Mountain-climate Interactions in the Himalayan-Tibet and Andean Orogens

by

Hong Shen

A dissertation submitted in partial fulfillment
of the requirements for the degree of
Doctor of Philosophy
(Earth and Environmental Sciences)
in the University of Michigan
2020

Doctoral Committee:

Professor Christopher J. Poulsen, Chair
Associate Professor Christiane Jablonowski
Professor Nathan Niemi
Associate Professor Benjamin Passey
Associate Professor Brian Yanites, Indiana University

Hong Shen

hdshen@umich.edu

ORCID iD: 0000-0003-4287-7989

Dedication

This dissertation is dedicated to my family and all of friends who supported me.

Acknowledgements

First and foremost, I would like to thank my advisor Chris Poulsen for his exceptional and insightful mentoring, patient guidance and continuous support and encouragement through the PhD period. I would also like to thank my committee – Brian, Nathan, Christiane and Ben – for their helpful suggestions and discussions. Special thanks to Brian for his help and guidance in doing the collaborative project on climate-erosion-mountain coupling. I'd also to thank my co-authors, Brian and Brigid, for the numerous helpful discussions and suggestions for the manuscripts.

I am very grateful to my current lab members, including Phoebe Aron, Alex Thompson, Sophie Macarewich, Paul Acosta and Jean-Baptiste Ladant, and former members, including Jiang Zhu, Chris Skinner, Andrew Guchte, Clay Tabor, Ran Feng, Richard Fiorella and Chana Tilevis. I will never forget the lab members reading my manuscripts and listening to my presentations many times and provided suggestions, especially helpful for me improve my writing and communication skills.

I would also like to thank my friend, Chuliang Xiao and Dr. David Gochis. Without their help, I would have spent more time struggling with running the WRF-Hydro model. Special thanks to my instructors from the English Language Institute, including Judy Dyer, Christine Feak and John Swales for their careful guidance with editing and writing.

I am very thankful to the friends, Yi Wang, Xiaojing Du, and many others, who provide continuous support, relaxation and encouragement throughout the PhD career. Last but not the least, I would like to thank my parents and other relatives for supporting me through all of my life!

Table of Contents

List of Tables

List of Figures

List of Appendices

Abstract

Mountain building processes have profound impact on both local and large-scale hydrology and climate change, and climate change interacts with mountain growth to form feedbacks. Numerous effects have been given to study the mountain-climate interactions, primarily by linking climate with erosion and topography during the growth history of mountains. Establishing such linkages require understanding on climate responses to mountain growth, how to interpret the climate signals preserved in proxy records, and the control of climate on landscape evolution. In this dissertation, we conduct numerical simulations in the Himalayan-Tibet and Andean orogens to investigate climate and isotopic response to mountain growth and the linked behavior among climate, erosion and topography.

Chapter 2 studies the climatic and isotopic responses to the uplift of the Himalayan-Tibet orogen and evaluate the application of the Rayleigh distillation process in reconstructing past elevation using an isotope-enabled general circulation model. The results show that the Rayleigh distillation is only the dominant process in monsoonal regions in the Himalayas when topography is high. At low elevations, local surface recycling becomes the primary process. On the Tibetan Plateau, stable water isotopes are shown to be primarily controlled by sub-cloud evaporation. This chapter show that the processes controlling isotopes varies by location and mountain elevation and using stable water isotopes as an indicator might be inappropriate.

Chapter 3 focuses on the climate response the widening of the central Andes, its impact on hydrology and proxy records, and the comparison with uniform uplift. The results show similar response of orographic precipitation on the eastern flank of central Andes due to the widening and due to the uplift, and substantial drying on the western flank due to the widening but little change due to the uplift. This chapter opens the ground of interpreting the hydrology changes preserved in proxy records as signals showing a west-east expansion of the Andes.

Chapter 4 is a technical study presenting a coupling framework for simulating climate-erosion-topography interaction, and simulations in various climate regimes to explore the strength of this interaction at different locations. The results from the simulations show a general

relationship of higher annual precipitation rates corresponding to higher discharge, more erosion, smaller slopes and lower elevation. This control is stronger in regions with heavier precipitation and when topography grows higher. This study highlights the mountain-climate interactions as a first-order control on mountain building process.

Collectively, these chapters improve our understanding on climate response to mountain growth, the interpretation of climate and hydrology signals in proxy records, and the control of climate change on shaping landscape through erosion.

Chapter 1 Introduction

1.1 Overview

Cenozoic orogenesis created the world's most extensive orogen systems today. Accompanying the evolution of these systems are monsoons and large-scale rainfall systems (e.g. Boos and Kuang, 2010; Ehlers and Poulsen, 2009), which relate directly to drought/flood distribution (e.g. Zhang et al., 2007), agriculture (Briner et al., 2013) and impact billions of human lives. Such large-scale rainfall systems also shape landscape by modulating erosion and sediment/nutrient transport (e.g. Hoorn et al., 2010), which triggers changes in surface elevation and climate responses. The sediment/nutrient transport further influences natural habitats, indirectly enhancing diversity and expanding distribution of species (e.g. Deng et al., 2020; McClain and Naiman, 2008). Given these broad impacts of the mountain-climate interactions during mountain-building process, understanding the strength, mechanisms and implications of these interactions is necessary.

Linking climate with erosion and topography during the growth history of mountain ranges provides insight into mountain-climate interactions. To establish this link, past studies have reconstructed past topography using proxy methods (e.g. Pingel et al., 2016; Rowley and Currie, 2006); have estimated past erosion rates (e.g. Barke and Lamb, 2006; Schildgen et al., 2009) and paleoclimate (e.g. Eiler, 2011) from proxy records; and have used climate and landscape evolution models to simulate climate responses to mountain growth (e.g. Lenters and Cook, 1995; Manabe and Terpstra, 1974; Roe et al., 2016) and erosional responses to climate change (e.g. Anders et al., 2008).

Understanding climate responses to mountain growth is crucial in interpreting proxy records, reconstructing past topography, and linking climate with erosion and topography. Most proxy records rely heavily on modern relationships between climate and mountain elevation to reconstruct past elevation (e.g. Pingel et al., 2016; Rowley and Currie, 2006). Due to the evolution of climate with mountain growth, this assumption of using the modern relationship might not have been valid in the past when the extensive mountain ranges both uplifted vertically

by several kilometers (e.g. Hoke et al., 2014; Rohrmann et al., 2016) and expanded horizontally by thousands of kilometers (e.g. Quade et al., 2015).

Field studies have reached opposing conclusions on the control of climate on erosion and topography (e.g. Whipple, 2014). Several studies have found precipitation modulating erosion rates (e.g. Ferrier et al., 2013). In contrast, other studies have detected no link between precipitation and erosion rates (Blythe et al., 2007; Burbank et al., 2003). One major limitation of these field studies is that they have relied on modern mean annual precipitation to relate precipitation to erosion. However, landscape evolution is driven by discrete events and the characteristics of these events evolve through time and with changes in topography (Tucker and Bras, 2000). Thus, new techniques incorporating the spatial and temporal variabilities of orographic precipitation and its response to topography is needed to properly investigate erosional responses to climate change.

Numerical modeling provides a powerful alternative way to study mountain-climate interactions. Climate models have the advantage of exploring climate sensitivities to various scenarios of topography (vertical uplift and horizontal expansion) (e.g. Kutzbach et al., 1989; Lenters and Cook, 1997; Roe et al., 2016), diagnosing climate and isotope related variables with high temporal and spatial resolution (e.g. Poulsen et al., 2010), and quantifying the relative contribution of the processes which impact proxy records and the responses of these processes to climate change (e.g. Feng et al., 2013). Landscape evolution models are capable of representing spatial and temporal variabilities of orographic precipitation (e.g. Tucker and Bras, 2000), and thus, provide more insights into erosional response to climate than field studies.

For this research, we conducted numerical simulations of the Himalayan-Tibet and Andes orogens to investigate climate and isotopic response to mountain growth and the linked behavior among climate, erosion and topography. These mountainous ranges were chosen because of their documented significant influence on local climate (Insel et al., 2010; Zhang et al., 2015), and their profound thermal and dynamic impact on large-scale atmospheric circulation and global climate (e.g. Feng and Poulsen, 2014; Kutzbach et al., 1993; Li et al., 2008).

1.2 Background

1.2.1 The Himalayan-Tibet orogen and the Andes: growth history, modern climate and climate response to topography

As the most extensive mountainous system, the Himalayan-Tibet orogen is believed to be an Andean type mountain range with a high Himalayas and low Tibetan Plateau before the collision of India and Eurasia around 60 Ma to 50 Ma (Wang et al., 2012). The growth of the Tibetan Plateau is thought to have been a south-to-north stepwise process (Tapponnier et al., 2001) with potential vertically-averaged uplift (Molnar et al., 1993). The timing for this stepwise growth is highly uncertain, varying by locations and studies depending on the type of proxy records (Clark et al., 2005; Molnar et al., 2010; Wang et al., 2008). Additionally, several studies have shown that the eastern Tibetan Plateau formed through the west-east expansion of the western-to-central plateau and that this expansion may have begun around 15-10 Ma (Mulch and Chamberlain, 2007).

The Himalaya-Tibet orogen spans various climate regimes and therefore should be investigated separately. In the modern era, the Himalayas is covered by three climate regimes spanning the mountain range (Yao et al., 2013): the western Himalayas is dominated by westerly winds and peak precipitation in boreal winter and spring; the central Himalayas is characterized by the Indian summer monsoon and southerly prevailing winds and the eastern Himalayas by the East Asian summer monsoon and southeasterly prevailing winds. The Tibetan Plateau to the north of the Himalayas, is known for nearly uniform elevation and drying out from low to high latitudes (Tong et al., 2014).

The climate response to surface uplift in these climate regimes is crucial in understanding its impact on proxy records and paleoaltimetry. Asian monsoon systems have received much attention in the past decades (e.g. Boos, 2015; Wu et al., 2012). Both field studies and modelling studies show a strengthening of the Indian summer monsoon system since at least the Miocene time (Liu et al., 2017; Molnar et al., 2010), and the uplift of the Himalaya-Tibet orogen is thought to be a first-order impact (Roe et al., 2016). In contrast, the response of the East Asian Summer Monsoon to surface uplift has been more contested and uncertain. Numerical modeling studies show an intensification of the East Asian Summer Monsoon due to the uplift of the Himalaya-Tibet orogen (Liu et al., 2017). However, there have also been studies arguing that

other mechanisms may include the retreat of the Paratethys (Guo et al., 2008) and global cooling since the Eocene (Licht et al., 2014). In contrast to the monsoonal regions, the climate response on the western Himalayan flank and on the Tibetan Plateau has received scant attention in past studies, and thus, the response of the isotopic gradient to surface uplift remains unknown.

The Andes, extending over 7000 m from north to south, is the second largest tectonically active orogen system and the most important mountain range in the Southern Hemisphere. Past studies have debated the timing of the uplift in the central Andes, arguing between rapid rise of ~2.5 km in Mid-Miocene (e.g. Pingel et al., 2016; Rohrmann et al., 2016), and gradual rise of the this height since the late Eocene (Ehlers and Poulsen, 2009; Poulsen et al., 2010). Proxy records suggest that this timing may have varied from west to east, with a potential first rise of the western flank since the Eocene (Bissig and Riquelme, 2010), and later rise of the plateau and the eastern flank in Miocene (e.g. Garzione et al., 2014), though there has been debates on an earlier uplift of the eastern flank prior to the plateau (Saylor and Horton, 2014).

The Andes spans the tropics to the midlatitudes and is covered by multiple climate regimes, providing rich atmospheric backgrounds for testing climate-erosion-topography coupling. Under modern conditions, the tropical Andes has been characterized by heavy precipitation on both sides of the mountain all year round. The sub-equatorial northern Andes (north of 15 °S) is characterized by seasonal heavy precipitation on the eastern windward flank (>50% in austral summer). The central Andes (15 °S–30 °S) is dominated by subtropical dry conditions with deserts on the leeward western flank. However, the windward eastern flank is not substantially dried out due to the South America Low-level Jet (LLJ), which is located to the east of the Andes in the sub-equatorial region and subtropics and is an important source transporting moisture from the tropics to subtropics in modern time. The southern Andes (south of 30 °S) is known for westerly winds, with heavy precipitation on the windward western flank and rain shadow on the leeward east flank.

With the growth of the Andes, field studies show an increase in orographic precipitation on the windward flanks, including the eastern flanks in the northern (e.g. Polissar et al., 2006) and central Andes (e.g. Rohrmann et al., 2016), and the western flank in the southern Andes (e.g. Blisniuk et al., 2005). Of these windward flanks, the precipitation in the central Andes showed a rapid increase during the Miocene (Rohrmann et al., 2016). Field studies also captured an aridity to hyperaridity transition on the western flank of the central Andes during the Miocene (Rech et

al., 2019). Climate simulations with scenarios of uniformly lowered Andes show a similar increase in orographic precipitation on the windward flanks (Poulsen et al., 2010). These models simulate a rapid increase in precipitation in the central Andes with uniform surface uplift from ~50% to ~75% of modern height. This rapid increase is attributed to the large-scale atmospheric response to uplift, in which the LLJ initiates with the uplift and transports more moisture to the south (Insel et al., 2010). On the western flank of the central Andes, past climate models with the uniform lowered scenarios have not detected a drying phase, as shown by the field studies, and there have been no numerical modeling studies studying the climate response to a widening of the central Andes.

1.2.2 Stable water isotopes: fundamentals and responses to mountain growth

Stable water isotopes have been widely used in the mountainous regions to reconstruct past elevation. During phase change, the heavier isotope is preferentially retained within the more condensed phase, and this process is called fractionation. Fractionation is classified as equilibrium and kinetic, with the former reversible and latter irreversible unidirectional. Phase changes can take place either with pure equilibrium fractionation or mixed with an additional kinetic fractionation. During kinetic fractionation, the less condensed phase is more depleted than equilibrium fractionation, making the more condensed phase more enriched. Kinetic fractionation becomes stronger when the relative humidity of ambient air is lower (Stewart, 1975), resulting in more enriched rainfall in dry regions and more depleted rainfall in humid regions. Due to reduced kinetic fractionation under high relative humidity in regions with heavy rainfall (e.g. tropics and monsoonal regions), isotopic composition in precipitation is found to decrease with increasing precipitation amount in these regions (e.g. Lee and Swann, 2010; Risi et al., 2008), and this relationship is called the amount effect. In addition to fractionation, other processes related to atmospheric circulation (e.g. moisture source through advection, surface water recycling) can also alter isotopic compositions (e.g. Risi et al., 2008).

Paleoaltimetry using stable water isotopes has relied heavily on the modern relationship between isotopic composition and mountain elevation. This relationship well agrees with the Rayleigh distillation process which describes preferential rainout of heave isotopes through pure equilibrium fractionation and continuing depletion of an air parcel when the air parcel is forced to uplift a mountain slope (Rowley et al., 2001). This modern relationship between the isotope

compositions with elevation has been widely used to reconstruct past elevation (e.g. Rowley and Garzione, 2007). However, it is unknown exactly how the partitioning of other processes responds to mountain growth. Numerical modeling studies using isotope-enabled climate models have reported that the amount effect in the North America Cordillera (Feng et al., 2013), moisture availability (Ehlers and Poulsen, 2009; Feng et al., 2013) and large-scale atmospheric circulation (Ehlers and Poulsen, 2009; Poulsen et al., 2010) in the Andes and the North America Cordillera are factors that can substantially alter isotopic compositions causing them to deviate from the relationship purely under the Rayleigh distillation process.

On this Himalayan flank, the modern relationship between stable water isotope and elevation accord well with the Rayleigh distillation process in all three climate regimes. To the north of the Himalayas, the Tibetan Plateau features nearly uniform elevation and drying out from low to high latitudes, and the compositions of stable oxygen isotope increase linearly with latitude due to the amount effect (e.g. Bershaw et al., 2012). This gradient is shown to have existed since the early Eocene (Caves Rugenstein and Chamberlain, 2018), and it has been suggested that it be used as a correction applied to isotopic compositions on the Tibetan plateau for reconstructing past elevation (Quade et al., 2011). The response of this gradient on the Tibetan Plateau and lapse rate of isotopic compositions in the Himalayas to the growth of the Himalaya-Tibet orogen has never been studied.

In the Andes, under modern conditions, it is shown that compositions of stable water isotopes display a strong relationship with elevation, and this relationship varies by location (Fiorella et al., 2015). Compositions of stable water isotopes is shown to be controlled by precipitation amount associated with sea-surface temperature and conditions in the Amazon Basin in northern Andes, wind trajectory and the position of the Bolivian High in the northern central Andes, and the strength and position in the southern central Andes (Insel et al., 2013). With the growth of the Andes, field studies have shown a decrease in compositions of stable water isotope on the windward flanks, and this decrease has been interpreted by an increase in orographic precipitation and surface elevation (e.g. Garzione et al., 2008; Garzione et al., 2017). Many studies have reported a rapid decrease of compositions of stable water isotopes between 15–6 Ma on the eastern flank of the central Andes (e.g. Pingel et al., 2016; Rohrmann et al., 2016), and have interpreted the decrease as representing a rapid rise in surface elevation. However, past the numerical modeling studies showed the initiation of LLJ as the cause for the

threshold decrease in precipitation and isotopic compositions (Ehlers and Poulsen, 2009; Poulsen et al., 2010). On the Andean plateau and leeward flank, field studies have shown an increase in compositions of stable water isotopes in Miocene (e.g. Saylor and Horton, 2014), that can be explained by an aridity to hyperaridity transition (Rech et al., 2019; Rech et al., 2006). Numerical modeling studies with uniformly uplifted topography from ~50% to 100% of modern elevation have captured the decrease in isotopic compositions on the windward flanks, but not the increase on the plateau and western flank of the central Andes (Poulsen et al., 2010). To date there have been no numerical modeling studies of the effect of the horizontal expansion (widening) of the Andes on climate change and potential climate-related isotopic changes.

1.2.3 Modeling climate-erosion-topography interactions

Landscape evolution models have the advantage of incorporating spatial and temporal variabilities of precipitation over field studies which can only link proxy records to modern precipitation. However, these variabilities of precipitation have been greatly simplified in past studies (Roe et al., 2002; Willett, 1999). Furthermore, these past models do not include the responses of precipitation to large-scale atmospheric changes to landscape, such as the initiation of the LLJ and the strengthening in monsoon systems. Thus, past landscape evolution models are incapable of properly modelling the landscape response to precipitation and the interactions between climate and mountain elevation on geological time scale of mountain building.

Building such a modelling framework and appropriately incorporating the interactions and feedback is challenging, since landscape and climate processes differ on both spatial and temporal scales. Landscape evolves on the time scale of millions of years, and it typically takes a few hundred thousand to a few million years for fluvial bedrock channels to respond to climate perturbations (Snyder et al., 2003). To make it computationally possible to integrate millions of years, the time step of the landscape model is typically in hundreds or thousands of years. Spatially, the scale of the fluvial channels is in the order of tens to hundreds of meters, thus, fine spatial resolution is required to resolve the channels. On the contrary, atmospheric models capture synoptic-scale weather systems' large-scale atmospheric changes (e.g. LLJ and monsoon), and thus, employ large domains. To ensure computational feasibility running the large domains, the spatial resolution of the atmospheric model is usually on the scale of tens to hundreds of kilometers. Temporally, to capture medium-scale systems (e.g. gravity wave) with

lifetimes of minutes to hours and keep the computing stable, the time step of the atmospheric models must be small i.e. in the range of seconds to minutes.

1.3 Dissertation outline

This dissertation is organized as follows: The data chapters (Chapters 2 through 4) consist of three studies using climate models and landscape evolution models to investigate mountain-climate interactions, followed by a conclusion chapter (Chapter 5).

In Chapter 2 (*published in Climate of the Past*), we use an isotope enabled general circulation model, ECHAM5-wiso, to investigate how the climate response to surface uplift impacts the key processes that control compositions of stable oxygen isotopes in the Himalaya-Tibet orogen. Our results show that the modern Rayleigh distillation process is only dominant in the monsoonal regions and when the mountains are high, but that the isotopic gradient also decreases when mountains are lowered. This study indicates that stable isotope paleoaltimetry should be used with great caution in this mountain range.

In Chapter 3 (*to be submitted*), we use a regional climate model, WRF, to study the climate response to the growth of the central Andes, and the potential impact of climate on reconstructed signals in proxy records. We include both the vertical uplift and the horizontal expansion (widening) of the central Andes in this study. Our results show that the widening of the central Andes shares a similar climate response on the windward flanks to the uniform uplift of the Andes, but the widening scenario captures a drying phase on the plateau and leeward flank in the central Andes. These results provide an alternative interpretation of proxy records.

In Chapter 4 (*in review with Computers and Geosciences*), we build a modeling framework coupling a regional climate model, WRF, and a hydrological model, WRF-HYDRO, to a landscape evolution model, Landlab. The goal is to simulate the climate-erosion-elevation interactions and gain insight as to whether the coupling strength varies in different climate regimes, and whether the coupling is sufficiently strong to impact the overall mountain building process. To overcome the challenges from the huge difference in temporal and spatial scales between the climate and landscape evolution models, in our study we used nested domains and asynchronous coupling techniques. We then simulated the coupling behavior by building a mountain range along the western coast in South America at the location of today's Andes. Our

results show that the strength of climate-erosion-topography interactions varies by climate regimes, and this interaction is a first-order control on the mountain-building process.

1.4 References

Anders, A. M., Roe, G. H., Montgomery, D. R., and Hallet, B., 2008, Influence of precipitation phase on the form of mountain ranges: Geology, v. 36, no. 6, p. 479-482.

Barke, R., and Lamb, S., 2006, Late Cenozoic uplift of the Eastern Cordillera, Bolivian Andes: Earth and Planetary Science Letters, v. 249, no. 3, p. 350-367.

Bershaw, J., Penny, S. M., and Garzione, C. N., 2012, Stable isotopes of modern water across the Himalaya and eastern Tibetan Plateau: Implications for estimates of paleoelevation and paleoclimate: Journal of Geophysical Research-Atmospheres, v. 117, p. D02110.

Bissig, T., and Riquelme, R., 2010, Andean uplift and climate evolution in the southern Atacama Desert deduced from geomorphology and supergene alunite-group minerals: Earth and Planetary Science Letters, v. 299, no. 3, p. 447-457.

Blisniuk, P. M., Stern, L. A., Chamberlain, C. P., Idleman, B., and Zeitler, P. K., 2005, Climatic and ecologic changes during Miocene surface uplift in the Southern Patagonian Andes: Earth and Planetary Science Letters, v. 230, no. 1, p. 125-142.

Blythe, A. E., Burbank, D. W., Carter, A., Schmidt, K., and Putkonen, J., 2007, Plio-Quaternary exhumation history of the central Nepalese Himalaya: 1. Apatite and zircon fission track and apatite [U-Th]/He analyses: Tectonics, v. 26, no. 3, p. TC3002.

Boos, W. R., 2015, A review of recent progress on Tibet's role in the South Asian monsoon: CLIVAR Exchanges Special Issue on Monsoons, v. 66, p. 23-27.

Boos, W. R., and Kuang, Z., 2010, Dominant control of the South Asian monsoon by orographic insulation versus plateau heating: Nature, v. 463, no. 7278, p. 218-222.

Briner, S., Elkin, C., and Huber, R., 2013, Evaluating the relative impact of climate and economic changes on forest and agricultural ecosystem services in mountain regions: Journal of Environmental Management, v. 129, p. 414-422.

Burbank, D. W., Blythe, A. E., Putkonen, J., Pratt-Sitaula, B., Gabet, E., Oskin, M., Barros, A., and Ojha, T. P., 2003, Decoupling of erosion and precipitation in the Himalayas: Nature, v. 426, no. 6967, p. 652-655.

Caves Rugenstein, J. K., and Chamberlain, C. P., 2018, The evolution of hydroclimate in Asia over the Cenozoic: A stable-isotope perspective: Earth-Science Reviews, v. 185, p. 1129-1156.

Clark, M. K., House, M. A., Royden, L. H., Whipple, K. X., Burchfiel, B. C., Zhang, X., and Tang, W., 2005, Late Cenozoic uplift of southeastern Tibet: Geology, v. 33, no. 6, p. 525-528.

Deng, T., Wu, F., Zhou, Z., and Su, T., 2020, Tibetan Plateau: An evolutionary junction for the history of modern biodiversity: Science China Earth Sciences, v. 63, no. 2, p. 172-187.

Ehlers, T. A., and Poulsen, C. J., 2009, Influence of Andean uplift on climate and paleoaltimetry estimates: Earth and Planetary Science Letters, v. 281, no. 3-4, p. 238-248.

Eiler, J. M., 2011, Paleoclimate reconstruction using carbonate clumped isotope thermometry: Quaternary Science Reviews, v. 30, no. 25, p. 3575-3588.

Feng, R., and Poulsen, C. J., 2014, Andean elevation control on tropical Pacific climate and ENSO: Paleoceanography, v. 29, no. 8, p. 795-809.

Feng, R., Poulsen, C. J., Werner, M., Chamberlain, C. P., Mix, H. T., and Mulch, A., 2013, Early Cenozoic evolution of topography, climate, and stable isotopes in precipitation in the North American Cordillera: American Journal of Science, v. 313, no. 7, p. 613-648.

Ferrier, K. L., Huppert, K. L., and Perron, J. T., 2013, Climatic control of bedrock river incision: Nature, v. 496, no. 7444, p. 206-209.

Garzione, C. N., Auerbach, D. J., Jin-Sook Smith, J., Rosario, J. J., Passey, B. H., Jordan, T. E., and Eiler, J. M., 2014, Clumped isotope evidence for diachronous surface cooling of the Altiplano and pulsed surface uplift of the Central Andes: Earth and Planetary Science Letters, v. 393, p. 173-181.

Garzione, C. N., Hoke, G. D., Libarkin, J. C., Withers, S., MacFadden, B., Eiler, J., Ghosh, P., and Mulch, A., 2008, Rise of the Andes: Science, v. 320, no. 5881, p. 1304-1307.

Garzione, C. N., McQuarrie, N., Perez, N. D., Ehlers, T. A., Beck, S. L., Kar, N., Eichelberger, N., Chapman, A. D., Ward, K. M., Ducea, M. N., Lease, R. O., Poulsen, C. J., Wagner, L. S., Saylor, J. E., Zandt, G., and Horton, B. K., 2017, Tectonic Evolution of the Central Andean Plateau and Implications for the Growth of Plateaus: Annual Review of Earth and Planetary Sciences, v. 45, no. 1, p. 529-559.

Guo, Z. T., Sun, B., Zhang, Z. S., Peng, S. Z., Xiao, G. Q., Ge, J. Y., Hao, Q. Z., Qiao, Y. S., Liang, M. Y., Liu, J. F., Yin, Q. Z., and Wei, J. J., 2008, A major reorganization of Asian climate by the early Miocene: Clim. Past, v. 4, no. 3, p. 153-174.

Hoke, G. D., Liu-Zeng, J., Hren, M. T., Wissink, G. K., and Garzione, C. N., 2014, Stable isotopes reveal high southeast Tibetan Plateau margin since the Paleogene: Earth and Planetary Science Letters, v. 394, no. Supplement C, p. 270-278.

Hoorn, C., Wesselingh, F. P., ter Steege, H., Bermudez, M. A., Mora, A., Sevink, J., Sanmartín, I., Sanchez-Meseguer, A., Anderson, C. L., Figueiredo, J. P., Jaramillo, C., Riff, D., Negri, F. R., Hooghiemstra, H., Lundberg, J., Stadler, T., Särkinen, T., and Antonelli, A., 2010, Amazonia Through Time: Andean Uplift, Climate Change, Landscape Evolution, and Biodiversity: Science, v. 330, no. 6006, p. 927-931.

Insel, N., Ehlers, T. A., Schaller, M., Barnes, J. B., Tawackoli, S., and Poulsen, C. J., 2010, Spatial and temporal variability in denudation across the Bolivian Andes from multiple geochronometers: Geomorphology, v. 122, no. 1-2, p. 65-77.

Kutzbach, J. E., Guetter, P. J., Ruddiman, W. F., and Prell, W. L., 1989, Sensitivity of climate to late Cenozoic uplift in southern Asia and the American west: Numerical experiments: Journal of Geophysical Research: Atmospheres, v. 94, no. D15, p. 18393-18407.

Kutzbach, J. E., Prell, W. L., and Ruddiman, W. F., 1993, Sensitivity of Eurasian Climate to Surface Uplift of the Tibetan Plateau: The Journal of Geology, v. 101, no. 2, p. 177-190.

Lee, J.-E., and Swann, A. L., 2010, Evaluation of the "amount effect" at speleothem sites in the Asian monsoon region: IOP Conference Series: Earth and Environmental Science, v. 9, p. 012023.

Lenters, J. D., and Cook, K. H., 1995, Simulation and Diagnosis of the Regional Summertime Precipitation Climatology of South America: Journal of Climate, v. 8, no. 12, p. 2988-3005.

-, 1997, On the Origin of the Bolivian High and Related Circulation Features of the South American Climate: Journal of the Atmospheric Sciences, v. 54, no. 5, p. 656-678.

Li, J., Yu, R., and Zhou, T., 2008, Teleconnection between NAO and Climate Downstream of the Tibetan Plateau: Journal of Climate, v. 21, no. 18, p. 4680-4690.

Licht, A., van Cappelle, M., Abels, H. A., Ladant, J. B., Trabucho-Alexandre, J., France-Lanord, C., Donnadieu, Y., Vandenberghe, J., Rigaudier, T., Lecuyer, C., Terry Jr, D., Adriaens, R., Boura, A., Guo, Z., Soe, A. N., Quade, J., Dupont-Nivet, G., and Jaeger, J. J., 2014, Asian monsoons in a late Eocene greenhouse world: Nature, v. 513, no. 7519, p. 501-506.

Liu, X., Dong, B., Yin, Z.-Y., Smith, R. S., and Guo, Q., 2017, Continental drift and plateau uplift control origination and evolution of Asian and Australian monsoons: Scientific Reports, v. 7, p. 40344.

Manabe, S., and Terpstra, T. B., 1974, The Effects of Mountains on the General Circulation of the Atmosphere as Identified by Numerical Experiments: Journal of the Atmospheric Sciences, v. 31, no. 1, p. 3-42.

McClain, M. E., and Naiman, R. J., 2008, Andean Influences on the Biogeochemistry and Ecology of the Amazon River: BioScience, v. 58, no. 4, p. 325-338.

Molnar, P., England, P., and Martinod, J., 1993, Mantle dynamics, uplift of the Tibetan Plateau, and the Indian Monsoon: Reviews of Geophysics, v. 31, no. 4, p. 357-396.

Molnar, P., Boos, W. R., and Battisti, D. S., 2010, Orographic Controls on Climate and Paleoclimate of Asia: Thermal and Mechanical Roles for the Tibetan Plateau: Annual Review of Earth and Planetary Sciences, v. 38, no. 1, p. 77-102.

Mulch, A., and Chamberlain, C. P., 2007, Stable isotope paleoaltimetry in orogenic belts - The silicate record in surface and crustal geological archives: Paleoaltimetry: Geochemical and Thermodynamic Approaches, v. 66, p. 89-118.

Pingel, H., Mulch, A., Alonso, R. N., Cottle, J., Hynek, S. A., Poletti, J., Rohrmann, A., Schmitt, A. K., Stockli, D. F., and Strecker, M. R., 2016, Surface uplift and convective rainfall along the southern Central Andes (Angastaco Basin, NW Argentina): Earth and Planetary Science Letters, v. 440, p. 33-42.

Polissar, P. J., Abbott, M. B., Shemesh, A., Wolfe, A. P., and Bradley, R. S., 2006, Holocene hydrologic balance of tropical South America from oxygen isotopes of lake sediment opal, Venezuelan Andes: Earth and Planetary Science Letters, v. 242, no. 3, p. 375-389.

Poulsen, C. J., Ehlers, T. A., and Insel, N., 2010, Onset of convective rainfall during gradual late Miocene rise of the central Andes: Science, v. 328, no. 5977, p. 490-493.

Quade, J., Breecker, D. O., Daeron, M., and Eiler, J., 2011, The paleoaltimetry of Tibet: An isotopic perspective: American Journal of Science, v. 311, no. 2, p. 77-115.

Quade, J., Dettinger, M. P., Carrapa, B., DeCelles, P., Murray, K. E., Huntington, K. W., Cartwright, A., Canavan, R. R., Gehrels, G., and Clementz, M., 2015, The growth of the central Andes, 22°S–26°S, *in* DeCelles, P. G., Ducea, M. N., Carrapa, B., and Kapp, P. A., eds., Geodynamics of a Cordilleran Orogenic System: The Central Andes of Argentina and Northern Chile, Geological Society of America.

Rech, J. A., Currie, B. S., Jordan, T. E., Riquelme, R., Lehmann, S. B., Kirk-Lawlor, N. E., Li, S., and Gooley, J. T., 2019, Massive middle Miocene gypsic paleosols in the Atacama Desert and the formation of the Central Andean rain-shadow: Earth and Planetary Science Letters, v. 506, p. 184-194.

Rech, J. A., Currie, B. S., Michalski, G., and Cowan, A. M., 2006, Neogene climate change and uplift in the Atacama Desert, Chile: Geology, v. 34, no. 9, p. 761-764.

Risi, C., Bony, S., and Vimeux, F., 2008, Influence of convective processes on the isotopic composition (δ18O andδD) of precipitation and water vapor in the tropics: 2. Physical interpretation of the amount effect: Journal of Geophysical Research, v. 113, no. D19.

Roe, G. H., Ding, Q., Battisti, D. S., Molnar, P. H., Clark, M. K., and Garzione, C., 2016, A modeling study of the response of Asian summertime climate to the largest geologic forcings of the past 50 Ma: Journal of Geophysical Research: Atmospheres, p. 5453-5470.

Roe, G. H., Montgomery, D. R., and Hallet, B., 2002, Effects of orographic precipitation variations on the concavity of steady-state river profiles: Geology, v. 30, no. 2, p. 143-146.

Rohrmann, A., Sachse, D., Mulch, A., Pingel, H., Tofelde, S., Alonso, R. N., and Strecker, M. R., 2016, Miocene orographic uplift forces rapid hydrological change in the southern central Andes: Scientific Reports, v. 6, p. 35678.

Rowley, D. B., and Currie, B. S., 2006, Palaeo-altimetry of the late Eocene to Miocene Lunpola basin, central Tibet: Nature, v. 439, no. 7077, p. 677-681.

Rowley, D. B., and Garzione, C. N., 2007, Stable Isotope-Based Paleoaltimetry: Annual Review of Earth and Planetary Sciences, v. 35, no. 1, p. 463-508.

Rowley, D. B., Pierrehumbert, R. T., and Currie, B. S., 2001, A new approach to stable isotope-based paleoaltimetry: implications for paleoaltimetry and paleohypsometry of the High Himalaya since the Late Miocene: Earth and Planetary Science Letters, v. 188, no. 1-2, p. 253-268.

Saylor, J. E., and Horton, B. K., 2014, Nonuniform surface uplift of the Andean plateau revealed by deuterium isotopes in Miocene volcanic glass from southern Peru: Earth and Planetary Science Letters, v. 387, p. 120-131.

Schildgen, T. F., Hodges, K. V., Whipple, K. X., Pringle, M. S., van Soest, M., and Cornell, K., 2009, Late Cenozoic structural and tectonic development of the western margin of the central Andean Plateau in southwest Peru: Tectonics, v. 28, no. 4.

Snyder, N. P., Whipple, K. X., Tucker, G. E., and Merritts, D. J., 2003, Importance of a stochastic distribution of floods and erosion thresholds in the bedrock river incision problem: Journal of Geophysical Research: Solid Earth, v. 108, no. B2.

Stewart, M. K., 1975, Stable isotope fractionation due to evaporation and isotopic exchange of falling waterdrops: Applications to atmospheric processes and evaporation of lakes: Journal of Geophysical Research, v. 80, no. 9, p. 1133-1146.

Tapponnier, P., Zhiqin, X., Roger, F., Meyer, B., Arnaud, N., Wittlinger, G., and Jingsui, Y., 2001, Oblique Stepwise Rise and Growth of the Tibet Plateau: Science, v. 294, no. 5547, p. 1671-1677.

Tong, K., Su, F., Yang, D., Zhang, L., and Hao, Z., 2014, Tibetan Plateau precipitation as depicted by gauge observations, reanalyses and satellite retrievals: International Journal of Climatology, v. 34, no. 2, p. 265-285.

Tucker, G. E., and Bras, R. L., 2000, A stochastic approach to modeling the role of rainfall variability in drainage basin evolution: Water Resources Research, v. 36, no. 7, p. 1953-1964.

Wang, C., Zhao, X., Liu, Z., Lippert, P. C., Graham, S. A., Coe, R. S., Yi, H., Zhu, L., Liu, S., and Li, Y., 2008, Constraints on the early uplift history of the Tibetan Plateau: Proceedings of the National Academy of Sciences, v. 105, no. 13, p. 4987-4992.

Wang, X., Zhang, J., Santosh, M., Liu, J., Yan, S., and Guo, L., 2012, Andean-type orogeny in the Himalayas of south Tibet: Implications for early Paleozoic tectonics along the Indian margin of Gondwana: Lithos, v. 154, p. 248-262.

Whipple, K. X., 2014, Can erosion drive tectonics?: Science, v. 346, no. 6212, p. 918-919.

Willett, S. D., 1999, Orogeny and orography: The effects of erosion on the structure of mountain belts: Journal of Geophysical Research: Solid Earth, v. 104, no. B12, p. 28957-28981.

Wu, G., Liu, Y., He, B., Bao, Q., Duan, A., and Jin, F.-F., 2012, Thermal Controls on the Asian Summer Monsoon: Scientific Reports, v. 2, no. 1, p. 404.

Yao, T. D., Masson-Delmotte, V., Gao, J., Yu, W. S., Yang, X. X., Risi, C., Sturm, C., Werner, M., Zhao, H. B., He, Y., Ren, W., Tian, L. D., Shi, C. M., and Hou, S. G., 2013, A review

of climatic controls on δ18O in precipitation over the Tibetan Plateau: observations and simulations: Reviews of Geophysics, v. 51, no. 4, p. 525-548.

Zhang, Q., Chen, J., and Becker, S., 2007, Flood/drought change of last millennium in the Yangtze Delta and its possible connections with Tibetan climatic changes: Global and Planetary Change, v. 57, no. 3, p. 213-221.

Zhang, R., Jiang, D., Zhang, Z., and Yu, E., 2015, The impact of regional uplift of the Tibetan Plateau on the Asian monsoon climate: Palaeogeography, Palaeoclimatology, Palaeoecology, v. 417, p. 137-150.

Chapter 2
Precipitation $\delta^{18}O$ on the Himalaya-Tibet Orogeny and its Relationship to Surface Elevation

Abstract

The elevation history of the Himalaya-Tibet orogen is central to understanding the evolution and dynamics of both the Indian-Asia collision and the Asian monsoons. The surface elevation history of the region is largely deduced from stable isotope ($\delta^{18}O$, δD) paleoaltimetry. This method is based on the observed relationship between the isotopic composition of meteoric waters ($\delta^{18}O_p$, δD_p) and surface elevation, and the assumption that precipitation undergoes Rayleigh distillation under forced ascent. Here we evaluate how elevation-induced climate change influences the $\delta^{18}O_p$-elevation relationship and whether Rayleigh distillation is the dominant process affecting $\delta^{18}O_p$. We use an isotope-enabled climate model, ECHAM-wiso, to show that the Rayleigh distillation process is only dominant in the monsoonal regions of the Himalayas when the mountains are high. When the orogen is lowered, local surface recycling and convective processes become important as forced ascent is weakened due to weaker Asian monsoons. As a result, the $\delta^{18}O_p$ lapse rate in the Himalayas increases from around −3 ‰/km to above −0.1 ‰/km, having little relationship with elevation. On the Tibetan Plateau, the meridional gradient of $\delta^{18}O$ decreases from ~1 ‰/° to ~0.3 ‰/° with reduced elevation, primarily due to enhanced sub-cloud re-evaporation under lower relative humidity. Overall, we report that using $\delta^{18}O_p$ or δD_p to deduce surface elevation change in the Himalaya-Tibet region has severe limitations and demonstrate that the processes that control annual-mean precipitation-weighted $\delta^{18}O_p$ vary by region and with surface elevation. In sum, we determine that the application of $\delta^{18}O$-paleoaltimetry is only appropriate for 7 of the 50 sites from which $\delta^{18}O$ records have been used to infer past elevations.

2.1 Introduction

Surface elevation is a fundamental characteristic of the Earth surface, directly affecting atmospheric circulation patterns and surface temperatures, precipitation and surface hydrology, erosion and sediment transport, and the distribution and diversity of life (Aron and Poulsen, 2018). Created by India-Asia convergence and is believed to be an Andean type mountain range with a high Himalayas and low Tibetan Plateau before the collision (Wang et al., 2012), the Himalaya-Tibet Orogen was the defining event of the Asian continent in the Cenozoic and had global environmental implications. Surface uplift of the orogen has been implicated in the onset and strengthening of the southeast Asian monsoon system (Boos and Kuang, 2010; Zhang et al., 2015) and the position of atmospheric stationary waves (Kutzbach et al., 1989); the evolutionary diversification and biogeographic distribution of fauna and flora in central Asia (Zhao et al., 2016; Yang et al., 2009; Antonelli et al., 2018); and, the intensification of chemical weathering of exposed rocks and transport of nutrients to the ocean that contributed to global atmospheric CO_2 drawdown (Galy et al., 2007; Maffre et al., 2018). Surface elevation also lends a first-order constraint on the crustal and upper mantle dynamics that create topography (Ehlers and Poulsen, 2009). Surface elevation estimates for the Himalaya-Tibet orogen, and specifically evidence for high elevations of the orogen since the late Eocene, have been instrumental in supporting geodynamical models of Tibetan Plateau growth through early deformation and crustal thickening (Rowley and Currie, 2006; Rohrmann et al., 2012; Hoke et al., 2014).

The paramount importance of surface elevation to our understanding of Cenozoic environmental and tectonic evolution has led to a proliferation of studies that infer past Himalaya-Tibet surface elevations from ancient proxy materials (Cyr et al., 2005; Rowley and Currie, 2006; Li et al., 2015). Stable isotope paleoaltimetry, one of the few quantitative methods to reconstruct past surface elevations, relies on the water isotopic composition of ancient materials, including pedogenic and lacustrine carbonates, authigenic clay and hydrated volcanic glass, that were formed in contact with ancient surface waters. The method is predicated on the observed, modern decrease in water stable isotopic compositions ($\delta^{18}O$, δD) with elevation gain (the isotopic lapse rate) (Chamberlain and Poage, 2000) a relationship that is commonly attributed to rainout of heavy isotopologues during stably forced ascent of a saturated air over high elevation and is modeled as a Rayleigh distillation process (e.g. Rowley and Garzione, 2007). Stable isotope paleoaltimetry has been used to reconstruct past surface elevation of many

of the world's major mountain belts, including the North America Cordillera (e.g. Poage and Chamberlain, 2002; Fan et al., 2014), the Andes (e.g. Garzione et al., 2008), and the Himalayan-Tibetan orogen (e.g. Rowley and Currie, 2006), due to the robustness of the isotopic lapse rate in modern orogenic regions and the ubiquity of proxy materials.

The interpretation of stable isotopes in ancient materials to infer past surface elevation is complicated by factors related both to the mineralization of proxy materials and to the isotope-elevation relationship of meteoric waters from which the proxies form (Poage and Chamberlain, 2001). With regard to the latter factor, studies using global climate models have demonstrated that the isotopic lapse rate can be dependent on a mountain range's elevation due to processes that are not described by Rayleigh distillation (Ehlers and Poulsen, 2009; Poulsen et al., 2010; Feng et al., 2013; Botsyun et al., 2016). Indeed, Feng et al. (2013) showed that the simulated $\delta^{18}O$ of precipitation ($\delta^{18}O_p$) during uplift of the Eocene North America Cordillera was substantially influenced by changes in vapor mixing, surface recycling, moisture source change, and precipitation type. Similarly, Botsyun et al. (2016) investigated $\delta^{18}O_p$ across the Himalaya-Tibet region in response to surface uplift and showed that direct topographic effects only partially accounted for total $\delta^{18}O_p$ changes.

On the Himalayan slope, $\delta^{18}O$ in surface waters and precipitation has been widely observed to decrease with elevation at a rate of ~3 ‰/km (e.g. Rowley et al., 2001). The $\delta^{18}O$-elevation relationship has been attributed to orographic rainout and modeled as a Rayleigh distillation process (e.g. Rowley and Currie, 2006). On the Tibetan plateau, $\delta^{18}O$ in surface water and precipitation increases linearly with latitude by ~1 ‰/° over nearly uniform elevation (e.g. Bershaw et al., 2012). The source of $\delta^{18}O$ variations on the plateau and whether $\delta^{18}O$ can be used for paleoaltimetry on the high Tibetan Plateau has received little attention. Quade et al., (2011) proposed that paleoelevations could be inferred from proxy $\delta^{18}O$ after removing the meridional $\delta^{18}O$ gradient on the Tibetan Plateau. This south-to-north gradient in $\delta^{18}O$ has been reported to have existed since the early Eocene (Caves Rugenstein and Chamberlain, 2018). However, little is known about either the processes that contribute to the meridional $\delta^{18}O$ gradient or how the meridional $\delta^{18}O$ gradient varied when the plateau was lower.

The goal of this study is to identify and quantify the processes that control $\delta^{18}O_p$ variations across the Himalayas and the Tibetan Plateau and to evaluate the utility of $\delta^{18}O_p$ as a

paleoaltimeter in these regions. To do this, we use an isotope-enabled global climate model, ECHAM5-wiso, with prescribed elevation scenarios and compare the annual-mean precipitation-weighted $\delta^{18}O_p$ calculated by the climate model with that expected due to Rayleigh distillation alone. Botsyun et al. (2016) used the LMDZ-iso model to decompose the influence of adiabatic elevation changes on $\delta^{18}O_p$ from other influences due to non-adiabatic temperature changes, local changes in relative humidity and post-condensational processes. Building on Botsyun et al. (2016), we take a more process-oriented approach to quantify the isotopic fluxes attributed to specific mechanisms and demonstrate that the contributions from these processes vary spatially and in response to elevation change. Finally, we discuss the implications of our results for reconstructing paleoaltimetry of the Himalayas and Tibetan Plateau. Although our prescribed elevation scenarios are idealized and may not conform with past elevation at particular time slices, and thus, do not provide direct comparison to proxy records, our simulations provide insights on the sensitivities of climate and isotope processes to surface elevations.

2.2 Methods

2.2.1 Model and experimental design

In this study, we employ ECHAM5-wiso, a water isotope-enabled atmospheric global climate model (AGCM). The model has been widely used both for modern and past climate and isotope simulations. For instance, Feng et al. (2013) and Feng and Poulsen (2016) employed ECHAM5-wiso to explore climate and isotopic responses to Cenozoic surface uplift and climate change in western North America. ECHAM has also been shown to simulate many aspects of Asian climate (e.g. Battisti et al., 2014) and isotopic compositions ($\delta^{18}O_p$) simulated by ECHAM5-wiso generally agree well with observed modern stream and precipitation $\delta^{18}O$ across the Tibetan Plateau as shown by Li et al. (2016) (see their Fig. 2-11).

We use a model configuration with 19 vertical levels, and a spectral triangular truncation of 106 horizontal waves, approximately equivalent to a 100-km grid spacing. This horizontal resolution, though still relatively coarse, is about twice that of recent simulations used to validate the simulation of water isotopes over the Tibetan plateau (Li et al., 2016) and recent paleoclimate simulations of the Tibetan Plateau (e.g. Roe et al., 2016). The AGCM is coupled to a slab-ocean model, the MPI-OM, with prescribed ocean heat flux from the Atmospheric Modeling Project Intercomparison 2 (AMIP2; Gleckler, 2005) averaged over years 1956-2000. A modern annual

mean seawater $\delta^{18}O$ dataset spanning from 1956 to 2006 (LeGrande and Schmidt, 2006) is provided as a lower boundary condition for the model.

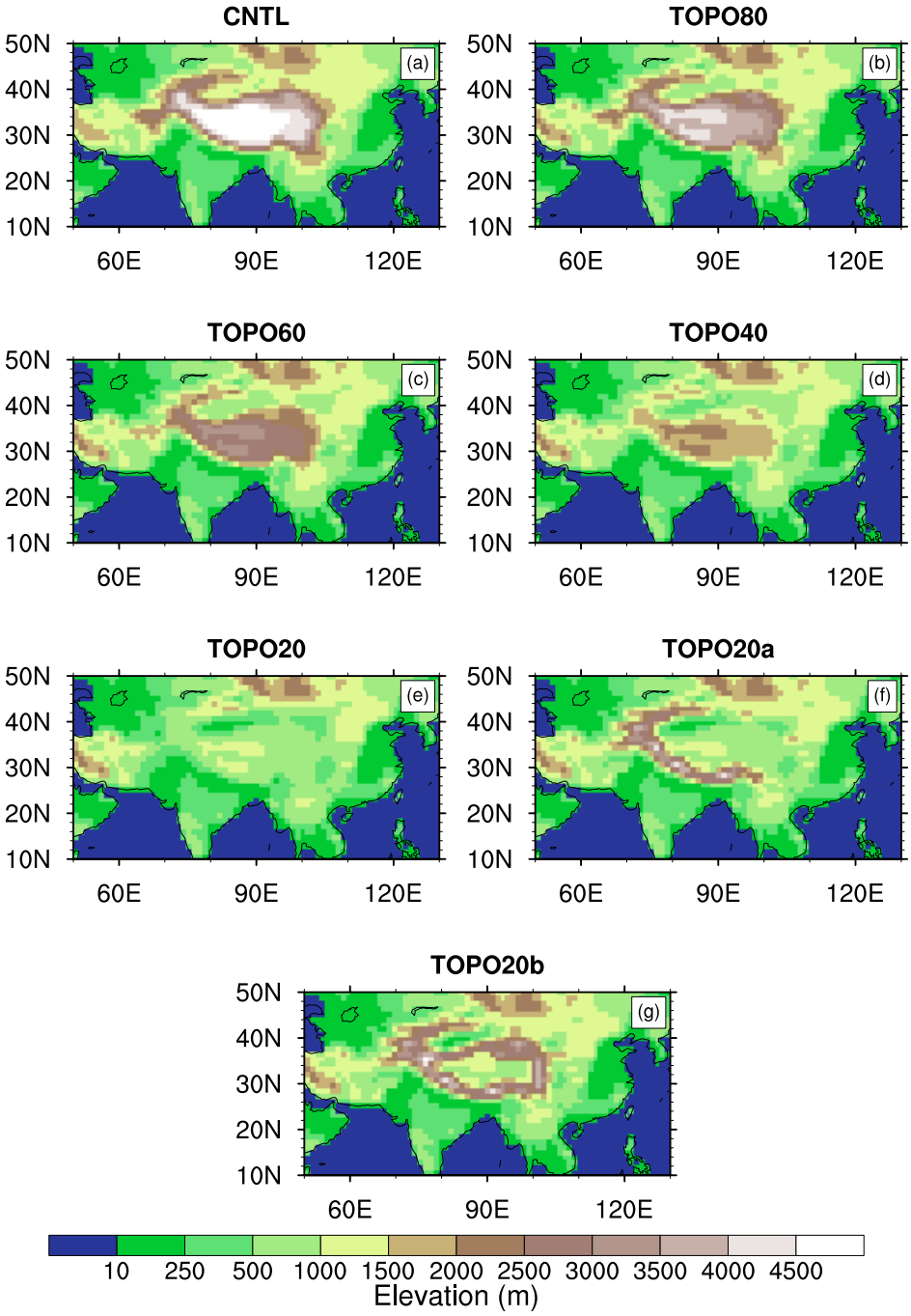

Figure 2-1 Surface elevations (m) prescribed in ECHAM5

(a) CNTL, (b) TOPO80, (c) TOPO60, (d) TOPO40, (e) TOPO20, (f) TOPO20a, and (g) TOPO20b. Note that the CNTL simulations includes modern elevations. The names of the other cases (e.g. TOPO60) indicate surface elevations of the Himalaya-Tibetan region relative to the modern (e.g. 60%). Cases TOPO2a and TOPO20b are modifications of the TOPO20 case (see Methods).

In ECHAM5-wiso, water isotopologues are included as independent tracers in the atmosphere. When water evaporates from the sea, both equilibrium and non-equilibrium distillation processes occur as a function of sea surface temperature, wind speed, relative humidity, isotope composition in seawater and vapor above the ocean surface (Hoffmann et al., 1998). Convective rains are assumed to have larger raindrops that reach only partial (50%) isotopic equilibration with surrounding vapor, while large-scale precipitation has smaller raindrops and attains almost complete (90%) equilibration with the environment (Hoffmann et al., 1998). For kinetic fractionation of raindrops during partial evaporation in ECHAM5-wiso, the fractionation factor is formulated to depend on the sub-cloud relative humidity of the entire grid box (Hoffmann et al., 1998). Only large lakes, the size of at least one-half grid cell, are resolved in the model, and fractionation from the land surface is not included since its impact on precipitation $\delta^{18}O_p$ is negligible (Haese et al., 2013).

We conducted two sets of sensitivity experiments (Fig. 2-1) in addition to a control simulation with modern conditions (CNTL). In the first set of sensitivity experiments, topography is uniformly lowered to 80% (TOPO80), 60% (TOPO60), 40% (TOPO40) and 20% (TOPO20) of its modern elevation over a domain that includes the Himalaya and Tibetan plateau. In the second set of sensitivity experiments, we conducted two experiments with non-uniform elevation modifications over this domain. The first experiment includes a high Himalayan front with a Tibetan Plateau reduced to 20% of its modern elevation (TOPO20a). This experiment is inspired by the widely accepted notion that southeast Asia had an Andean type mountain belt before the collision of the Eurasia and the Indian plate (Royden et al., 2008). TOPO20a also serves as a test of the Himalaya on the regional climate. In the second experiment, the outer edge of the Tibetan Plateau remains, but the inside is lowered to 20% of its modern height (TOPO20b). The second experiment is a sensitivity test to investigate the role of plateau heating on regional climate and isotopic compositions. In both sets of experiments, we tapered the topography along the borders of the domains to avoid any abrupt topography boundaries. Except for topography, all other boundary conditions are kept the same among all experiments. Each experiment was run for 20 years, with the last 15 years used for analysis. Summertime (June-July-August) climate variables and annual-mean precipitation-weighted $\delta^{18}O$ are analysed and presented, reflecting that total precipitation over most of the region is

dominated by summer precipitation and that carbonates preferentially form in summer when precipitation peaks (Peters et al., 2013).

Mean climate conditions today vary across the Himalaya; the western Himalaya is characterized by peak precipitation in winter and early spring, while the central Himalaya is dominated by the Indian Summer Monsoon (IM) and the eastern Himalaya by the East Asia Summer Monsoon (EASM) (Yao et al., 2013). Because of this heterogeneity, we separate the Himalayas into four distinct regions for analysis purposes, including the western Himalaya; a transitional area between western and central Himalaya; central Himalaya; and eastern Himalaya (transitional areas between central and eastern Himalaya are excluded because climate and isotopic signals are similar to IM and EASM regions). The strength and pattern of precipitation and wind, and isotopic compositions in the two eastern-most transitional areas are similar to those in the IM and EASM in most cases. Thus, in the following we present results only for the western, transitional, IM and EASM regions as shown in Fig. 2-2.

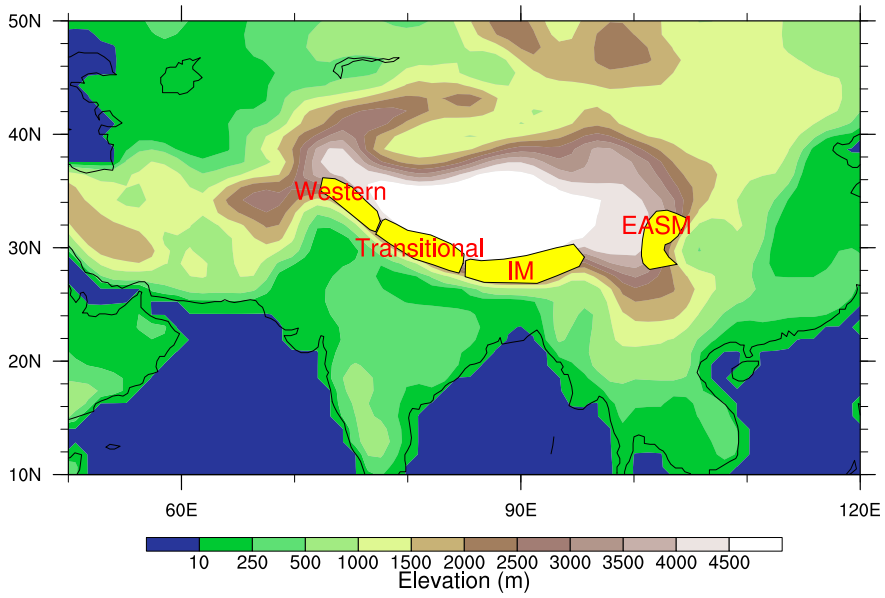

Figure 2-2 Topographic map (m) showing Himalayan climate zones

Topographic map (m) showing Himalayan climate zones after Yao et al. (2013). Western, transitional, Indian Summer Monsoon (IM), and Eastern Asian Summer Monsoon (EASM) regions are marked. Transitional areas between central and eastern Himalaya are excluded because climate and isotopic signals are similar to IM and EASM regions.

2.2.2 Rayleigh distillation

We developed an open-system, one-dimensional, altitude-dependent Rayleigh distillation model (RDM) in order to estimate decreases in $\delta^{18}O_p$ due to Rayleigh distillation during ascent. The RDM tracks the isotopic composition of an air parcel as it ascends adiabatically from low to

high altitude, becomes saturated, and loses condensate through precipitation. In the RDM, an air parcel cools at the dry adiabatic lapse rate before condensation and at the moist adiabatic lapse rate upon saturation (Rowley and Garzione, 2007). The RDM is run using terrain-following coordinates and is initialized with three different moisture sources: (1) fixed air temperature (T=20°C) and relative humidity (RH=80%), (2) local, summertime low-level T and RH from ECHAM5, and (3) fixed T=20°C and summertime RH from ECHAM5. In this way, we are able to quantify the influence due to total moisture source change ((1) minus (2)), and further decompose this influence into the changes in T ((3) minus (2)) or RH ((1) minus (3)).
In order to estimate how much of the mass flux of ^{18}O in total precipitation is contributed by the Rayleigh distillation process, we assumed that all large-scale precipitation, P_l, forms in response to stable upslope ascent and participates in Rayleigh distillation. We then estimated the isotopic flux of water undergoing Rayleigh distillation as:

$$RD = \left(\frac{\delta^{18}O_{RDM}}{1000} + 1\right) R_{vsmow} \times P_l \times \rho_{water}, \quad (1)$$

where RD has units of g m^{-2} h^{-1}; ρ_{water} (in g m^{-3}) is the density of water; P_l (in m h^{-1}) is the large-scale precipitation rate; $\delta^{18}O_{RDM}$ is the isotopic composition simulated by the RDM at the same elevation as the grid points in 2.2.3 where the mass flux in total precipitation is estimated. Note that this estimation of RD stands for the upper limit of the contribution of RD, since not all large-scale precipitation is triggered by the Rayleigh distillation process.

To compare the relative importance of Rayleigh distillation with other isotopic fractionation processes in ECHAM, we quantify the change in upslope $\delta^{18}O_p$ attributable to Rayleigh distillation. We do this by comparing the rate of upslope $\delta^{18}O_p$ change (hereafter referred to as the $\delta^{18}O_p$ lapse rates) in ECHAM with that estimated using the RDM. We define the $\delta^{18}O_p$ lapse rate as the slope of the linear regression equation of precipitation-weighted $\delta^{18}O_p$ regressed on elevation and use the coefficient of determination (R^2) of this regression to evaluate the robustness of the $\delta^{18}O_p$-elevation relationship. We use a ratio of the $\delta^{18}O_p$ lapse rate in ECHAM to that in the RDM (p_percent) to approximate the contribution of Rayleigh distillation to the ECHAM $\delta^{18}O_p$ lapse rate. When R^2 and p_percent are both above 0.5 for a particular domain and elevation scenario, we consider the ECHAM $\delta^{18}O_p$ lapse rate to agree with the RDM $\delta^{18}O_p$ lapse rate.

$\delta^{18}O_p$ decreases as an air parcel travels inland. This continental effect may contribute to a significant portion of the decrease in $\delta^{18}O_p$ over elevated regions in the low elevation scenarios. To evaluate whether a strong $\delta^{18}O_p$-elevation relationship exists in low-elevation scenarios, we examine the ratio of the slope of $\delta^{18}O_p$ regressed against latitude on the subcontinent to the south of the Himalayas to that on the Himalayan slope. This method accounts for the fact that $\delta^{18}O_p$ changes with both latitude and elevation. A significant $\delta^{18}O_p$-elevation relationship is signified by a large ratio, indicating that $\Delta\delta^{18}O_p$ with elevation is greater than that with latitude.

2.2.3 Quantifying effects through the mass flux of ^{18}O

Mass fluxes of ^{18}O are calculated to quantify the contribution of vapor mixing, surface recycling and RDM to the ^{18}O in total precipitation. Vapor mixing and surface recycling serve as the lateral and lower boundary sources of ^{18}O in an air column, and total precipitation as the sink. Within this air column, sinks and sources of ^{18}O in the air are assumed to compensate to make the total mass of ^{18}O in the air stable on climatological time scales, with the mass flux of ^{18}O from vapor mixing and surface recycling balancing that from total precipitation. With this compensation of sources and sinks in mind, we calculated the flux of ^{18}O due to vapor mixing, surface recycling and total precipitation.

The vapor mixing between air masses is estimated as the advection of ^{18}O in a vertical air column:

$$\frac{\partial M^{18}O}{\partial t} \sim \int -\vec{V} \cdot \vec{\nabla} m^{18}O \, dz, \tag{2}$$

where $M^{18}O$ (g m^{-2}) is the unit column-total mass of ^{18}O in the air; $\vec{V}$ (m h^{-1}) is the wind speed vector within a layer; $m^{18}O$ (g m^{-3}) is the mass of ^{18}O per m^3 of air, and z (m) is elevation. Approximating total mass of water by the amount of ^{16}O, $m^{18}O$ is defined in terms of $\delta^{18}O_c$ from (1) as:

$$m^{18}O \approx q\rho_{air}\left(\frac{\delta^{18}O}{1000}+1\right)R_{vsmow}\,. \tag{3}$$

By substituting $\delta^{18}O_c$ in (3) into (2), the final form of the total column-integrated vapor mixing (g m^{-2} h^{-1}) is written as:

$$VM = \int -\vec{V} \cdot \vec{\nabla} m^{18}O \, dz = -\int \vec{V} \cdot \vec{\nabla}\left[q\rho_{air}\left(\frac{\delta^{18}O}{1000}+1\right)R_{vsmow}\right]\rho_{air}dz\,. \tag{4}$$

Note that the centered-finite-difference method is used in discretizing the derivatives in Eq. (4). This method could potentially bring errors in comparison to the spectral method used in the dynamical core of ECHAM5.

Recycling of surface water vapor transports ^{18}O to the atmosphere from lower boundary. To estimate this contribution to ^{18}O, the recycled mass flux (in g m^{-2} h^{-1}) is calculated as:

$$\left(\frac{\delta^{18}O}{1000}+1\right) R_{vsmow} \times E \times \rho_{water}, \quad (5)$$

where $\delta^{18}O$ is the isotopic composition of the evaporated water and E (m h^{-1}) is the surface evaporation rate.

The mass flux of ^{18}O in total precipitation is estimated following (3) as:

$$\left(\frac{\delta^{18}O}{1000}+1\right) R_{vsmow} \times P \times \rho_{water}, \quad (6)$$

where $\delta^{18}O$ is the isotopic composition of precipitation and P (m h^{-1}) is the precipitation rate. Note that this method does not allow us to isolate within-column processes, including vertical mass exchanges through convective updrafts and downdrafts and through phase changes. We encourage future studies to isolate these within-column processes and how they evolve with topography.

2.3 Results

2.3.1 Model validation of ECHAM5-wiso

Under modern elevations, annual-mean precipitation-weighted $\delta^{18}O_p$ decreases with elevation on the Himalayan slope, increases with latitude across the Tibetan plateau (Fig. 2-3a, 2-4), and varies little (mostly within 2 ‰) on the northern Tibet slope (36° N-40° N) (Fig. 2-4). Li et al. (2016) demonstrated that ECHAM5 simulates $\delta^{18}O$ variations across the Himalaya and Tibetan Plateau that are in reasonable agreement with observed precipitation and stream values (see Methods). Consistent with stream water samples, the model captures a decrease in $\delta^{18}O_p$ along a north-south transect across the Himalayas and an increase in $\delta^{18}O_p$ on the Tibetan Plateau (see their Fig. 2-12d). The main discrepancy occurs on the northwestern Tibetan Plateau in winter and spring. Simulated $\delta^{18}O_p$ is 4 ‰ greater than stream sample values along a cross section extending westward from 85° E and centered on 30° N. Li et al. (2016) attributed this

mismatch to local factors, systematic model bias, and the influence of freshwater discharge from higher altitudes in the watershed.

We further compare ECHAM5 CNTL $\delta^{18}O_p$ with the modern surface water isotope dataset reported in Li and Garzione (2017) (Fig. 2-5). Co-located ECHAM and water sample $\delta^{18}O_p$ agree within 2 ‰ at 49.2% of sites, and within 3 ‰ at 73.3% of sites. Several discrepancies between simulated and observed $\delta^{18}O_p$ exist: Firstly, ECHAM5 $\delta^{18}O_p$ is lower than sampled $\delta^{18}O_p$ over northwestern Tibet (80° E-85° E, 35° N-37° N). This mismatch could be

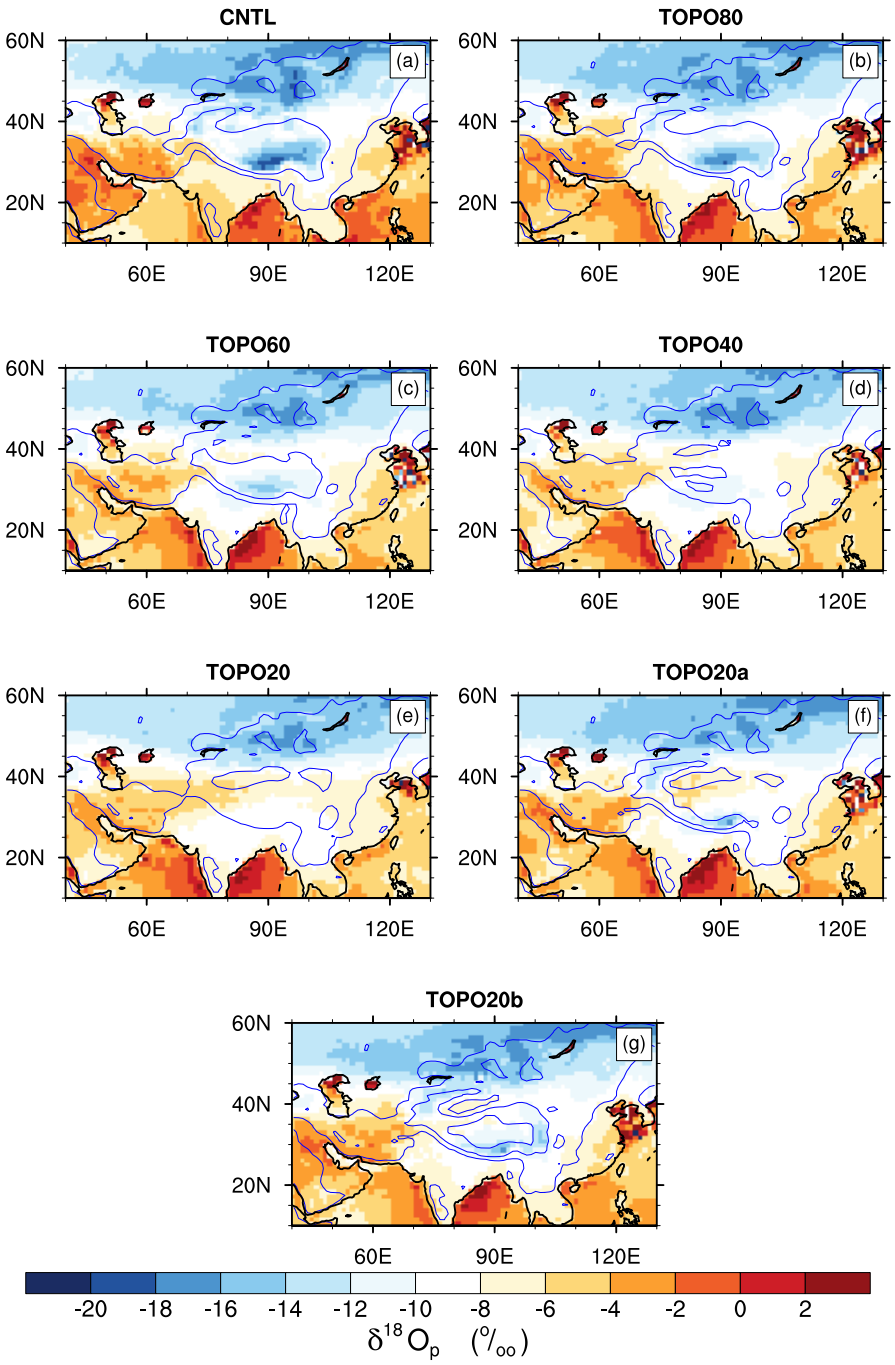

Figure 2-3 Mean-annual precipitation-weighted ECHAM stable oxygen isotope

$\delta^{18}O_p$ (in ‰) for cases (a) CNTL, (b) TOPO80, (c) TOPO60, (d) TOPO40, (e) TOPO20, (f) TOPO20a, (g) TOPO20b. Light blue contour lines represent 500 and 2000 m surface elevation contours.

associated with the higher relative humidity in ECHAM (Fig. A-1) than that in observations. This high relative humidity results in weaker evaporation both from land surface and below

cloud-base, lowering $\delta^{18}O$ in surface waters. Secondly, ECHAM5 $\delta^{18}O_p$ is more depleted, by 2-5 ‰, over east-central Tibet (89° E-102° E, 32° N-35° N). The LMDZ-iso model shows a similar

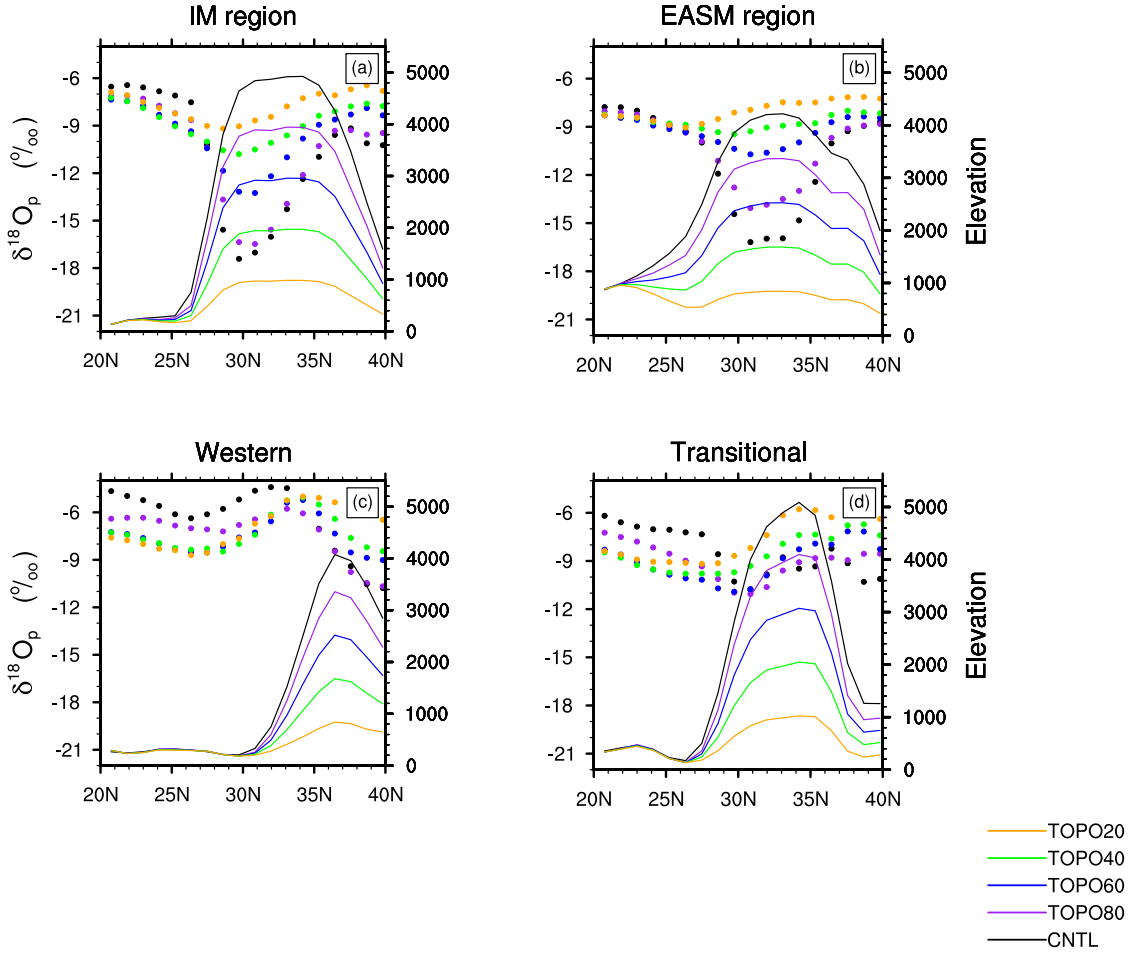

Figure 2-4 Stable oxygen isotopes along latitudinal transects

Annual-mean precipitation-weighted $\delta^{18}O_p$ (filled circles) and surface elevations (lines) along latitudinal transects for the (a) IM; (b) EASM; (c) western; and (d) transitional regions. These values represent zonal-average values over the specific region.

mismatch of 1-4 ‰ (Botsyun et al., 2016). In other regions of Tibet, simulated $\delta^{18}O_p$ in LMDZ-iso are very similar to those in ECHAM5, within 2‰ (Yao et al., 2013). There are two potential explanations for the mismatch from modern surface water over east-central Tibet. One possibility is that the sampled $\delta^{18}O_p$ does not reflect mean climatic conditions. We note that the water samples from the east-central and northern Tibet regions were collected over a short two-year span. This possibility is supported by the large inter-annual variability in $\delta^{18}O_p$ (up to 9 ‰) in both ECHAM (Li et al., 2016) and in precipitation sample spanning 1986 to 1992 from GNIP (AEA/WMO, 2017). The other source for the mismatch over east-central Tibet is from the higher

than observed precipitation simulated by ECHAM5, which can result in lower $\delta^{18}O_p$ through the amount effect (as shown in 2.3.6). The simulated summertime precipitation rate over east-central Tibet (89° E-102° E, 32° N-35° N) is 3.9 mm/day, higher than the CMAP value of 2.8 mm/day. This high precipitation is systematic and is also seen in other models, such as the LMDZ-iso (Botsyun et al., 2016) and ECHAM4 (Battisti et al., 2014).

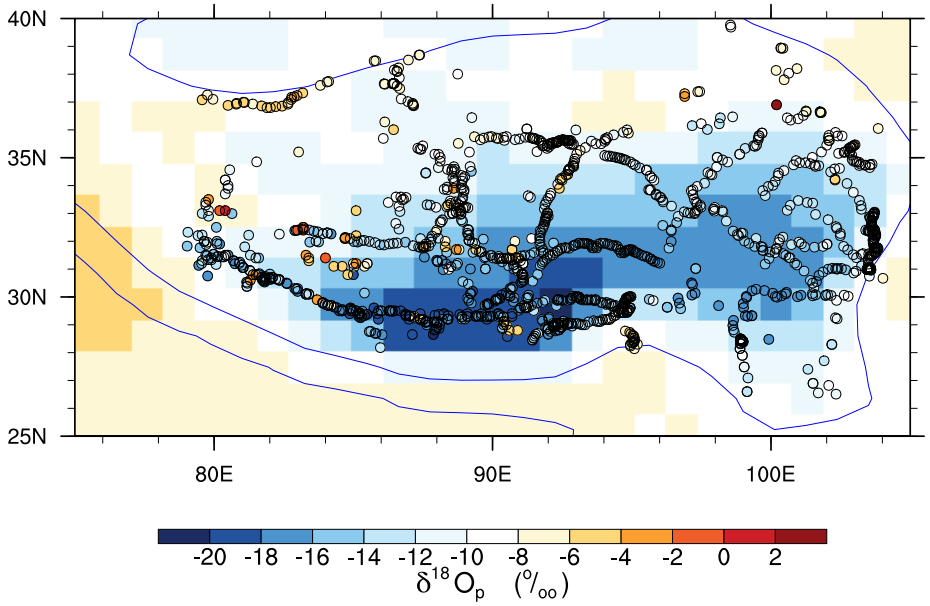

Figure 2-5 Validation of ECHAM stable oxygen isotopes

Comparison of annual-mean precipitation-weighted ECHAM $\delta^{18}O_p$ (shaded) with precipitation and stream samples (circles) from Li and Garzione (2016).

2.3.2 Climate response to Tibetan-Himalayan surface elevation

Numerous modeling studies have found that lowering the height of the Tibetan Plateau influences regional temperature, wind, precipitation, and relative humidity (e.g, Kitoh, 2004; Jiang et al., 2008). In this section, we describe regional climate changes on the western Himalayan slope, the Tibetan Plateau, the IM region and the EASM region, that occur as high elevations are lowered.

Under modern conditions, near-surface temperatures in the Tibetan-Himalayan region vary with elevation following a moist adiabatic lapse rate (~5 °C km^{-1}) (Fig. A-2) and range from >30 °C on the Indian subcontinent at the foot of the Himalaya to <10 °C across the Tibetan Plateau (Fig. A-3a). Lowering elevations in our experiments causes near-surface temperatures across the Tibet-Himalayan region to increase (Fig. A-3b-g) at approximately the lapse rate for

CNTL. As a result, temperature lapse rates vary little among elevation scenarios, for instance, ranging from 4.9-5.4 °C km^{-1} in the IM region (Fig. 2-1).

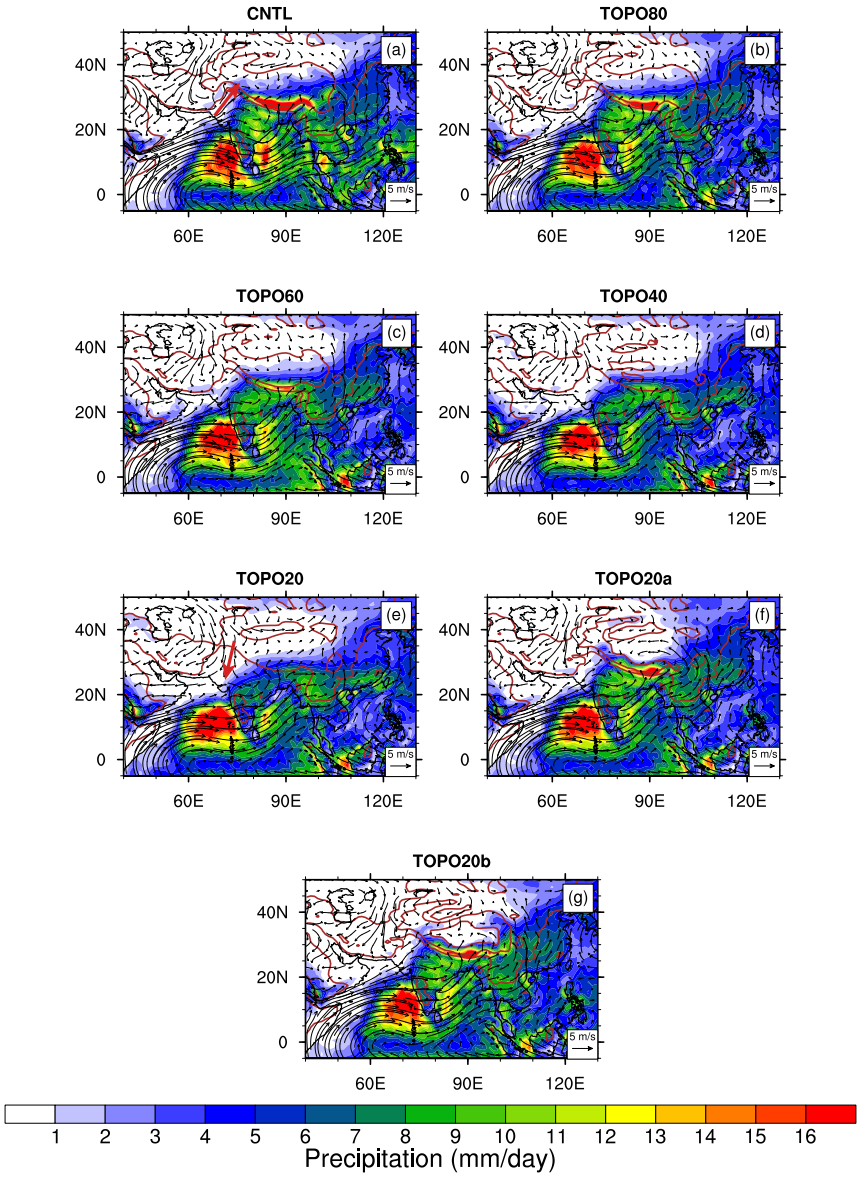

Figure 2-6 Summer precipitation and winds.

Summer (June-July-August) low-level (850 hPa) wind (arrows) and precipitation (shaded) for (a) CNTL (b) TOPO80, (c) TOPO60, (d) TOPO40, (e) TOPO20, (f) TOPO20a, and (g) TOPO20b cases. Brown contour lines represent 500 m and 2000 m surface elevation contours in the Tibetan region. The red arrows on the western Himalayan slope in (a) and (e) shows the wind direction reversal from CNTL to TOPO20.

Wind patterns, precipitation and RH respond dramatically to reductions in elevation. These changes vary across regions. On the western Himalayan slope, wind directions nearly reverse with southerly winds in the high-elevation scenarios switching to northwesterly winds in low-elevation scenarios (Fig. 2-6). This wind reversal results in transport of arid air from the

north, lowering total-column relative humidity by ~40%. With this substantial decrease in RH, summer precipitation decreases from ~3 mm day^{-1} in CNTL to ~0.1 mm day^{-1} on the western Himalayan slope in TOPO20. A similar decrease in RH, by ~20% from CNTL to TOPO20, is simulated on the Tibetan Plateau. Accompanying this reduction in RH, precipitation on the Tibetan Plateau decreases from ~4 mm day^{-1} in CNTL to ~1 mm day^{-1} in TOPO20. This reduction in Tibetan Plateau precipitation is linked to a weakening of the Asian monsoonal systems and moisture delivery through monsoonal winds.

The responses in the monsoonal regions are somewhat different from those on the western slope and Tibetan Plateau. A reduction in surface elevation (from CNTL to TOPO20) (Fig. 2-1) leads to weakening of the IM, as indicated by slowing of summer southwesterly winds over the Bay of Bengal and the Arabian Sea and a decrease in summer precipitation (by more than 20 mm day^{-1} in ECHAM) along the central Himalayas (Fig. 2-6). IM weakening is also demonstrated by the WSI1 monsoon index (Fig. 2-7, following Wang and Fan (1999)), which is defined by the vertical wind shear between the lower (850 hPa) and upper (200 hPa) troposphere in the region (5-20° N, 40-80° E) during summer. Monthly WSI1 index values (not shown) indicate that the Indian monsoon persists through all elevation scenarios, although summertime WSI1 (Fig. 2-7) shows that this Indian Monsoon weakens abruptly once elevations are reduced to between 40-60% of modern values, a threshold reported in previous modelling studies (e.g. Abe et al., 2003). As a result of IM weakening, total-column average RH decreases from >90% in CNTL to 70% in TOPO20 and summer precipitation decreases from >16 mm day^{-1} in CNTL to ~6 mm day^{-1} in TOPO20.

ECHAM5 captures a similar threshold behavior in monsoon activity in the EASM region. With lowering of the Himalayan front to 40% of its modern elevations, the broad humid belt that characterizes central China in high elevation scenarios (CNTL, TOPO80, TOPO60, TOPO20a and TOPO20b) shifts southward, resulting in an expanded arid belt in the region (in TOPO40 and TOPO20). This shift in precipitation is associated with a southward retreat of the southwesterly monsoonal winds that penetrate much of eastern Asia (Fig. 2-6d, e).

2.3.3 Climate response to Himalayan surface-elevation

ECHAM5 experiments TOPO20a and TOPO20b isolate the influence of Himalayan elevations on the regional climate. These experiments generally indicate that the Himalayas,

rather than the Tibetan Plateau, govern regional precipitation and circulation patterns. The IM and EASM are strong in both TOPO20a and TOPO20b. The IM is shown by strong low-level wind over the Arabian sea and heavy precipitation across both the Indian subcontinent and the central Himalayas in TOPO20a and TOPO20b (Fig. 2-6f,g). Likewise, the EASM in these simulations is similar to that in the CNTL as indicated by heavy precipitation to the north of Yangtze river and southerly winds penetrating central China (Fig. 2-6f,g).

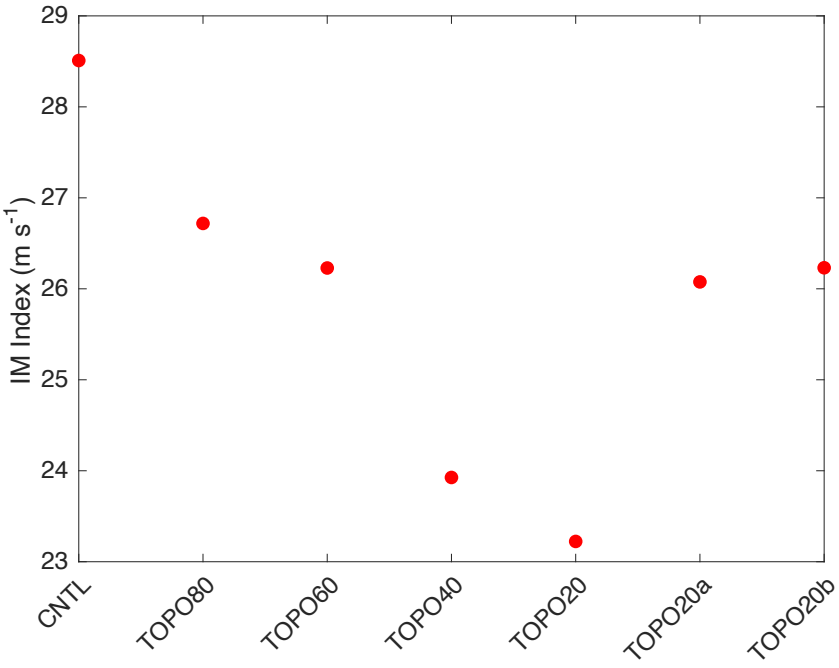

Figure 2-7 Indian Summer Monsoon index

Indian Summer Monsoon (June-July-August) index, WSI1, calculated as the vertical wind shear between the lower (850 hPa) and upper (200 hPa) troposphere in the region (5-20° N, 40-80° E).

To further elucidate the contribution of the Himalaya to monsoonal dynamics, we calculated the equivalent potential temperature (Fig. A-4), which is commonly used to denote the location of monsoonal heating for the Indian Monsoon. In TOPO20a and TOPO20b, the equivalent potential temperature maxima are reduced but in a similar location as in the CNTL case, supporting our conclusion that the Himalayas are the dominant driver of the IM. When the Himalayas are lowered, monsoonal heating decreases and the locus shifts southeastward as cold, dry extratropical air moves southward and mixes with warm, humid subcontinental air, consistent with the results in Boos (2015), though the extent of the shift is smaller in ECHAM5.

In contrast to this well-established mechanism for the Indian Monsoon, the mechanism for the southward shift of the EASM is not well understood. Uplift of the Himalaya-Tibet orogen (Guo et al., 2008; Liu et al., 2017), retreat of the Paratethys (Guo et al., 2008), and forcing by atmophere pCO_2 (Licht et al., 2014; Caves Rugenstein and Chamberlain, 2018) have been proposed as possible factors triggering this southward shift, though the timing for this shift is highly debated from Eocene to early Miocene. Our simulation of a strong EASM over central China in both TOPO20a and TOPO20b suggests that uplift of the central and western Himalaya would have been capable of forcing this southward shift.

2.3.4 Moisture source influence on RDM $\delta^{18}O_p$

Under lower elevation scenarios, $\delta^{18}O_p$ values increase relative to the modern elevation scenario both on the Himalayas and the Tibetan Plateau (Fig. 2-4). The rate of change of $\delta^{18}O_p$ with elevation and latitude decreases substantially in the monsoonal regions as Tibetan-Himalayan elevations are reduced (Fig. 2-4a, b).

Table 2-1 Contribution of physical processes

Contribution of physical processes to annual-mean precipitation-weighted $\delta^{18}O_p$ (all units in ‰) averaged over monsoonal regions (IM and EASM). In the table, RDM_{ECHAM} represents RDM initiated using the moisture sources (i.e. air temperature and relative humidity) from ECHAM5; RDM_{Fixed} is the $\delta^{18}O_p$ simulated by RDM initiated with fixed moisture source of T=20°C and RH=80%; and RDM_{Fixed_T} is initiated with fixed T=20°C and ECHAM RH (refer to section 2.2 for more details on the three different moisture sources). All columns show values averaged from mountain foot to mountain peak, except for the 2nd column showing the difference in $\delta^{18}O_p$ between mountain peak and foot as simulated by RDM_{ECHAM}.

Case	RDM_{ECHAM} peak – foot (‰)	RDM_{ECHAM} – ECHAM5 (‰)	RDM_{Fixed} – RDM_{ECHAM} (‰)	RDM_{Fixed_T} – RDM_{ECHAM} (‰)	RDM_{Fixed} – RDM_{Fixed_T} (‰)
CNTL	-8.00	0.88	-0.32	-1.52	1.20
TOPO80	-6.15	1.89	1.73	-0.96	2.70
TOPO60	-4.16	1.80	2.25	-1.00	3.25
TOPO40	-2.53	0.86	2.34	-1.23	3.57
TOPO20	-1.12	-0.30	1.86	-1.51	3.37

The oxygen isotope compositions of precipitation on mountain slopes are traditionally assumed to systematically decrease in response to adiabatic cooling, condensation, and rainout of

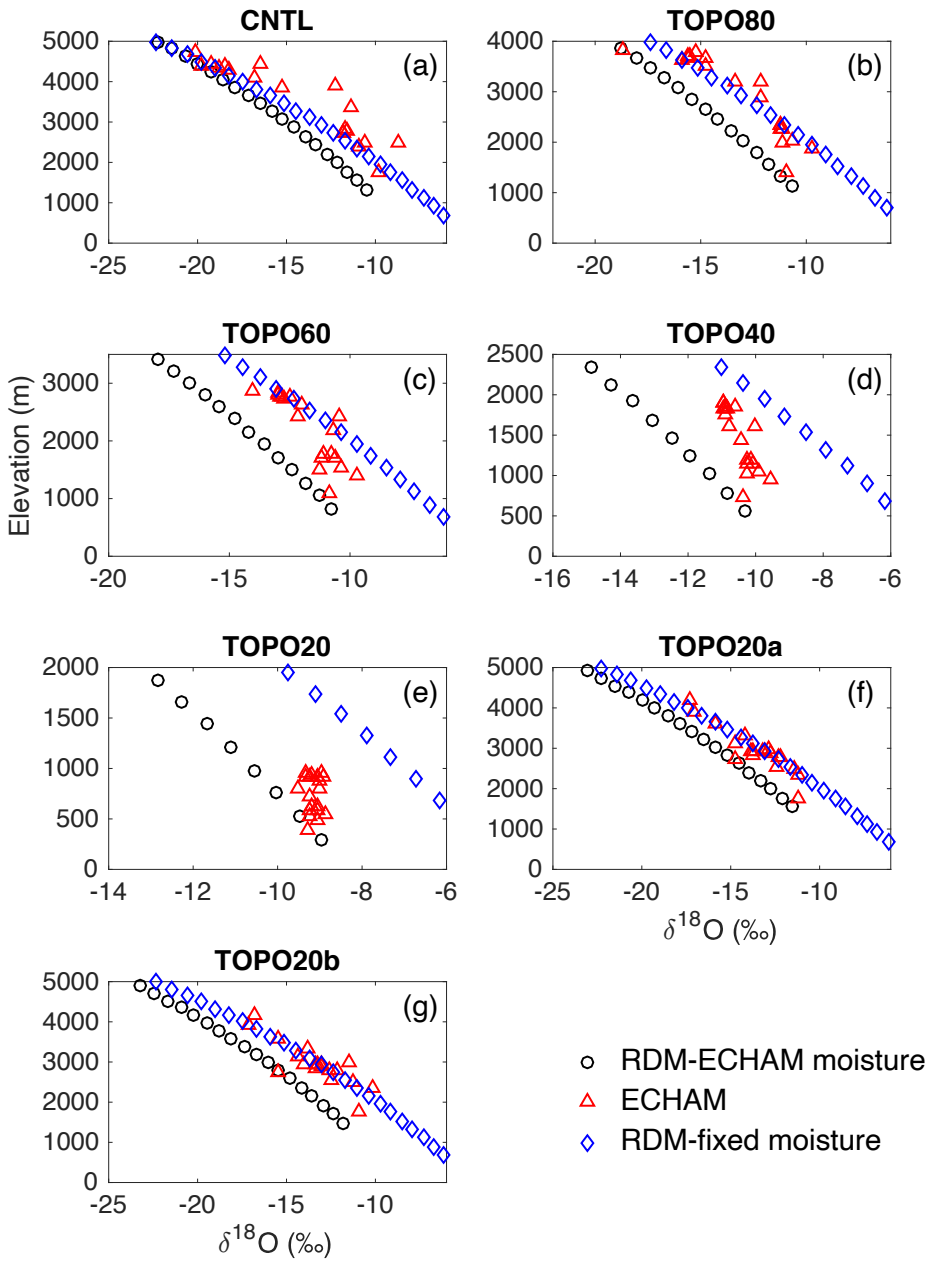

Figure 2-8 Stable oxygen isotope versus elevation for the Indian Summer Monsoon region

$\delta^{18}O_p$ (‰) versus elevation (m) for the Indian Summer Monsoon (ISM) region of the southern Himalayan flank as simulated by ECHAM5 (blue triangle, annual-mean precipitation-weighted), RDM initiated with ECHAM5 summertime moisture sources (black circle) and RDM initiated with fixed moisture sources of T=20°C and RH=80% (red diamond) for the (a) CNTL, (b) TOPO80, (c) TOPO60, (d) TOPO40, (e) TOPO20, (f) TOPO20a, and (g) TOPO20b cases.

ascending air parcels, a process described by Rayleigh distillation and the basis for the application of $\delta^{18}O_p$-paleoaltimetry. In this section, we evaluate the degree to which Rayleigh distillation accounts for up-slope decreases in $\delta^{18}O_p$ by comparing RDM to ECHAM $\delta^{18}O_p$ in

four separate regions (Fig. 2-2). Note that the northern Tibet slope is excluded here because most of the northerly air is diverted rather than being forced to ascent (Fig. 2-6).

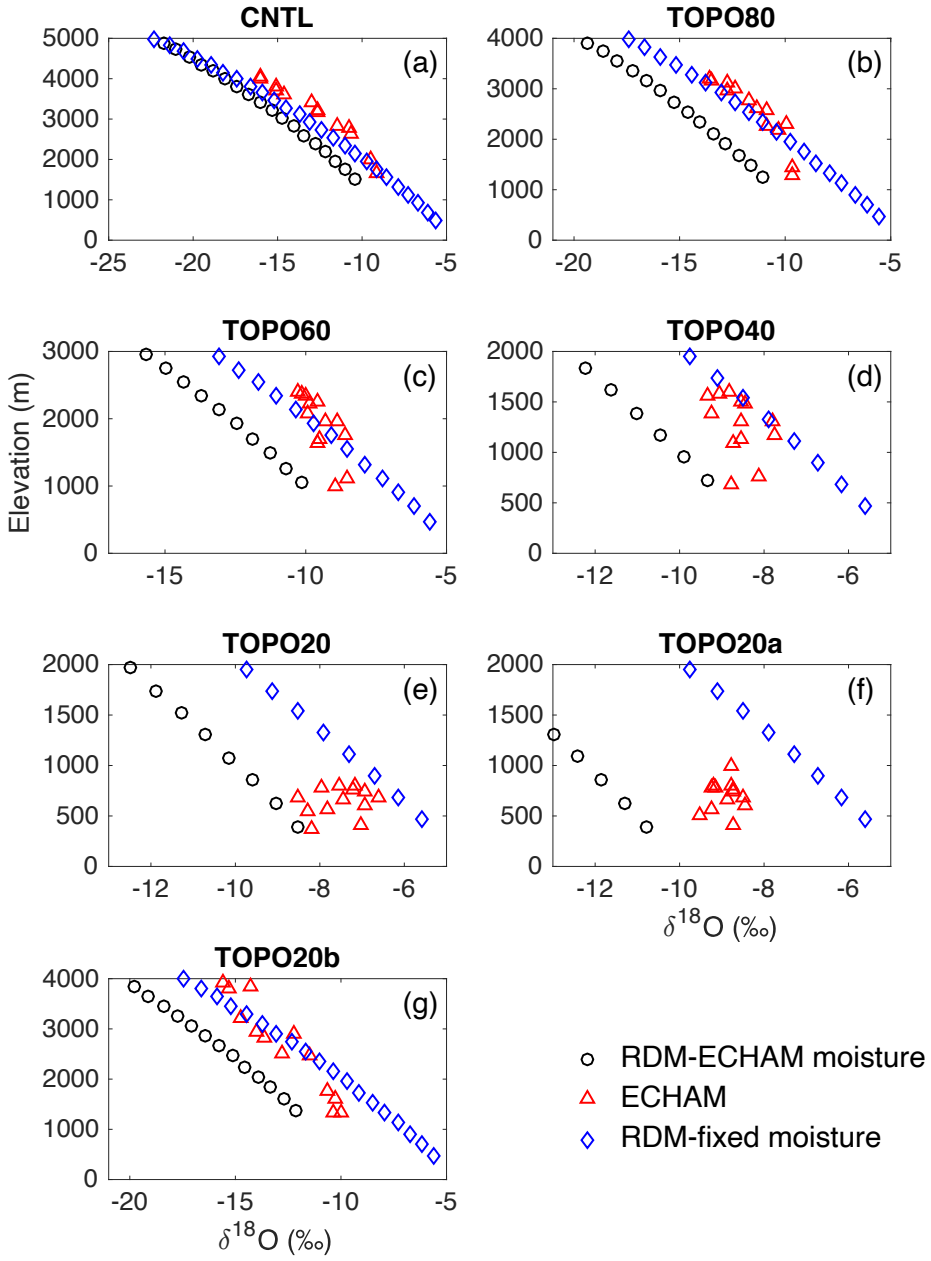

Figure 2-9 Stable oxygen isotope versus elevation for the East Asia Summer Monsoon region

Same as in Figure 2-8 but for the East Asian Summer Monsoon (EASM) region of the southern Himalayan flank.

For each of the four regions, we initialize the RDM with both fixed moisture sources (with initial T=20°C and RH=80%) as in paleoaltimetry studies and with ECHAM moisture sources (with T and RH that varies by region and case). The $\delta^{18}O_p$ predicted by the RDM using each moisture source is shown in Fig. 2-8 & 2-9 (red diamonds vs. black circles). With ECHAM-

derived T and RH, the RDM $\delta^{18}O_p$ values are close to those simulated by ECHAM5 in all elevation scenarios (Fig. 2-8 & 2-9, Table 2-1, 3rd column). RDM $\delta^{18}O_p$ with ECHAM-derived moisture is 0-2 ‰ less than that with fixed T and ECHAM RH (Table 2-1, 4th column), except in the CNTL scenario where the two RDM $\delta^{18}O_p$ are very close. The lower $\delta^{18}O_p$ is due to the fact that the RH of the initial air parcel is lower in ECHAM than in the prescribed case (Fig. A-1). The impact of moisture source differences on $\delta^{18}O_p$ is further decomposed in Table 2-1 to estimate the contributions adiabatic temperature versus RH changes. As seen in Table 2-3, the effect of adiabatic temperature changes is consistently small (~−1 ‰) across all elevation scenarios, reflecting the fact that temperature lapse rates vary little among elevation scenarios (Fig. A-2). In contrast, as the initial RH decreases with lowering of elevation, ECHAM-sourced $\delta^{18}O_p$ is lowered by as much as 3.5 ‰ (Table 2-1, last column). In sum, these results demonstrate that elevation-related changes in moisture source characteristics substantially impact RDM $\delta^{18}O_p$ estimates.

2.3.5 Performance of ECHAM-sourced Rayleigh distillation in the Himalayans

Our estimates using an RDM implicitly assume that Rayleigh distillation is the dominant process controlling the $\delta^{18}O_p$-elevation relationship. To test this assumption, we compare ECHAM-sourced RDM $\delta^{18}O_p$ and ECHAM5 $\delta^{18}O_p$.

Decreases in $\delta^{18}O_p$ with elevation in ECHAM and the RDM generally agree under high-Himalaya scenarios and are consistent with modern observations (Table 2-2). Under modern topographic scenarios for the western Himalaya (Fig. A-5) and the monsoonal regions (Fig. 2-8 & 2-9), R^2 and p_percent values are greater than 0.77 and 0.51, indicating that RDM and ECHAM $\delta^{18}O_p$ match well. R^2 and p_percent values are similarly high, above 0.68 and 0.53, for the western Himalaya and the monsoonal regions in high-Himalaya scenarios (TOPO80, TOPO60, TOPO20a, and TOPO20b in the IM region; TOPO80, TOPO20b in the EASM region) again indicating a good match between ECHAM and RDM $\delta^{18}O_p$ and suggesting that Rayleigh distillation drives isotopic compositions in these regions.

In other regions and under low-elevation scenarios, however, the comparison between RDM and ECHAM $\delta^{18}O_p$ is poor (Table 2-2). For instance, on the western Himalayas, in the TOPO80 case (Fig. A-5), the lapse rate of ECHAM $\delta^{18}O_p$ is much smaller than the lapse rate

predicted by the RDM (Fig. A-5), as shown by p_percent values of less than 0.15. Under even lower elevation scenarios (TOPO60, TOPO40, TOPO20), orographic precipitation is not triggered over the Himalayas (Fig. A-4c-e), making the RDM an unsuitable representation of precipitation processes. In the transitional region, the $\delta^{18}O_p$ can vary by more than 5‰ at a specific elevation under all elevation scenarios (Fig. A-6). This large spread is represented by a low R^2 value of 0.12 for the CNTL case, and even lower values (less than 0.10) for other topographic scenarios. In TOPO40 and TOPO20, ECHAM $\delta^{18}O_p$ shows little relationship with elevation (Fig. 2-4d).

In the monsoonal regions, the relationship between ECHAM5 $\delta^{18}O_p$ and elevation is weak in low elevation scenarios (Table 2-2 and Fig. 2-4) and compares poorly with the RDM. In the IM region, p_percent values for the TOPO40 and TOPO20 are less than 0.29. In the EASM region, ECHAM5 $\delta^{18}O_p$ is higher than RDM $\delta^{18}O_p$ (Fig. 2-8 & 2-9) in the TOPO60 scenario and the agreement is low (with p_percent value of 0.31). Under even lower elevation scenarios (TOPO40 and TOPO20), ECHAM $\delta^{18}O_p$ shows no relationship with elevation (Table 2-2 and Fig. 2-4b) and also compares poorly with the RDM (with p_percent less than 0.29).
Among the high-Himalaya-low-Tibet cases (TOPO20a and TOPO20b), RDM and ECHAM $\delta^{18}O_p$ match well in the IM region. The match is similarly good for TOPO20b in the EASM region. However, in the case with a low eastern flank (TOPO20a), the comparison is poor with an R^2 of 0.006 and a p_percent of −0.05.

Table 2-2 Summary of the comparison between ECHAM and RDM

Summary of the comparison between ECHAM and RDM $\delta^{18}O_p$ lapse rates under different topographic scenarios in different climate regions. Regions and scenarios with high R^2 and p_percent are marked with an "X" indicating the existence of a significant $\delta^{18}O_p$-elevation relationship (see methods in section 2.2 for definitions of R^2 and p_percent).

Region	CNTL	TOPO80	TOPO60	TOPO40	TOPO20	TOPO20a	TOPO20b
Western	X					X	X
Transitional							
IM	X	X	X			X	X
EASM	X	X					X

2.3.6 Factors influencing $\delta^{18}O_p$-elevation relationship on the Himalayan slope

As shown in 2.3.5, Rayleigh distillation cannot explain $\delta^{18}O_p$ variations with elevation for most regions in the reduced elevation (TOPO40, TOPO20) scenarios and in many regions

under higher elevation scenarios (TOPO80, TOPO60). To understand the factors influencing $\delta^{18}O_p$, we quantify the mass fluxes of ^{18}O (Fig. 2-10), distinguishing the processes that increase the mass flux of ^{18}O of the column (mixing and surface recycling) from those that decrease it (Rayleigh distillation and convective rainfall). Note that this method of taking the vertical column as a whole does not isolate the processes occurring within the air column (e.g. sub-cloud re-evaporation, vertical advection and mixing); this limitation does not impact our ability to identify the contributions of Rayleigh distillation and local processes. The results from this method yield very different contributions on the western slope from those in other regions, thus, the western Himalayas are reported separately.

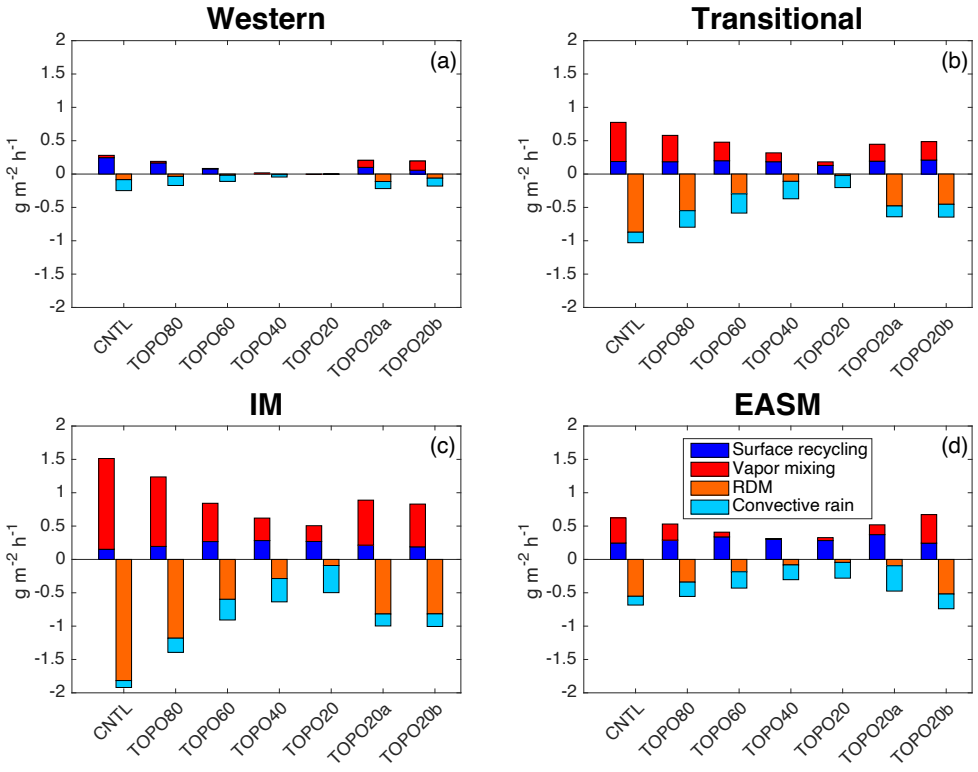

Figure 2-10 Summertime mass flux of stable water isotope in the Himalayas

Summertime mass flux of ^{18}O (g m^{-2} h^{-1}) for the (a) western Himalayas, (b) the transitional, (c) IM and (d) the EASM regions. Sources (positive values) and sinks (negative values) balance within 20% or 0.1 g m^{-2} h^{-1} for fluxes that are close to zero. (Small errors in the net balance arise due to the centered finite-difference method used to calculate derivatives in the advection terms.) Note that the largest source and sink varies by region and with elevation. Local convection and surface recycling are the dominant source and sink of ^{18}O in the western Himalayas and under low-elevation scenarios, while Rayleigh distillation and vapor mixing dominate in high-elevation scenarios in the monsoonal and transitional regions.

On the western Himalayas, local surface recycling and convective rainfall contributes substantially to the total mass flux of $^{18}O_p$ in the highest elevation scenarios (Fig. 2-10a). The contributions from these processes account for the poor match between RDM and ECHAM

$\delta^{18}O_p$ in this region. In the TOPO20a and TOPO20b scenarios, enhanced transport of enriched vapor from the south (see Fig. A-7, 1 of 42 trajectories in CNTL versus 11 and 13 of 42 in TOPO20a and TOPO20b) increases the contribution from vapor mixing.

Table 2-3 Isotopic contributions on the Tibetan Plateau

The isotopic contribution (in ‰) due to summertime sub-cloud re-evaporation and surface recycling on the Tibetan Plateau for different elevation scenarios.

	CNTL	TOPO80	TOPO60	TOPO40	TOPO20
Sub-cloud re-evaporation	9.06	10.02	7.97	5.21	5.28
Surface recycling	0.09	0.14	-1.40	-2.67	-1.8

In the monsoonal regions and the transitional region, vapor mixing is the predominant source of ^{18}O under high-elevation scenarios and reflects the advection of ^{18}O-enriched vapor from the Arabian Sea and Bay of Bengal. This mass flux of vapor mixing decreases substantially with a reduction in elevation, whereas the mass flux of surface recycling remains approximately constant in all elevation scenarios. As a result, surface recycling is as or more important than mixing as a source of ^{18}O under low-elevation scenarios (Fig. 2-10c, d). This change in relative importance of the two sources represents an increase in the importance of local versus remote sources as monsoon strength weakens under low-elevation scenarios.

In high elevation scenarios, Rayleigh distillation acts as the dominant sink of ^{18}O in the monsoonal regions causing $\delta^{18}O$ to decrease markedly with elevation (Fig. 2-10c,d). Under reduced elevation scenarios, the absolute mass flux from Rayleigh distillation decreases, as large-scale precipitation due to stable upslope ascent decreases and convective precipitation increases (Fig. 2-11). With reduced elevation, the percentage of large-scale precipitation to total precipitation falls from 86% to 18% in the transitional region, from 93% to 18% in the IM region and from 80% to 15% in the EASM region, mirroring the decrease in the mass contribution of Rayleigh distillation, which falls from 85% to 11% in the transitional region, from 93% to 22% in the IM region and from 80% to 18% in the EASM region. As a result of the reduction in (large-scale) precipitation by stable upslope ascent, convective precipitation becomes the largest ^{18}O sink in TOPO20 and TOPO40 in both the transitional region and the IM region, and in TOPO60, TOPO40, TOPO20 and TOPO20a in the EASM region. These are also the scenarios

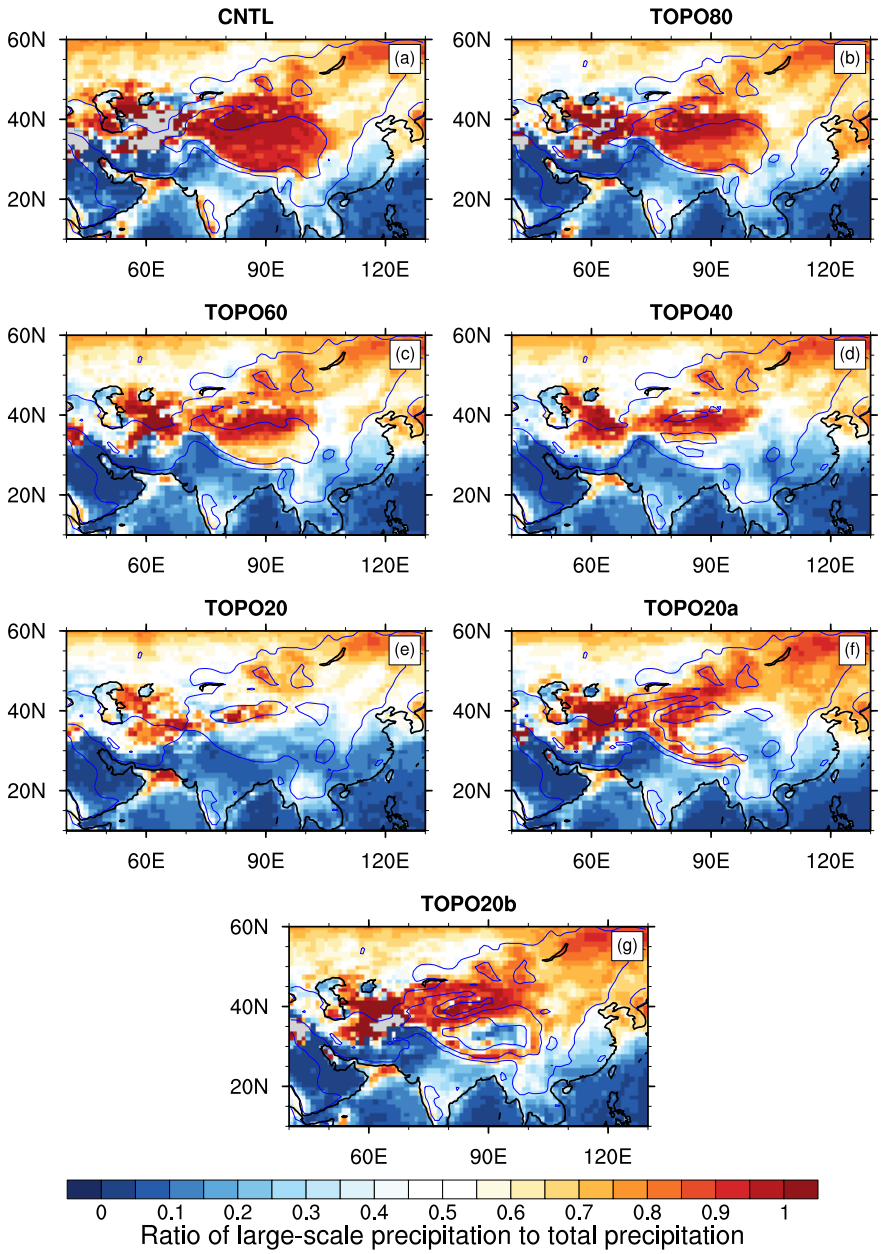

Figure 2-11 Ratio of summer large-scale to total precipitation

Ratio of summer large-scale to total precipitation rate in the (a) CNTL, (b) TOPO80, (c) TOPO60, (d) TOPO40, (e) TOPO20, (f) TOPO20a, and (g) TOPO20b cases. Light blue lines mark the 500 and 2000 m elevation contours in each case. In the Himalayas, this ratio decreases when mountain elevations are reduced. As a result, large-scale precipitation is dominant in high-elevation scenarios, but not in low-elevation scenarios.

that exhibited a poor match between RDM $\delta^{18}O_p$ and ECHAM $\delta^{18}O_p$ (Sect. 2.3.5). The increase in convective rainfall in these cases leads to greater kinetic fractionation through sub-cloud evaporation of falling rain, which is only partially equilibrated with the surrounding vapor (see 2.2.1), and an enrichment in the isotopic composition of rain. The RDM does not capture this

enrichment because it does not include sub-cloud evaporation. A similar reduction in large-scale precipitation with reduction in elevation is also captured in the Andes region (Insel et al., 2009) and is associated with a decrease in the rate of change of $\delta^{18}O_p$ with elevation.

Note that, although Rayleigh distillation is the primary sink under high-elevation scenarios, RDM $\delta^{18}O_p$ does not match ECHAM $\delta^{18}O_p$ well in the transitional region because of the large spread in ECHAM $\delta^{18}O_p$ (Fig. A-6). This spread is due to the bifurcated sources from northwest India (relatively enriched) and the Bay of Bengal (relatively depleted), since air parcels follow separate trajectories before mixing at the peak (Fig. A-7).

In sum, the mismatch between RDM and ECHAM $\delta^{18}O_p$ is caused by a weakening of Rayleigh distillation under low-elevation scenarios, triggered by a reduction in large-scale precipitation.

2.3.7 $\delta^{18}O_p$-latitude relationship on the Tibetan Plateau

In contrast to $\delta^{18}O_p$ on the Himalayas, $\delta^{18}O_p$ on the Tibetan Plateau increases linearly with latitude. It has been proposed that past $\delta^{18}O_p$, reconstructed from isotopic analyses of ancient soil and lake carbonates, could provide information about past elevations on the Tibetan Plateau after removing the modern meridional $\delta^{18}O_p$ gradient (Bershaw et al., 2012). This proposal is problematic because the meridional $\delta^{18}O_p$ gradient and the processes that set this gradient on the Tibetan Plateau are poorly understood today and were likely different in the past in ways that are not known.

Tibetan Plateau meridional $\delta^{18}O_p$ gradients simulated by ECHAM5 under modern and reduced elevation scenarios are shown in Fig. 2-12. The average meridional gradient in CNTL is 0.95 ‰/°, very close to the observed gradient of 1.09 ‰/° (Li and Garzione, 2017). Three features of the latitudinal $\delta^{18}O_p$ gradients are notable. Firstly, the gradient varies with longitude (Fig.2-12a, b) and variations are larger in high-elevation cases (e.g. from 1.90 ‰/° to 0.20 ‰/° in CNTL). Secondly, a linear fit is generally good with a high coefficient of determination ($R^2 >$ 0.8) east of 85°W for all cases but TOPO20a and TOPO20b (Fig. A-8). The high goodness of fit indicates a robust $\delta^{18}O_p$-latitude relationship for the cases with uniform reductions in topography. The poor fit in TOPO20a and TOPO20b is due to the larger variations in elevation

across the Tibetan Plateau. In these two cases, dry conditions (Fig. A-1) on the steep leeward side of the Himalaya favor strong below cloud-base re-evaporation, increasing local latitudinal

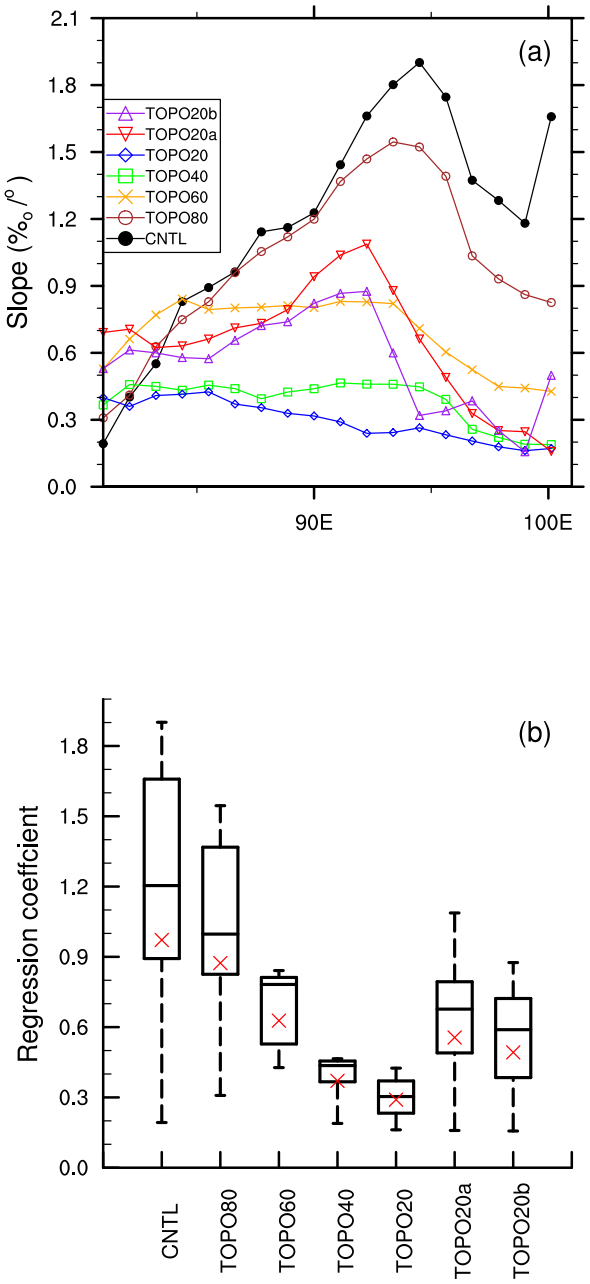

Figure 2-12 Linear regression of stable oxygen isotope with latitude on the Tibetan Plateau

(a) The slope (in ‰/°) of linear regression of annual-mean precipitation-weighted $\delta^{18}O_p$ on latitude from ECHAM5 output, used as an approximation for the meridional gradient of $\delta^{18}O_p$. (b) Boxplot shows the variability of the meridional gradient of $\delta^{18}O_p$. Red "x" indicates mean values for each scenario, calculated by regressing longitudinally averaged $\delta^{18}O_p$ across the Tibetan Plateau on latitude. Box plots show minimum, maximum, median, and quartile values.

$\delta^{18}O_p$ gradients. Lastly, in cases with uniform lowering of topography, the median meridional gradient (Fig. 2-12b) decreases almost linearly with reductions from 100% to 60% of modern

topography, changes more abruptly between 60% and 40%, and varies little once the topography is lowered below the monsoon threshold in TOPO40 and TOPO20.

The modern latitudinal $\delta^{18}O_p$ gradient on the Tibetan Plateau has been attributed to both surface recycling and sub-cloud re-evaporation. Surface recycling increases $\delta^{18}O_p$ by adding more enriched vapor from the land surface, while sub-cloud evaporation enriches ^{18}O in precipitation by partial evaporation of falling raindrops in an unsaturated air column. To understand the cause of the decline in the meridional $\delta^{18}O_p$ gradient, we quantified both the sources of ^{18}O (surface recycling and vapor mixing) and the isotopic contribution due to sub-cloud re-evaporation. Sub-cloud evaporation is quantified separately because this effect is contained in but cannot be isolated from the sources of ^{18}O.

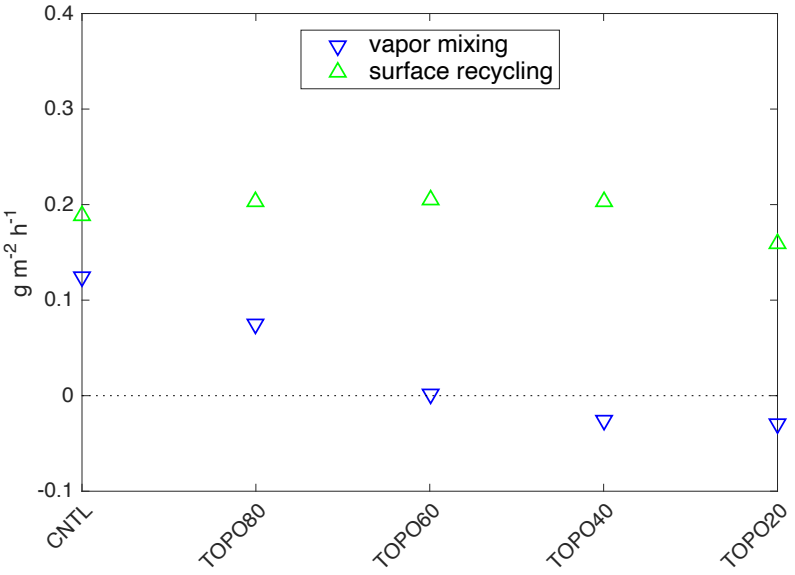

Figure 2-13 Mass flux of stable oxygen isotope on the Tibetan Plateau

The mass flux of ^{18}O (g m^{-2} h^{-1})) from summertime (June-July-August) vapor mixing and surface recycling on the Tibetan Plateau. Note positive (negative) values indicate sources (sinks) of ^{18}O. Surface recycling is the largest sources of ^{18}O under all elevation scenarios. Vapor mixing is secondary as a source in high-elevation scenarios and becomes a sink in low-elevation scenarios.

Surface recycling is the primary source of ^{18}O on the Tibetan Plateau with largely consistent contributions under all elevation scenarios (Fig. 2-13). The mass flux of ^{18}O due to vapor mixing is small and becomes a sink in low-elevation scenarios, since there are increasingly more depleted sources from the south in these scenarios (e.g., 17 out of 42 in CNTL vs. 30 out of 42 in TOPO20 for one location (33° N, 90° E)). To further quantify the contribution of surface

recycling to total precipitation, we subtracted $\delta^{18}O$ in precipitation from $\delta^{18}O$ in recycled vapor and normalized by the amount of precipitation and recycled vapor as in the equation:

$$\left(\delta^{18}O_s - \delta^{18}O_p\right) \times E/P \times \rho_{water}, \quad (7)$$

where $\delta^{18}O_p$ is the isotopic composition in precipitation; $\delta^{18}O_s$ is the condensate of recycled vapor; E (m h^{-1}) is the surface evaporation rate and P (m h^{-1}) is the total precipitation rate. Results from Eq. (7) show that $\delta^{18}O$ of surface recycling contributes less than 0.1 ‰ in CNTL and slightly more (−2.67 ‰) in TOPO20 (Table 2-3). The overall small contribution from surface recycling in ECHAM5 is due to the fact that $\delta^{18}O$ values in soil are similar to those in precipitation (Fig. A-9). This small contribution grows in low-elevation scenarios due to the increased fraction of evaporated vapor to total precipitation (Fig. A-10). Nonetheless, surface recycling plays a secondary role in decreasing the meridional $\delta^{18}O_p$ gradients.

Sub-cloud re-evaporation occurs within an unsaturated air column as falling raindrops undergo kinetic fractionation and become isotopically enriched (Stewart, 1975). Enrichment is reduced in heavier rain where the relative humidity is high, resulting in the observed anti-correlation between $\delta^{18}O_p$ and precipitation rate referred to as the amount effect. To quantify this enrichment due to sub-cloud re-evaporation, we show $\delta^{18}O_p$ against daily precipitation (Fig. 2-14). The slope of this $\delta^{18}O_p$-precipitation relationship denotes the strength of the amount effect. In low-elevation scenarios, the $\delta^{18}O_p$-precipitation slope is shallower (Fig. 2-14), indicating a weaker amount effect and stronger sub-cloud re-evaporation even at high precipitation rates.

This shallow slope of sub-cloud evaporation results in the shallower meridional $\delta^{18}O_p$ gradient on the Tibetan Plateau in low-elevation scenarios. In each individual elevation scenario, the enrichment of $\delta^{18}O_p$ due to sub-cloud evaporation is stronger at higher latitudes since there are more events of lower precipitation rates at higher latitudes than at lower latitudes (Fig. 2-15). As a result of this different distribution of precipitation, rainfall at higher latitudes is more enriched than that at lower latitudes. To further compare this contribution of sub-cloud re-evaporation with surface recycling, the excess enrichment of $\delta^{18}O_p$ due to sub-cloud re-evaporation is quantified by the $\delta^{18}O_p$ difference at high and low precipitation rates, weighted by precipitation rates (Table 2-2 & 2-3). The excess enrichment due to sub-cloud re-evaporation is much larger than that due to surface recycling and decreases with reduced elevation.

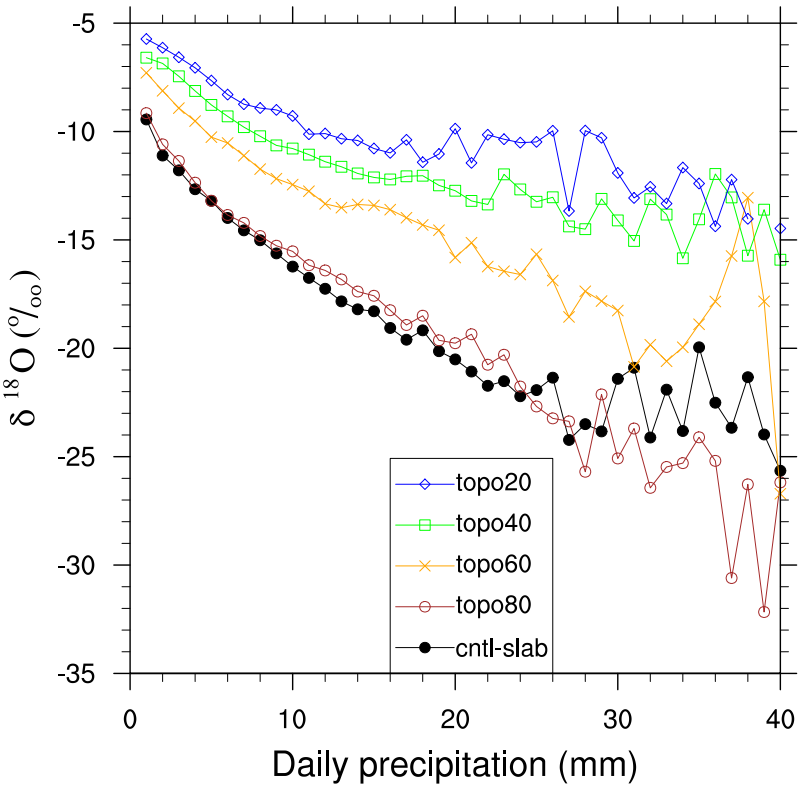

Figure 2-14 The amount effect on the Tibetan Plateau

ECHAM $\delta^{18}O_p$ (‰) versus daily summertime precipitation rate (mm/day) on the Tibetan plateau. ECHAM $\delta^{18}O_p$ decreases with increasing precipitation under all elevation scenarios, but is greatest in high-elevation scenarios than in low-elevation scenarios.

To explain this stronger sub-cloud re-evaporation in low-elevation scenarios, we refer to the kinetic fractionation process in ECHAM5 during partial evaporation of raindrops. As shown in Hoffmann et al. (1998), kinetic fractionation in ECHAM5 is formulated as:

$$\alpha = \frac{RH}{\frac{D}{\widehat{D}}(RH-1)+1}, \tag{8}$$

where α is the fractionation factor; $D \times \widehat{D}^{-1}$ represents the ratio of diffusivities between ^{16}O and ^{18}O and has the constant value of 0.9727; *RH* is the effective relative humidity of the grid box. To estimate how this kinetic fractionation changes between different elevation scenarios, we approximated the effective relative humidity to be the total-column-averaged RH. As seen in Fig. A-11, the total-column-averaged RH at any given precipitation rate is higher in high-elevation scenarios than that in low-elevation scenarios. Specifically, when the precipitation rate is very high at 40mm day^{-1}, the RH is at ~100% in CNTL, suggesting very little kinetic fractionation and weak sub-cloud re-evaporation. In comparison, in TOPO20 the RH is much lower at ~85%, indicating the presence of sub-cloud re-evaporation even at high precipitation rates.

In sum, meridional $\delta^{18}O_p$ gradients on the Tibetan Plateau decrease with lower elevation, and this reduction is due to stronger sub-cloud evaporation in low-elevation scenarios.

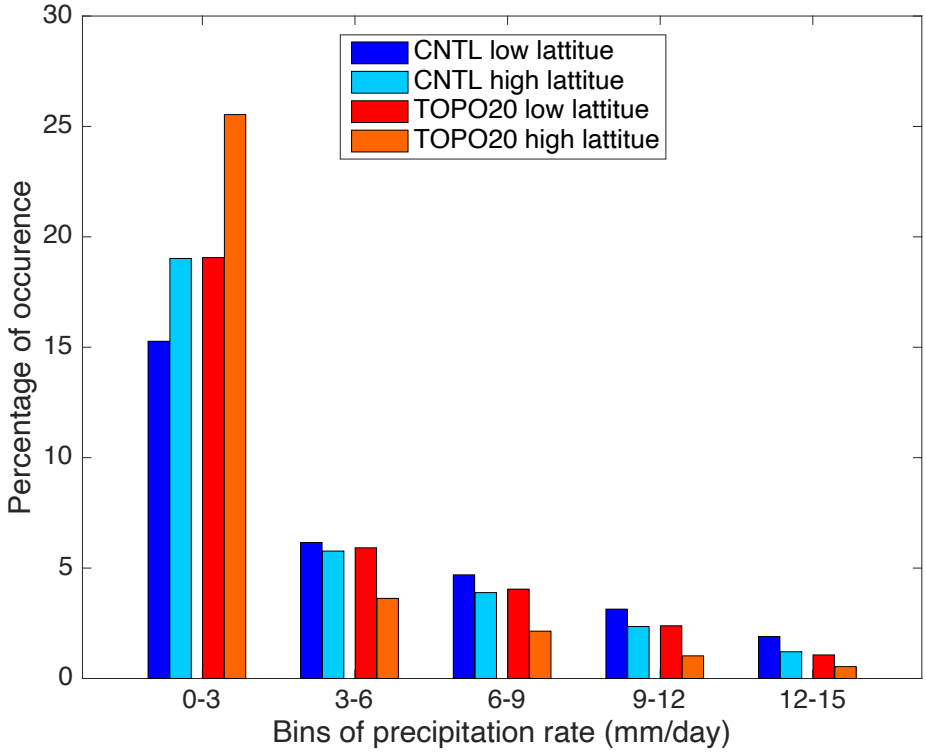

Figure 2-15 Relative occurrence of precipiation on the Tibetan Plateau

Relative occurrence (%) of summer daily precipitation rates on the Tibetan Plateau for lower latitudes (averaged over 30~32° N, 85~100° E) higher latitudes (averaged over 34~36° N, 85~100° E). Only two elevation scenarios (CNTL and TOPO20) are shown here since other scenarios are identical to these two. Low precipitation rate events are more frequent at higher latitudes than at lower latitudes under all elevation scenarios. See Figure 13 for a demonstration of how this rainfall distribution impacts $\delta^{18}O_p$.

2.4 Discussion

2.4.1 Processes impacting paleoaltimetry

The use of $\delta^{18}O_p$ as a paleoaltimeter is based on the principle that atmospheric vapor becomes saturated and condenses under forced ascent in orographic regions leading to preferential rainout of ^{18}O. Observations of meteoric $\delta^{18}O$ in orographic regions support the use of stable isotope paleoaltimetry and show a robust and significant decreasing relationship in $\delta^{18}O_p$ with surface elevation (e.g. Poage and Chamberlain, 2001; Fiorella et al., 2015; Li and Garzione, 2017) that can be modeled by Rayleigh distillation (Rowley and Garzione, 2007). However, there is no a priori reason that modern $\delta^{18}O$-elevation relationships should hold in the

past when surface elevations and associated atmospheric conditions were different (e.g. Ehlers and Poulsen, 2009; Poulsen et al., 2010; Feng et al., 2013; Botsyun et al., 2016).

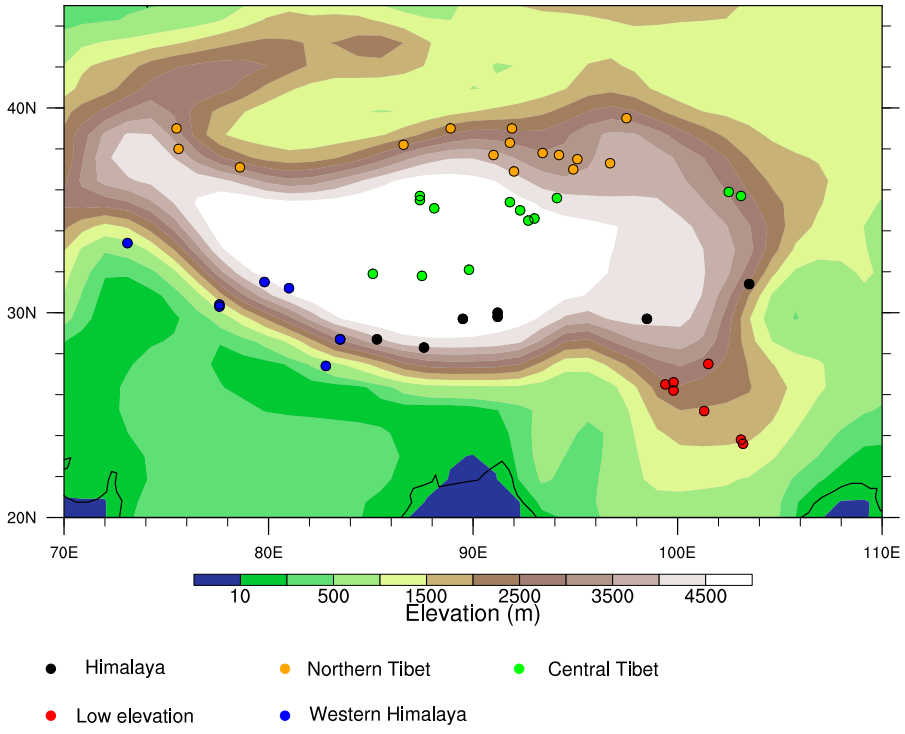

Figure 2-16 Evaluation for paleoaltimetry sites

Map of $\delta^{18}O_p$-paleoaltimetry sites (filled circles) plotted on surface elevation (shaded). Sites are classified by their type (see Section 4.2 in the paper for more details on the categories and Table S1 for a list of the sites).

Our ECHAM5 results confirm that the processes that govern $\delta^{18}O_p$ vary spatially and change in response to changes in surface elevation. Across the Himalayan front, $\delta^{18}O_p$ generally decreases with elevation, particularly in scenarios with high Himalayan elevations. However, Rayleigh distillation often does a poor job of explaining the $\delta^{18}O_p$-elevation relationship in the Himalaya-Tibetan region. There are two primary reasons. Firstly, local processes including convection and surface recycling can dominate the land-surface exchange of vapor (Fig. 2-10). These local processes are especially strong under low-elevation scenarios in monsoonal regions, where forced ascent is weak, and in the western Himalayas. Secondly, in regions with multiple moisture sources, mixing of air masses with different $\delta^{18}O$ can cause the $\delta^{18}O_p$-elevation signal to deviate from that expected from Rayleigh distillation. The transitional region on the Himalaya, which receives moisture from both the Arabian Sea and the Bay of Bengal, is such a case (Fig. A-7). On the Tibetan Plateau, the meridional $\delta^{18}O_p$ gradient decreases in response to reduced

elevation. This meridional $\delta^{18}O_p$ gradient is primarily controlled by sub-cloud re-evaporation under modern elevations. Sub-cloud re-evaporation increases due to wetter conditions in low-elevation scenarios, reducing the meridional $\delta^{18}O_p$ gradient. Our conclusions are similar to those of Feng et al. (2013) for the North American Cordillera, in which it was shown that the isotopic fractionation of precipitation was not primarily due to Rayleigh distillation.

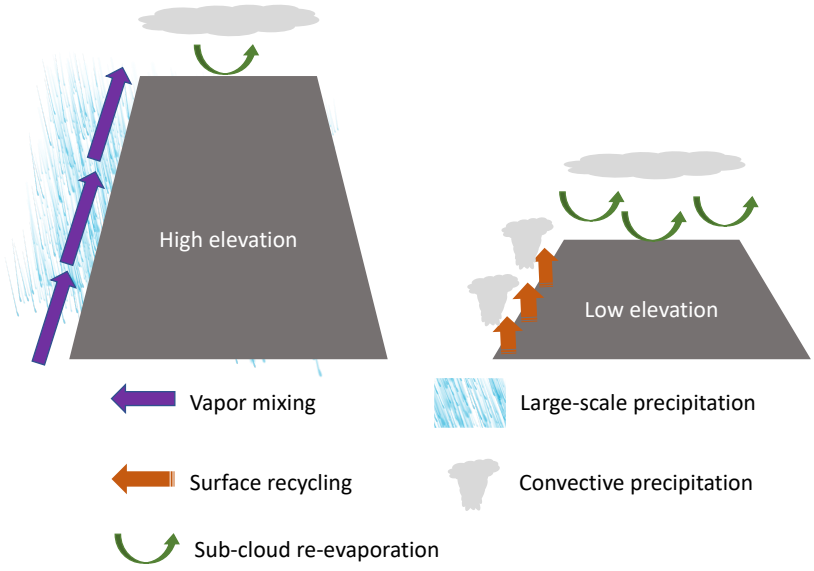

Figure 2-17 A sketch showing dominant sources/sinks

A sketch showing dominant sources/sinks of ^{18}O in the Himalayas and dominant process impacting $\delta^{18}O_p$ on the Tibetan Plateau for high and low elevation scenarios.

Our results also highlight the large influence that the choice of moisture source characteristics has on RDM $\delta^{18}O_p$ and are consistent with those of Botsyun et al. (2016). When we use fixed T and RH, ECHAM5 and RDM $\delta^{18}O_p$ agreement is poor with considerable enrichment in RDM. When we use ECHAM5 T and RH, the agreement is considerably improved. This change in moisture sources represents elevation-induced climate change unrelated to rainout and not captured by Rayleigh distillation. The overall impact from temperature and RH (red diamonds in Fig. 2-8 & 2-9) is a slight underestimation in high-elevation scenarios and severe overestimation in low-elevation scenarios (e.g. by ~100% in TOPO20 in the IM region).

2.4.2 Implications for $\delta^{18}O_p$ paleoaltimetry

As discussed above, $\delta^{18}O_p$ paleoaltimetry is only appropriate for monsoonal regions in high elevation scenarios. Nonetheless, proxy $\delta^{18}O_p$ from sites across the Himalaya-Tibet region have been used to infer paleoaltimetry throughout the Cenozoic (Fig. 2-16, Table A-1). We classify these sites into five types indicating their utility for $\delta^{18}O_p$ paleoaltimetry.

As shown in Fig. 2-16 (black dots), the modern $\delta^{18}O_p$-elevation relationship is well captured by ECHAM5 and well represented by the Rayleigh distillation process under high-elevation scenarios for 7 of 50 sites located on the high Himalayas. However, for these seven sites, the $\delta^{18}O_p$-elevation relationship breaks down as height of the Himalaya-Tibet orogen is reduced. For 13 of 50 sites in central Tibet (green dots), there is no direct $\delta^{18}O_p$-elevation relationship, since elevation is largely uniform and $\delta^{18}O_p$ increases linearly with latitude due to sub-cloud re-evaporation and recycling (as shown by 2.3.7). Although it has been proposed that $\delta^{18}O_p$-paleoaltimetry is still possible after removing this meridional $\delta^{18}O_p$ gradient from $\delta^{18}O_p$ (Bershaw et al., 2012), the meridional gradient varies by as much as 70% with elevation and is largely unknown in the past (as shown by 2.3.7); thus, $\delta^{18}O_p$-paleoaltimetry is not appropriate for these sites. For 7 of 50 sites (red dots), elevations are too low so that $\delta^{18}O_p$ has no relationship with elevation and changes very little throughout different elevation scenarios (Fig. 2-4). As a result, $\delta^{18}O_p$ is not indicative of elevation. For sites in the western and transitional regions (6 of 50), $\delta^{18}O_p$ either relates very little to elevation or exhibits a large range at the same elevation (Fig. A-6), and is thus not appropriate for $\delta^{18}O_p$-paleoaltimetry. Lastly, at sites in northern Tibet (yellow dots, 15 of 50), moisture is mostly diverted by the Tibetan Plateau, Rayleigh distillation is not triggered, and $\delta^{18}O_p$ does not vary with elevation (Fig. 2-4).

Although $\delta^{18}O_p$-elevation relationship at sites in monsoonal regions (Fig. 2-16, black dots) are well explained by Rayleigh distillation in our experiments, $\delta^{18}O_p$-paleoaltimetry should still be applied with care for these sites even under high elevation conditions due to the influence of climate change. Proxy $\delta^{18}O_p$ values as low as −18-−16 ‰ are reported for the early Eocene (Ding et al., 2014) and around −14 ‰ for the late Eocene (Rowley and Currie, 2006). These values almost certainly reflect high elevations. Nonetheless, elevation-independent factors, including atmospheric pCO_2 (Poulsen and Jeffrey, 2011) and paleogeography (Roe et al., 2016), add substantial uncertainty to the quantification of past surface elevations.

2.4.3 Caveats

Like all models, ECHAM has limitations. Most pertinent to this study, ECHAM simulates higher precipitation along the steepest slope of large mountain than indicated by satellite observations (Roe et al., 2016 and reference there in), which is a common problem in most GCMs. The model tends to overestimate the modern precipitation amount and RH on the western Tibetan plateau. This overestimation also exist in earlier version of ECHAM (Roe et al., 2016) and in LMDZ-iso (Zhang and Li, 2016). The overestimation of total-column-averaged RH might weaken sub-cloud re-evaporation process on the western plateau, and this weaker re-evaporation could potentially lower the meridional $\delta^{18}O_p$ gradient in this region. Another limitation of the model is that sub-grid scale lakes are not included. Although it has been proposed that the lakes provide $\delta^{18}O$-enriched vapor to the air (Bershaw et al., 2012), under equilibrium conditions the net $\delta^{18}O$ flux to the air should be zero. Despite these limitations, ECHAM's simulation of $\delta^{18}O_p$ compares favorably with natural water isotopic measurements (Li et al., 2016).

Another limitation of our modelling strategy is our use of a slab ocean model, which does not account for ocean circulation changes that would result from the changes in topography that we prescribe. To the best of our knowledge, no study has specifically investigated the response to a reduction in the elevations of the Himalayas and the Tibetan Plateau. It is not hard to imagine regional sea surface changes that might influence inland precipitation. For example, we speculate that under lower elevations and weaker monsoon winds, ocean upwelling along the western coast of Bay of Bengal and the Arabian Sea would be reduced, leading to higher sea-surface temperatures (SSTs). In a study of the East Asian response to historical SST warming, higher SSTs led to greater precipitation over the Indian Ocean and Pacific Ocean due to enhanced local convection and less precipitation along the Himalayan front, and further weakening of the Asian monsoon (Li et al., 2010). As this example highlights, future studies should incorporate dynamic ocean changes. An associated shortcoming is our prescription of fixed, mean-annual sea-surface $\delta^{18}O$. To quantify this impact of seasonal variations of seawater $\delta^{18}O$ on water vapor $\delta^{18}O$, we estimated the seasonal change of water vapor $\delta^{18}O$ over ocean using the Craig-Gordon model. Assuming a seasonal variation of 2.5‰ in sea water $\delta^{18}O$ (Breitenbach et al., 2010) and monthly SST, RH and air temperature from our ECHAM5 CNTL

case, we estimate that the seasonal change of water vapor $\delta^{18}O$ is within 0.3 ‰. This example illustrates the generally very small influence of seawater $\delta^{18}O$ variations on vapor and precipitation $\delta^{18}O$.

In this study, we use a series of idealized simulations to investigate the response of water isotopes to mountain uplift and to understand the mechanisms that control $\delta^{18}O_p$ variations on the Himalayas and the Tibetan Plateau. We do not compare and evaluate our model results directly against proxies, since the simulations are not meant to represent specific time slices in the geologic past. For example, the prescribed elevations with uniformly lowered Himalaya-Tibet orogen at 60% of modern height and below might not conform with the proposed Andean-type orogen and high Himalayas since the early Eocene (Wang et al., 2012). However, these scenarios can help confirm or test the proposed scenario and possible earlier elevation history before the collision of the Eurasia continents, in addition to providing insights in understanding proxy and climate responses to topography. Another reason why we do not make the comparison is that the models do not include changes in time-specific boundary conditions such as greenhouse gas composition, vegetation, orbital parameters (Tabor et al., 2018), glacial boundary conditions, tectonic displacement of the Indian subcontinent, or inclusion of the Paratethys. Changes in these boundary conditions, consistent with those that occurred through the Cenozoic, are likely to have a substantially influence on simulated $\delta^{18}O_p$. For instance, high early Cenozoic atmospheric CO_2 may have increased $\delta^{18}O_p$ over high elevation regions (Jeffery et al., 2012; Poulsen and Jeffery, 2011) and on the Tibetan Plateau by as much as 8‰ (Poulsen and Jeffery, 2011). In addition, Earth's orbital variations have been shown to contribute as much as 7 ‰ to oxygen isotope changes on the Tibetan Plateau (Battisti et al., 2014), which is comparable to the isotope difference from CNTL to TOPO20 (about −11 ‰) in Fig. 2-4. These large variations associated with orbital fluctuations are not observed in long records spanning 10^6 yrs (Deng and Ding, 2015; Kent-Corson et al., 2009), presumably because the terrestrial proxy archives of $\delta^{18}O$ integrate over orbital time periods.

2.5 Conclusion

The isotopic composition of ancient meteoric waters archived in terrestrial proxies is often used as a paleoaltimeter under the assumption that rainout during stable air parcel ascent over topography leads to a systemic isotopic depletion through Rayleigh distillation. We use an

isotope-enabled GCM, ECHAM5-wiso, to evaluate the extent to which oxygen isotopes can be used as a paleoaltimeter for the Himalaya-Tibet region and to explore the processes that control the $\delta^{18}O$-elevation relationship. Overall, our study highlights the myriad processes that influence $\delta^{18}O_p$ in the Himalaya-Tibet region now and during its uplift.

We find that Rayleigh distillation describes most of the $\delta^{18}O_p$ variation with elevation in the monsoonal regions under high-topography scenarios. In contrast, Rayleigh distillation does a poor job of describing $\delta^{18}O_p$ variation with elevation under high-topography scenarios in the western Himalayas due to the dominance of local convection and surface recycling in that region. When the Himalaya-Tibet elevations are reduced to below one-half of their modern heights, $\delta^{18}O_p$ exhibits no relationship with elevation. At these reduced elevations, $\delta^{18}O$ fractionation occurs primarily through local convection and surface recycling. On the Tibetan Plateau under modern elevations conditions, $\delta^{18}O_p$ linearly increases with latitude primarily due to sub-cloud re-evaporation. The $\delta^{18}O_p$ gradient decreases as the plateau is lowered due primarily to stronger sub-cloud re-evaporation under drier conditions and secondarily to increased moisture sources from surface recycling. Because of these elevation-independent processes, we conclude that only 7 out of the 50 paleoaltimetry sites are appropriate for $\delta^{18}O$-paleoaltimetry. Taken together, these results indicate that stable isotope paleoaltimetry in the Himalaya-Tibet region, as in other orogenic regions, is at best a blunt instrument for inferring past surface elevations.

2.6 Acknowledgements

This work was supported by National Science Foundation Grant F033233 to C. Poulsen.

2.7 References

Abe, M., Kitoh, A., and Yasunari, T., 2003, An Evolution of the Asian Summer Monsoon Associated with Mountain Uplift—Simulation with the MRI Atmosphere-Ocean Coupled GCM—: Journal of the Meteorological Society of Japan. Ser. II, v. 81, no. 5, p. 909-933.

AEA/WMO, 2017, Global Network of Isotopes in Precipitation: The GNIP Database, Accessible at: http://www.iaea.org/water.

Antonelli, A., Kissling, W. D., Flantua, S. G. A., Bermúdez, M. A., Mulch, A., Muellner-Riehl, A. N., Kreft, H., Linder, H. P., Badgley, C., Fjeldså, J., Fritz, S. A., Rahbek, C., Herman, F., Hooghiemstra, H., and Hoorn, C., 2018, Geological and climatic influences on mountain biodiversity: Nature Geoscience, v. 11, no. 10, p. 718-725.

Aron, P. G., and Poulsen, C. J., 2018, Cenozoic mountain building and climate evolution, Mountains, Climate and Biodiversity: New York, John Wiley and Sons Ltd, p. 111-121.

Battisti, D. S., Ding, Q., and Roe, G. H., 2014, Coherent pan-Asian climatic and isotopic response to orbital forcing of tropical insolation: Journal of Geophysical Research: Atmospheres, v. 119, no. 21, p. 11997-12020.

Bershaw, J., Penny, S. M., and Garzione, C. N., 2012, Stable isotopes of modern water across the Himalaya and eastern Tibetan Plateau: Implications for estimates of paleoelevation and paleoclimate: Journal of Geophysical Research-Atmospheres, v. 117, p. D02110.

Boos, W. R., 2015, A review of recent progress on Tibet's role in the South Asian monsoon: CLIVAR Exchanges Special Issue on Monsoons, v. 66, p. 23-27.

Boos, W. R., and Kuang, Z., 2010, Dominant control of the South Asian monsoon by orographic insulation versus plateau heating: Nature, v. 463, no. 7278, p. 218-222.

Botsyun, S., Sepulchre, P., Risi, C., and Donnadieu, Y., 2016, Impacts of Tibetan Plateau uplift on atmospheric dynamics and associated precipitation δ18O: Clim. Past, v. 2016, p. 1401-1420.

Breitenbach, S. F. M., Adkins, J. F., Meyer, H., Marwan, N., Kumar, K. K., and Haug, G. H., 2010, Strong influence of water vapor source dynamics on stable isotopes in precipitation observed in Southern Meghalaya, NE India: Earth and Planetary Science Letters, v. 292, no. 1, p. 212-220.

Caves Rugenstein, J. K., and Chamberlain, C. P., 2018, The evolution of hydroclimate in Asia over the Cenozoic: A stable-isotope perspective: Earth-Science Reviews, v. 185, p. 1129-1156.

Chamberlain, C. P., and Poage, M. A., 2000, Reconstructing the paleotopography of mountain belts from the isotopic composition of authigenic minerals: Geology, v. 28, no. 2, p. 115-118.

Cyr, A. J., Currie, B. S., and Rowley, D. B., 2005, Geochemical evaluation of Fenghuoshan Group lacustrine carbonates, North-Central Tibet: Implications for the paleoaltimetry of the Eocene Tibetan Plateau: Journal of Geology, v. 113, no. 5, p. 517-533.

Deng, T., and Ding, L., 2015, Paleoaltimetry reconstructions of the Tibetan Plateau: progress and contradictions: National Science Review, v. 2, no. 4, p. 417-437.

Ding, L., Xu, Q., Yue, Y., Wang, H., Cai, F., and Li, S., 2014, The Andean-type Gangdese Mountains: Paleoelevation record from the Paleocene–Eocene Linzhou Basin: Earth and Planetary Science Letters, v. 392, p. 250-264.

Ehlers, T. A., and Poulsen, C. J., 2009, Influence of Andean uplift on climate and paleoaltimetry estimates: Earth and Planetary Science Letters, v. 281, no. 3-4, p. 238-248.

Fan, M., Heller, P., Allen, S. D., and Hough, B. G., 2014, Middle Cenozoic uplift and concomitant drying in the central Rocky Mountains and adjacent Great Plains: Geology, v. 42, no. 6, p. 547-550.

Feng, R., and Poulsen, C. J., 2016, Refinement of Eocene lapse rates, fossil-leaf altimetry, and North American Cordilleran surface elevation estimates: Earth and Planetary Science Letters, v. 436, p. 130-141.

Feng, R., Poulsen, C. J., Werner, M., Chamberlain, C. P., Mix, H. T., and Mulch, A., 2013, Early Cenozoic evolution of topography, climate, and stable isotopes in precipitation in the North American Cordillera: American Journal of Science, v. 313, no. 7, p. 613-648.

Fiorella, R. P., Poulsen, C. J., Pillco Zolá, R. S., Jeffery, M. L., and Ehlers, T. A., 2015, Modern and long-term evaporation of central Andes surface waters suggests paleo archives underestimate Neogene elevations: Earth and Planetary Science Letters, v. 432, p. 59-72.

Galy, V., France-Lanord, C., Beyssac, O., Faure, P., Kudrass, H., and Palhol, F., 2007, Efficient organic carbon burial in the Bengal fan sustained by the Himalayan erosional system: Nature, v. 450, p. 407.

Garzione, C. N., Hoke, G. D., Libarkin, J. C., Withers, S., MacFadden, B., Eiler, J., Ghosh, P., and Mulch, A., 2008, Rise of the Andes: Science, v. 320, no. 5881, p. 1304-1307.

Gleckler, P., 2005, The Second Phase of the Atmospheric Model Intercomparison Project (AMIP2): Lawrence Livermore National Lab., Livermore, CA (US).

Guo, Z. T., Sun, B., Zhang, Z. S., Peng, S. Z., Xiao, G. Q., Ge, J. Y., Hao, Q. Z., Qiao, Y. S., Liang, M. Y., Liu, J. F., Yin, Q. Z., and Wei, J. J., 2008, A major reorganization of Asian climate by the early Miocene: Clim. Past, v. 4, no. 3, p. 153-174.

Haese, B., Werner, M., and Lohmann, G., 2013, Stable water isotopes in the coupled atmosphere-land surface model ECHAM5-JSBACH: Geoscientific Model Development, v. 6, p. 1463-1480.

Hoffmann, G., Werner, M., and Heimann, M., 1998, Water isotope module of the ECHAM atmospheric general circulation model: A study on timescales from days to several years: Journal of Geophysical Research: Atmospheres, v. 103, no. D14, p. 16871-16896.

Insel, N., Poulsen, C. J., and Ehlers, T. A., 2009, Influence of the Andes Mountains on South American moisture transport, convection, and precipitation: Climate Dynamics, v. 35, no. 7-8, p. 1477-1492.

Jeffery, M. L., Poulsen, C. J., and Ehlers, T. A., 2012, Impacts of Cenozoic global cooling, surface uplift, and an inland seaway on South American paleoclimate and precipitation δ18O: GSA Bulletin, v. 124, no. 3-4, p. 335-351.

Jiang, D., Ding, Z., Drange, H., and Gao, Y., 2008, Sensitivity of East Asian climate to the progressive uplift and expansion of the Tibetan Plateau under the mid-Pliocene boundary conditions: Advances in Atmospheric Sciences, v. 25, no. 5, p. 709-722.

Kent-Corson, M. L., Ritts, B. D., Zhuang, G., Bovet, P. M., Graham, S. A., and Page Chamberlain, C., 2009, Stable isotopic constraints on the tectonic, topographic, and climatic evolution of the northern margin of the Tibetan Plateau: Earth and Planetary Science Letters, v. 282, no. 1, p. 158-166.

Kitoh, A., 2004, Effects of Mountain Uplift on East Asian Summer Climate Investigated by a Coupled Atmosphere–Ocean GCM: Journal of Climate, v. 17, no. 4, p. 783-802.

Kutzbach, J. E., Guetter, P. J., Ruddiman, W. F., and Prell, W. L., 1989, Sensitivity of climate to late Cenozoic uplift in southern Asia and the American west: Numerical experiments: Journal of Geophysical Research: Atmospheres, v. 94, no. D15, p. 18393-18407.

LeGrande, A. N., and Schmidt, G. A., 2006, Global gridded data set of the oxygen isotopic composition in seawater: Geophysical Research Letters, v. 33, no. 12, p. L12604.

Li, H., Dai, A., Zhou, T., and Lu, J., 2010, Responses of East Asian summer monsoon to historical SST and atmospheric forcing during 1950–2000: Climate Dynamics, v. 34, no. 4, p. 501-514.

Li, J., Ehlers, T. A., Mutz, S. G., Steger, C., Paeth, H., Werner, M., Poulsen, C. J., and Feng, R., 2016, Modern precipitation δ18O and trajectory analysis over the Himalaya-Tibet Orogen from ECHAM5-wiso simulations: Journal of Geophysical Research: Atmospheres, v. 121, no. 18, p. 10432-10452.

Li, L., and Garzione, C., 2017, Spatial distribution and controlling factors of stable isotopes in meteoric waters on the Tibetan Plateau: implications for paleoelevation reconstruction: Earth and Planetary Science Letters, p. 302-314.

Li, S., Currie, B. S., Rowley, D. B., and Ingalls, M., 2015, Cenozoic paleoaltimetry of the SE margin of the Tibetan Plateau: Constraints on the tectonic evolution of the region: Earth and Planetary Science Letters, v. 432, p. 415-424.

Licht, A., van Cappelle, M., Abels, H. A., Ladant, J. B., Trabucho-Alexandre, J., France-Lanord, C., Donnadieu, Y., Vandenberghe, J., Rigaudier, T., Lecuyer, C., Terry Jr, D., Adriaens, R., Boura, A., Guo, Z., Soe, A. N., Quade, J., Dupont-Nivet, G., and Jaeger, J. J., 2014, Asian monsoons in a late Eocene greenhouse world: Nature, v. 513, no. 7519, p. 501-506.

Liu, X., Dong, B., Yin, Z.-Y., Smith, R. S., and Guo, Q., 2017, Continental drift and plateau uplift control origination and evolution of Asian and Australian monsoons: Scientific Reports, v. 7, p. 40344.

Maffre, P., Ladant, J.-B., Moquet, J.-S., Carretier, S., Labat, D., and Goddéris, Y., 2018, Mountain ranges, climate and weathering. Do orogens strengthen or weaken the silicate weathering carbon sink?: Earth and Planetary Science Letters, v. 493, p. 174-185.

Peters, N. A., Huntington, K. W., and Hoke, G. D., 2013, Hot or not? Impact of seasonally variable soil carbonate formation on paleotemperature and O-isotope records from clumped isotope thermometry: Earth and Planetary Science Letters, v. 361, no. Supplement C, p. 208-218.

Poage, M. A., and Chamberlain, C. P., 2001, Empirical Relationships Between Elevation and the Stable Isotope Composition of Precipitation and Surface Waters: Considerations for Studies of Paleoelevation Change: American Journal of Science, v. 301, no. 1, p. 1-15.

Poage, M. A., and Chamberlain, C. P., 2002, Stable isotopic evidence for a Pre-Middle Miocene rain shadow in the western Basin and Range: Implications for the paleotopography of the Sierra Nevada: Tectonics, v. 21, no. 4, p. 16.

Poulsen, C. J., Ehlers, T. A., and Insel, N., 2010, Onset of convective rainfall during gradual late Miocene rise of the central Andes: Science, v. 328, no. 5977, p. 490-493.

Poulsen, C. J., and Jeffery, M. L., 2011, Climate change imprinting on stable isotopic compositions of high-elevation meteoric water cloaks past surface elevations of major orogens: Geology, v. 39, no. 6, p. 595-598.

Roe, G. H., Ding, Q., Battisti, D. S., Molnar, P. H., Clark, M. K., and Garzione, C., 2016, A modeling study of the response of Asian summertime climate to the largest geologic forcings of the past 50 Ma: Journal of Geophysical Research: Atmospheres, p. 5453-5470.

Rowley, D. B., and Currie, B. S., 2006, Palaeo-altimetry of the late Eocene to Miocene Lunpola basin, central Tibet: Nature, v. 439, no. 7077, p. 677-681.

Rowley, D. B., and Garzione, C. N., 2007, Stable Isotope-Based Paleoaltimetry: Annual Review of Earth and Planetary Sciences, v. 35, no. 1, p. 463-508.

Rowley, D. B., Pierrehumbert, R. T., and Currie, B. S., 2001, A new approach to stable isotope-based paleoaltimetry: implications for paleoaltimetry and paleohypsometry of the High Himalaya since the Late Miocene: Earth and Planetary Science Letters, v. 188, no. 1-2, p. 253-268.

Royden, L. H., Burchfiel, B. C., and van der Hilst, R. D., 2008, The Geological Evolution of the Tibetan Plateau: Science, v. 321, no. 5892, p. 1054-1058.

Stewart, M. K., 1975, Stable isotope fractionation due to evaporation and isotopic exchange of falling waterdrops: Applications to atmospheric processes and evaporation of lakes: Journal of Geophysical Research, v. 80, no. 9, p. 1133-1146.

Tabor, C. R., Otto-Bliesner, B. L., Brady, E. C., Nusbaumer, J., Zhu, J., Erb, M. P., Wong, T. E., Liu, Z., and Noone, D., 2018, Interpreting Precession-Driven δ18O Variability in the South Asian Monsoon Region: Journal of Geophysical Research: Atmospheres, v. 123, no. 11, p. 5927-5946.

Wang, B., and Fan, Z., 1999, Choice of South Asian Summer Monsoon Indices: Bulletin of the American Meteorological Society, v. 80, no. 4, p. 629-638.

Yang, S., Dong, H., and Lei, F., 2009, Phylogeography of regional fauna on the Tibetan Plateau: A review: Progress in Natural Science, v. 19, no. 7, p. 789-799.

Yao, T. D., Masson-Delmotte, V., Gao, J., Yu, W. S., Yang, X. X., Risi, C., Sturm, C., Werner, M., Zhao, H. B., He, Y., Ren, W., Tian, L. D., Shi, C. M., and Hou, S. G., 2013, A review of climatic controls on δ18O in precipitation over the Tibetan Plateau: observations and simulations: Reviews of Geophysics, v. 51, no. 4, p. 525-548.

Zhang, R., Jiang, D., Zhang, Z., and Yu, E., 2015, The impact of regional uplift of the Tibetan Plateau on the Asian monsoon climate: Palaeogeography, Palaeoclimatology, Palaeoecology, v. 417, p. 137-150.

Zhang, Y., and Li, J., 2016, Impact of moisture divergence on systematic errors in precipitation around the Tibetan Plateau in a general circulation model: Climate Dynamics, p. 2923-2934.

Zhao, J., Xia, Y., Cannon, C. H., Kress, W. J., and Li, Q., 2016, Evolutionary diversification of alpine ginger reflects the early uplift of the Himalayan–Tibetan Plateau and rapid extrusion of Indochina: Gondwana Research, v. 32, p. 232-241.

Chapter 3
Impact of Central Andean Widening on Atmospheric Circulation, Orographic Precipitation, Hydrology and Paleo-elevation Estimates

Abstract

The growth of the Andes is known as a first-order control on climate over South America, and numerical simulations have been conducted to study the climate and hydrology response to a uniform uplift of the Andes. However, multiple lines of evidence suggest that the central Andes widened horizontally eastward from a narrow mountain range through the Cenozoic, and the climate response to this widening have never been investigated. In this study, we conducted simulations using a limited-domain climate model, WRF. The goal is to explore the climate response to the widening of the central Andes and its impact on local hydrology and proxy records, and to compare the response to that due to uniform surface uplift. Our results show that both widening and uplift lead to a similar increase in orographic precipitation on the eastern flank of the central Andes. In both widening and uplift scenarios, the South American Low-level Jet is substantially weakened reducing southward moisture transport. Further analysis shows that the jet is forced by the latent heating released by orographic precipitation triggered by a tall and wide central Andes. These similar responses in precipitation can substantially deplete stable water isotope and increases erosion, preserving similar signals in proxy records. Our study shows a major decrease in precipitation on the western flank of the Andes due to the widening and little change due to the uniform uplift. This differing in hydrological changes due to widening provide a scenario to be detected in proxy records. In sum, our study opens a new ground for interpreting these records and understanding the elevation history of the central Andes.

3.1 Introduction

As the longest and one of the highest continental mountain ranges in the world, the Andes serves as an important CO_2 sink through chemical weathering (Moquet et al., 2011), is a source

of erosion and sediment to terrestrial basins and continental shelves (Figueiredo et al., 2009). and enhances biodiversity through nutrient supply and the creation of ecological environments (McClain and Naiman, 2008). The Andes has also broadly affected climate on both local and regional scales. The uplift of the Andes has been linked to decrease in temperature, the formation of windward orographic precipitation and leeward aridity (Aron and Poulsen, 2018), the development of the Chaco Low, the enhancement of the South America Convergence Zone and the Bolivian High (Lenters and Cook, 1999), the reduction in El Niño events by enhancing low-cloud formation in the eastern equatorial Pacific (Feng and Poulsen, 2014), and the formation of South America Low-Level Jet (LLJ) and related orographic precipitation (Ehlers and Poulsen, 2009; Poulsen et al., 2010).

Despite decades of research, the history of Andean uplift remains uncertain. There has been considerable debate about the timing and rate of surface uplift in the central Andes, with important implications for the association of uplift with other geological and biological events and for the tectonic processes that drove uplift. The Andes was created by the Nazca plate subducting beneath the South America plate since at least the Cretaceous (Chen et al., 2019), with the central Andes divided into five tectonomorphic zones from west to east: the Precordillera, the Western Cordillera, the Andean Plateau, the Interandean Zone, and the Subandes. Much of the debate on the growth history has focused on when high elevations (>4 km) were attained on the central Andean plateau, with end-member models suggesting that the Andes reached modern heights either through punctuated rapid rise of ~2.5 km during 15–6 Ma (e.g.Garzione et al., 2006; Ghosh et al., 2006; Pingel et al., 2016; Rohrmann et al., 2016) or alternatively through long-lived steady rise since the late Eocene (Ehlers and Poulsen, 2009; Evenstar et al., 2015; Poulsen et al., 2010). Irrespective of when the Andes reached high elevations, multiple proxy records suggest that uplift of the central Andes occurred progressively from west to east. Stable water isotope records of pedogenic carbonates have been interpreted to infer a high Western Cordillera at no lower than 3 km in the late Eocene (Quade et al., 2015), and a high Altiplano Plateau no later than mid-Miocene to late Miocene (e.g. Quade et al., 2007; Saylor and Horton, 2014). Paleobotany and clumped isotope records also suggest a low Eastern Cordillera by mid-Miocene to late Miocene (Garzione et al., 2014; Graham et al., 2001). Further, Barnes and Ehlers (2009) show that the major deformation and exhumation events (based on thermochronology, sedimentary, and structural evidence) begin no later than the late Oligocene

in the western central Andes, and progressed eastward through Pliocene. To the north of the central Andes, the elevation history of the Colombian Andes is suggested to be low in mid-Miocene (Herold et al., 2008), with most of the elevation gained during Pliocene (Gregory-Wodzicki, 2000).

Given the complicated and uncertain uplift history of the Andes, studies of the climate response to Andean uplift using climate models have often assumed a uniform uplift of the entire range with a constant width. In response to uniform uplift, proxy records show a decrease in stable water isotope on the eastern flank of central Andes between 15–6 Ma and this evidence has been explained as a rapid rise in elevation and increase in precipitation (e.g. Pingel et al., 2016; Rohrmann et al., 2016). Climate models with uniform lowered topography show a threshold response with a sudden increase in orographic precipitation on the eastern Andes by increased southward moisture transport via the South American Low-Level Jet (SALLJ) as elevations are increased to 50% of modern. The threshold increase in orographic precipitation of the central Andes is shown to associate with a significant decrease in water stable isotope compositions by isotope-enable general circulation models (Insel et al., 2009; Poulsen et al., 2010). Thus, the modeled rapid decrease in isotope compositions interpret this decrease in proxy records as a threshold response during a gradual rise, rather than a rapid rise. On the western flank of the central Andes, climate modeling studies show little change or an increase in orographic precipitation with uniformly lowered topography (Ehlers and Poulsen, 2009; Fiorella et al., 2015; Poulsen et al., 2010). In contrast, proxy records show a transition from arid to hyperarid conditions in Miocene (Rech et al., 2019; Rech et al., 2006). This transition has been suggested to be either a rain shadow forced either by uplift of the Andes (Rech et al., 2019) or an increase in subsidence due to ocean cooling over the southeastern Pacific associated with global cooling (Garreaud et al., 2010). Given these climate modelling studies conducted with uniformly lowered Andes, the impacts of the widening of the central Andes on climate change has never been studied, and the further impact on the interpretation of proxy records is unknown.

Here we investigate the regional climate response to both widening and uplift of the central Andes using the state-of-the-art NCAR's Weather Research Forcasting model (WRF) (Powers et al., 2008). We focus on how progressive widening of the Andes impacts local precipitation, the South America LLJ and moisture transport. Then we further discuss the implications for hydrology and proxy records, and how this widening scenario compares with the past uniform

uplift scenario. Our work has implications for opening a new ground for interpreting the paleoaltimetry records and understanding the elevation history of the central Andes.

3.2 Model and experiments

We used a limited-domain state-of-art numerical weather prediction model (Powers et al., 2008), WRF-ARW version 3.7.1, to simulate the atmospheric response to a change to mountain elevation and shape. WRF-ARW is a three-dimensional model that has been widely used to simulate regional climate and weather conditions (e.g. Chen et al., 2014a; Martins et al., 2016). To produce precipitation that better matches observations in the South America Andes region, we adopted physics parameters from Müller et al. (2016) and incorporated diffusive damping as listed in Table. B-1. All experiments were run with 22 vertical levels and a horizontal resolution of 93.75 km (~ 1 °× 1 °), which is high in comparison to the most recent paleoclimate experiments (e.g. Díaz and Vera, 2018; Fallah et al., 2016) and necessary for simulating orographic precipitation in South America (Saurral et al., 2015). All model domains covered a large region of 100 × 100 grid cells over the South America, with a Lambert conformal projection centered at (28 °S, 70 °W) and true latitudes of 5 °S and 40 °S. Initial conditions and lateral boundary conditions were derived from the NCAR FNL reanalysis datasets (National Centers for Environmental Prediction, 2000). Large domains like the one used here have been shown to accurately perform responses to sensitivity tests with little impact from lateral boundary conditions (Insel et al., 2009; Seth and Rojas, 2003).

We conducted three main simulations only varying the mountain elevations in the Andes region. These include: (1) a control case with modern elevation (MODERN) (Fig. 3-1a), (2) a low-Andes case with 50% of modern height across all Andes region (HALF) (Fig. 3-1b), (3) a narrow-Andes case with the modern central Andes thinned to a narrow and tall mountain range along the western coast (NARROW) (Fig. 3-1c), and (4) a narrow-Andes case but with 50% of modern height (NARROW_HALF) (Fig. 3-1d). To better understand the impact of diachronous north-south uplift of the Andes, we include two additional auxiliary experiments: one in which northern Andean mountain elevations are reduced to 20% of their modern heights (LOW_NORTH) (Fig. B-1c), and a second with central Andean elevations reduced to a half of their modern height (LOW_CEN) (Fig. B-1b). Finally, we added an additional experiment with a warm tongue added to the southeast Pacific Ocean (SST) mimicking global warming prior to

Miocene (Garreaud et al., 2010). The goal of this additional experiment is to explore how the global warmth impacts precipitation on the western slope (Fig. 3-1e) in comparison to surface uplift.

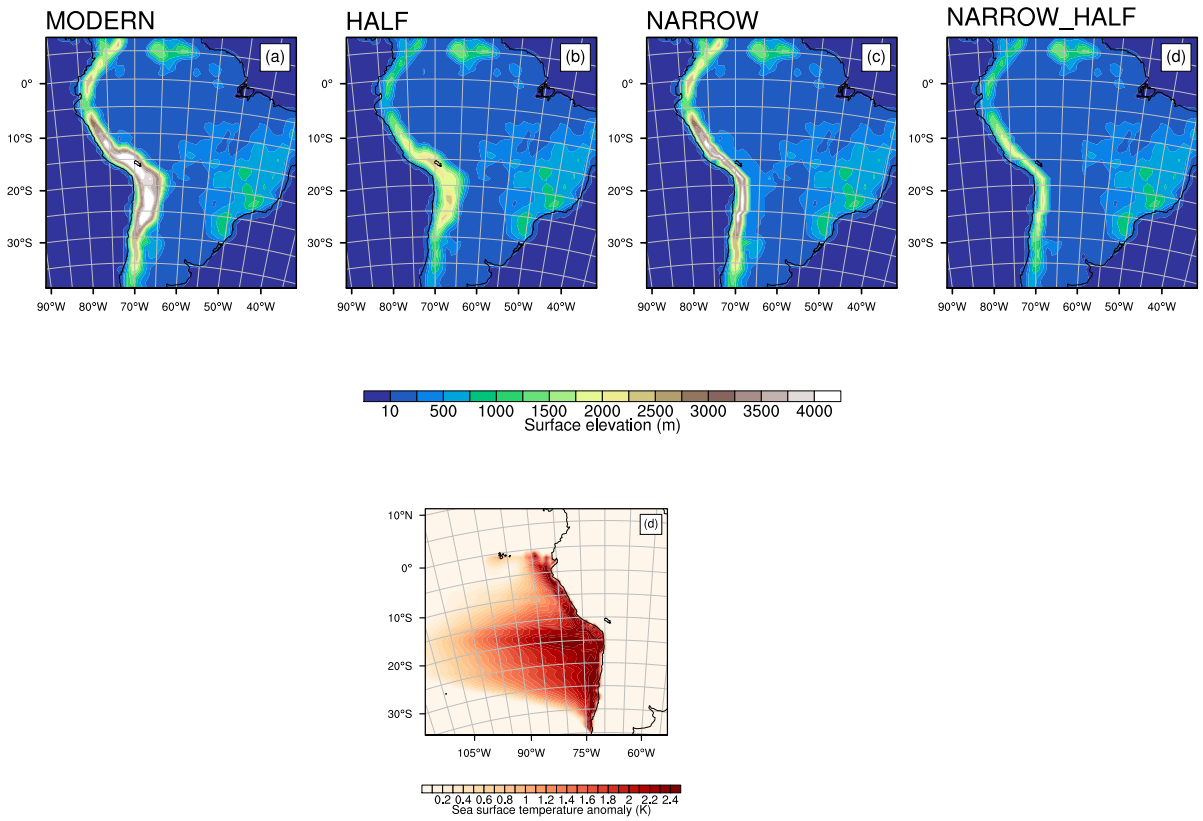

Figure 3-1 Elevation scenarios

Elevation scenario for (a) MODERN, (b) HALF, (c) NARROW, (d) NARROW_HALF, and anomalous SST for (d) SST.

3.3 Climate model results

Central Andean (~15 °S–25 °S) precipitation is highly seasonal, with 50~90% of annual precipitation falling in austral summer as simulated in MODERN (Fig. B-2). The WRF captures the distribution of precipitation similar to modern observations (Fig. 3-2 a, i), with the heavier rainfall in northern central Andes, lighter rainfall in the south, and wetter eastern flank than the western flank. The precipitation rate simulated by WRF is lighter than the observations, and this is a common problem of most model simulations (e.g. Carril et al., 2012). The response of precipitation to the uplift and the widening of the central Andes is different between northern central Andes and southern central Andes, and also between the western and eastern flanks. Thus, we analyze the orographic precipitation by regions as shown in Fig. 3-3a. North of 17 °S

on the eastern flank (NE in Fig. 3-3a), summer precipitation increases by 1–4 mm/day with uplift from HALF to MODERN, and by 7–13 mm/day with widening from HALF_NARROW to MODERN_NARROW mostly due to the eastward shift of the orographic precipitation (Fig. 3-3a). This increase due to widening from NARROW to MODERN is slighter smaller (6–9 mm/day), but still much larger than that due to simple uplift (from HALF to MODERN).

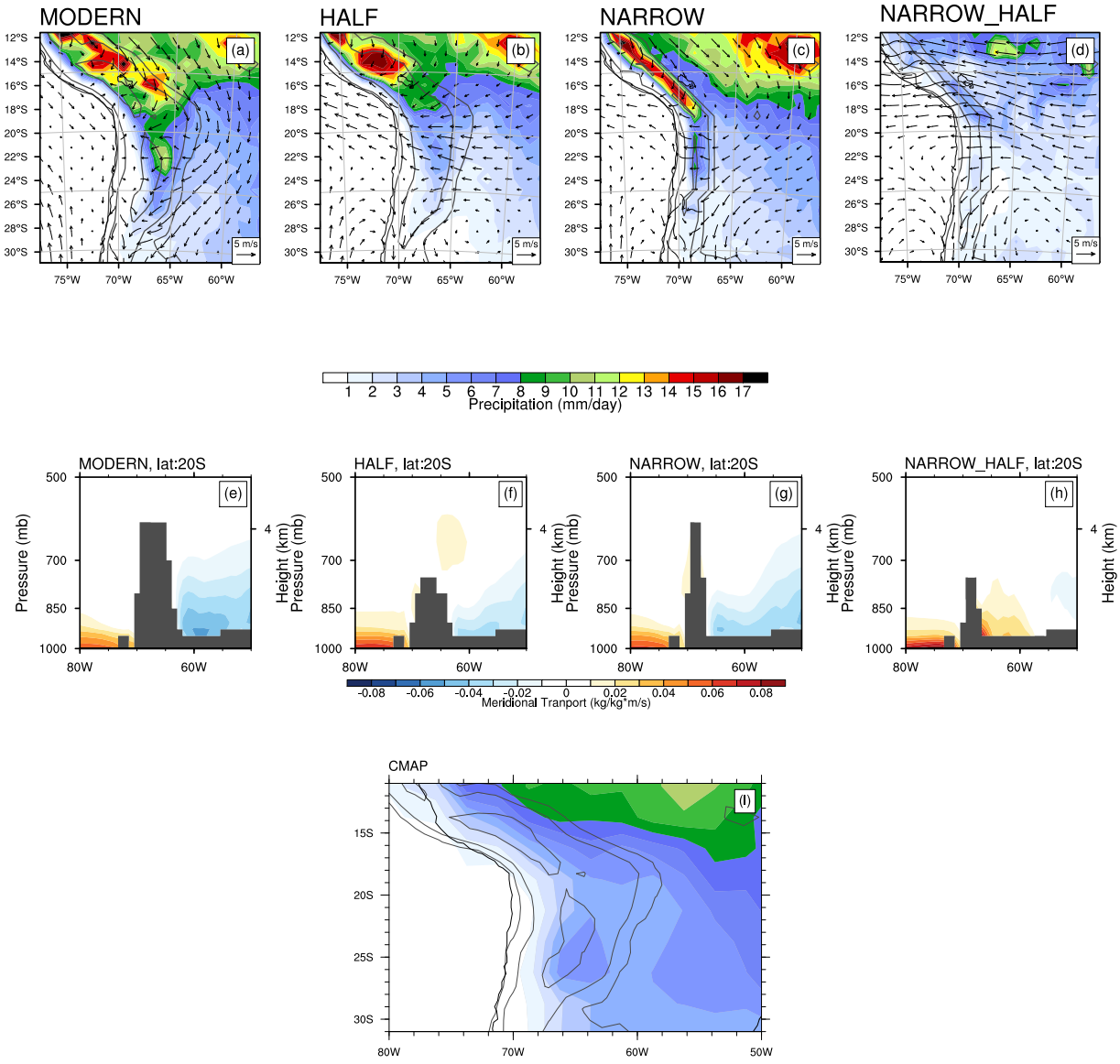

Figure 3-2 DJF winds, precipitation and zonal moisture transport

DJF winds at 800 mb (arrows) and precipitation (shaded) for elevation scenario (a) MODERN, (b) HALF, (c) NARROW, and (d) NARROW_HALF, and zonal moisture transport (shaded) for (e) MODERN, (f) HALF, (g) NARROW, and (h) NARROW_HALF. (i) Observed modern precipitation from CPC Merged Analysis of precipitation (CMAP). The modern observation shared the same colorbar as (a) to (d).

South of 18 °S (SE in Fig. 3-3a), summer precipitation increases by up to 4 mm/day (~58% of modern precipitation) on the eastern flank from HALF to MODERN and from MODERN_NARROW to MODERN, but by a much smaller amount (0.5–2 mm/day) from HALF_NARROW to NARROW (Fig. 3-3d). The large increase from NARROW to MODERN

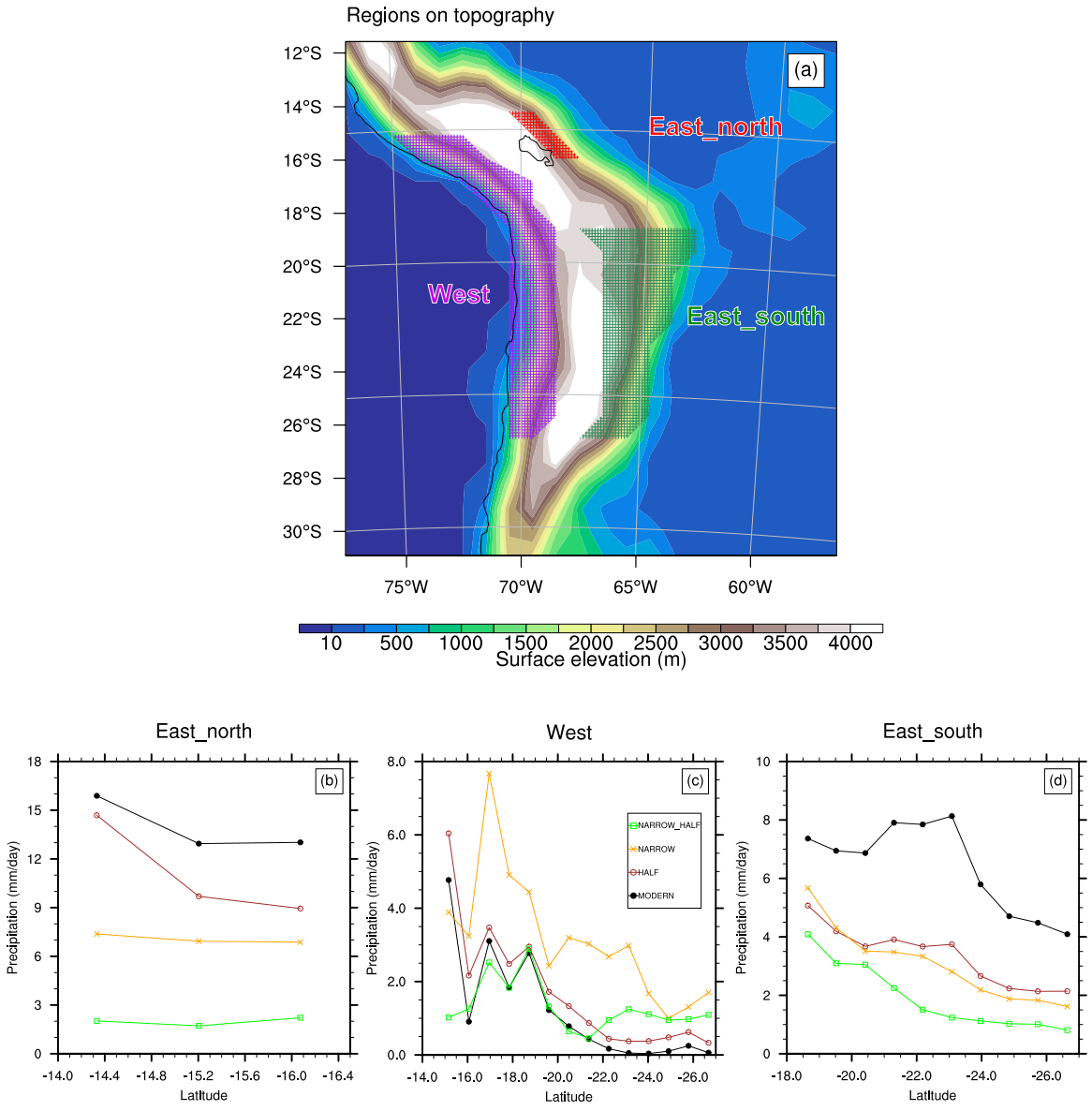

Figure 3-3 DJF precipitation by the regions

DJF precipitation by the regions as shown in (a), averaged by latitudes. Note that the y-axis scales are different among (b) to (d). Annual mean result is very similar to these results in all three regions.

is partly due to an eastward shift in orographic precipitation and partly due to a strengthening of the LLJ (Fig. 3-2a, c), which enhances via northeasterly winds southerward moisture transport

(Fig. 3-2e, g) from the Amazon Basin (AB). A similar enhancement of the LLJ and southward transport appears between HALF_NARROW to MODERN_NARROW and from HALF to MODERN (Fig. 3-2a-b, e-f). LLJ enhancement has been reported to trigger an increase in orographic precipitation as a response to a uniform uplift of the Andes from 50% to 75% of modern elevation and may explain the decrease in hydrogen and oxygen compositions in the mid-Miocene through rainout of heavy isotopologues (e.g. Insel et al., 2009; Poulsen et al., 2010).

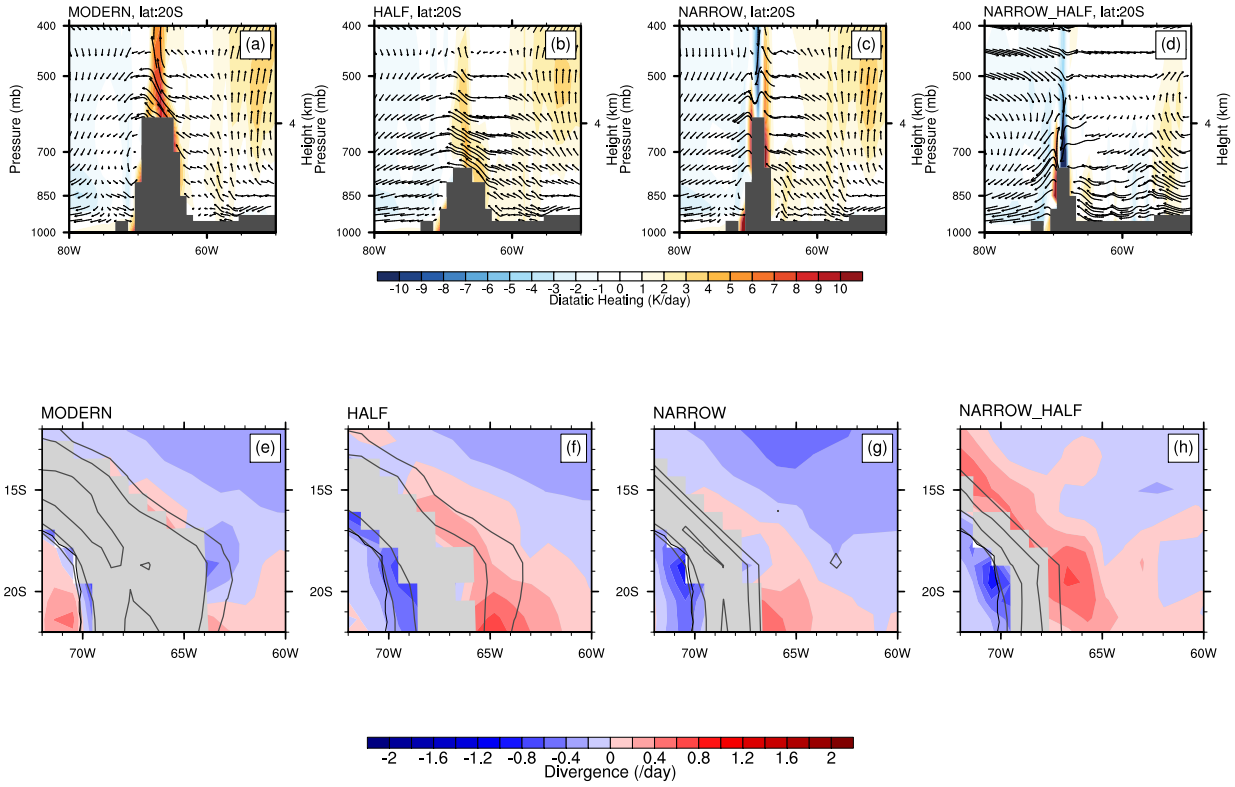

Figure 3-4 DJF diabatic heating, zonal and vertical winds, and horizontal wind convergence

DJF diabatic heating (shaded) and zonal and vertical winds (vectors) for elevation scenario (a) MODERN, (b) HALF, (c) NARROW, and (d) NARROW_HALF. And horizontal wind divergence at 800 mb for elevation scenario (e) MODERN, (f) HALF, (g) NARROW, and (h) NARROW_HALF, with positive values representing divergence and negative values denoting convergence. Note that the vertical winds are scaled to give a better view, and because of this scaling, the vector reference is not shown here. The grey shadings are topography higher than 800mb.

To explore the cause of LLJ initiation in the two experiments and to explore the climate response to other diachronous uplift scenarios of the central Andes, we conduct additional simulations in which sections of the Andes are lowered (LOW_NORTH and LOW_CEN, see Model and Experiments) (Fig.B-1). Lowering the central Andes results in weakening of the LLJ and northeasterly winds originating from the Atlantic Ocean. The weakened LLJ triggers a reduction in southward moisture transport, similar to our HALF experiment. In contrast,

lowering the northern Andes produces little changes in the LLJ and southward moisture transport. These two additional experiments, together with the MODERN, indicate that a tall and wide central Andean plateau is necessary for the LLJ to penetrate from subequatorial regions south into the subtropics.

We propose that the mechanisms that generate the LLJ are similar to those that cause the Asian Monsoon in the Himalayas (Chen et al., 2014b; Wu et al., 2012; Wu et al., 2007). The tall mountains in both MODERN and NARROW block easterly winds at low vertical levels in the subequatorial regions (Fig. 3-2a, c). However, this northwesterly winds to the east of the northern central Andes in NARROW do not penetrate further south as in MODERN (Fig 3-2a, c). This further penetration is tied to stronger convergence at lower vertical levels in MODERN and a large-scale candle-like diabatic heating of the plateau (Fig. 3-4), which is mainly due to latent heating (>80% in MODERN) released by enhanced orographic precipitation. A similar candle-like heating occurs on the Tibetan Plateau (Chen et al., 2014) and enhances the South Asian Monsoon and southerly winds. This strengthening was explained by the SHAP (sensible heat driving air pump) mechanism (Wu et al., 2007, 2012), which describes the sensible heating on highlands as an air pump, causing large-scale convergent flow at lower vertical levels and increasing local precipitation. The precipitation causes further release of latent heat and stronger air pump, forming a positive feedback.

Despite similar responses on the southeastern flank, precipitation on the western flank of central Andes (labeled as West in Fig. 3-3a) responds differently (Fig. 3-3c) to uplift and widening. Precipitation is 1–5 mm/day higher in NARROW than in all other scenarios due to the eastward shift in the location of orographic precipitation with widening. The difference in precipitation between these other scenarios is small to the south of 15 °S, less than 1 mm/day (Fig. 3-3c).

3.4 Implications for central Andean hydrology and proxies

On the western flank of the central Andes, desert paleosol records (Rech et al., 2006; Rech et al., 2019) show a transition from arid to hyperarid conditions during the Miocene, and this transition is attributed to an uplift of central Andes. Our results show that uniform uplift alone without widening (i.e. from HALF to MODERN or NARROW_HALF to NARROW) cannot account for this transition since the decrease in orographic precipitation is small (within 1

mm/day). Instead, a substantial drying of the western Andes can only be achieved by the widening of a high central Andes (from NARROW to MODERN). Among our simulations, only a widening of central Andes from NARROW to MODERN at high elevation produces a decrease by up to 9 mm/day due to the shift in orographic precipitation and the rain shadow effect due to the widening. To compare this hydrology response on the western flank to surface uplift with that to the formation of a cold tongue in the southeastern Pacific Ocean (Fig. B-2, Fig. 3-2) (Garreaud et al., 2010), we compare an experiment with specified SSTs that mimic a warm tongue, as in Garreaud et al. (2010), with MODERN. Our results show that cooling the cold tongue causes only a small decrease in DJF precipitation (within 1mm/day) (Fig. B-3).

On the eastern flank of the central Andes, a decrease in stable hydrogen/oxygen compositions of pedogenic carbonates (e.g.Pingel et al., 2016; Rohrmann et al., 2016) and an increase in paleo-surface slope incision (Barke and Lamb, 2006) have been interpreted to indicate surface uplift of the central Andes by ~2 km during the Miocene. On the southeastern flank (south of 18 °S), our results show an increase in precipitation due to widening from NARROW to MODERN and due to uplift from HALF to MODERN by ~2–5 mm/day. To show how much the increase in precipitation can potentially impact proxy records, we make an estimate using mean values of amount effect measured under modern conditions in Vimeux et al. (2005). The results show a contribution of 2.28–5.7 ‰ in $\partial^{18}O$ assuming an amount effect of -1.14 ‰ per mm/day. Assuming an isotope lapse rate of 2.39 ‰/km (Gonfiantini et al., 2001), we would estimate an elevation gain of 0.95–2.38 km due to the isotopic changes. On the northeastern flank (north of 18 °S), the increase in precipitation is ~1–4 mm/day from HALF to MODERN and 6–9 mm/day from NARROW to MODERN, which could be interpreted using stable isotope paleoaltimetry as an elevation gain of 0.5–1.9 km and 2.8–4.3 km, respectively. Similarly, rain storms are shown to be a first-order impact on eroding land surface (Tucker and Bras, 2000), and erosion-based thermochronogical records and paleo-surfaces are widely used to estimate past elevations (e.g. Barke and Lamb, 2006; Schildgen et al., 2009). The increase in precipitation can also leave imprint in these records. Overall, these estimated big increases in elevation due to the amount effect from NARROW to MODERN suggests a possible scenario of widening or partial widening of the central Andes in the Miocene.

In summary, the widening history of the central Andes can decrease stable water isotope and potentially increase erosion through increased orographic precipitation. Our results indicate that

the widening scenarios have to be considered when interpreting proxy records to reconstruct growth history.

3.5 Caveats

The goal of this study is to investigate the response of climate to a widening of the central Andes and to study the impact of this response. There are several limitations regarding the model, the experimental design and the analysis. Firstly, the horizontal resolution is 97.25 km in our simulations. This resolution is relatively low in regional modelling studies, and finer resolution may produce better match with modern observations (Saurral et al., 2015). However, it has been shown that horizontal resolution finer than 100 km can substantially decrease the bias in precipitation by giving a good representation of the mountain slopes and related atmospheric circulation (Saurral et al., 2015). Thus, the horizontal resolution (97.25 km) in our model is appropriate in simulating the orographic precipitation along the steep slopes of Andes. In addition, there is evidence from geochronological records showing increased erosion on the eastern flank of central Andes in Oligocene, indicating possible early uplift of a high and narrow (~0.25°) Eastern Cordillera (Saylor and Horton, 2014). With the current resolution, we are unable to simulate this even thinner (~0.25°) high Eastern Cordillera, and extremely high resolution of <0.05° to resolve gravity waves generated by this topography. Secondly, we showed austral summer precipitation instead of annual mean in this study. This choice of seasonal precipitation does not change our results on the eastern flank, but the precipitation differences on the western flank is dampened (see Fig. B-4). Despite of the damping, the increase in precipitation from MODERN to NARROW is still 2–7 times larger than that from MODERN to HALF from 20 °S to 24 °S. North of 20 °S, precipitation dominants in austral summer on the western flank in all experiments (Fig. B-2), and this seasonal precipitation is the most likely to be preserved in stable water isotopes. Further, more intense storms are shown to be more effective than less intense storms in eroding land surface (Tucker and Bras, 2000), thus, the dominant summer precipitation is more likely to erode the most. Thirdly, other boundary conditions not incorporated in this research, including global climate change with larger magnitude (Urrutia and Vuille, 2009), plate tectonic reorganization (e.g. Jeffery et al., 2012), the glaciation of Antarctica (Jomelli et al., 2014), and vegetation (e.g. Jeffery et al., 2014) may have impact on hydrology in

the Andes. Investigating these factors is beyond the scope of this study but is highly recommended for future research.

3.6 Conclusion

We investigate the climate response to the widening of the central Andes and discuss the impact on hydrology and paleoaltimetry by conducting numerical climate simulation by lowering the central Andes, narrowing the central Andes, and lowering while narrowing the central Andes at the same time. Our results show that the climate response varies by region. Precipitation decrease by very similar amount due to narrowing and lowering of the southeastern flank of central Andes; precipitation decrease by 2–7 mm/day more on the northeastern flank due to the thinning than due to the lowering the central Andes; precipitation changes very little on the western flank due to the lowering but increase by a large amount due to the thinning. The similar decrease in precipitation on the eastern flank due to narrowing and lowering may leave similar signals in proxy records, making the interpretation of uplift and widening possible and reasonable. The substantial increase in precipitation on the western flank due to the widening agrees better with proxy record showing a wetting from modern to Miocene. Further analysis show that the heavy precipitation under modern conditions is forced by the latent heating by central Andes, enhancing convergence and moisture transport by the LLJ. Our study emphasizes the impact of the widening central Andes on orographic precipitation by location and has implications in interpreting proxy records as a potential widening scenario in additional to uplift.

3.7 Acknowledgement

This work was supported by NSF grant EAR 1550101 to C. Poulsen.

3.8 References

Aron, P. G., and Poulsen, C. J., 2018, Cenozoic mountain building and climate evolution, Mountains, Climate and Biodiversity: New York, John Wiley and Sons Ltd, p. 111-121.

Barke, R., and Lamb, S., 2006, Late Cenozoic uplift of the Eastern Cordillera, Bolivian Andes: Earth and Planetary Science Letters, v. 249, no. 3, p. 350-367.

Barnes, J. B., and Ehlers, T. A., 2009, End member models for Andean Plateau uplift: Earth-Science Reviews, v. 97, no. 1-4, p. 105-132.

Carril, A. F., Menéndez, C. G., Remedio, A. R. C., Robledo, F., Sörensson, A., Tencer, B., Boulanger, J. P., de Castro, M., Jacob, D., Le Treut, H., Li, L. Z. X., Penalba, O., Pfeifer, S., Rusticucci, M., Salio, P., Samuelsson, P., Sanchez, E., and Zaninelli, P., 2012, Performance of a multi-RCM ensemble for South Eastern South America: Climate Dynamics, v. 39, no. 12, p. 2747-2768.

Chen, F., Yang, X., and Zhu, W., 2014a, WRF simulations of urban heat island under hot-weather synoptic conditions: The case study of Hangzhou City, China: Atmospheric Research, v. 138, p. 364-377.

Chen, G. S., Liu, Z., and Kutzbach, J. E., 2014b, Reexamining the barrier effect of the Tibetan Plateau on the South Asian summer monsoon: Clim. Past, v. 10, no. 3, p. 1269-1275.

Chen, Y.-W., Wu, J., and Suppe, J., 2019, Southward propagation of Nazca subduction along the Andes: Nature, v. 565, no. 7740, p. 441-447.

Díaz, L. B., and Vera, C. S., 2018, South American precipitation changes simulated by PMIP3/CMIP5 models during the Little Ice Age and the recent global warming period: International Journal of Climatology, v. 38, no. 6, p. 2638-2650.

Ehlers, T. A., and Poulsen, C. J., 2009, Influence of Andean uplift on climate and paleoaltimetry estimates: Earth and Planetary Science Letters, v. 281, no. 3-4, p. 238-248.

Evenstar, L. A., Stuart, F. M., Hartley, A. J., and Tattitch, B., 2015, Slow Cenozoic uplift of the western Andean Cordillera indicated by cosmogenic 3He in alluvial boulders from the Pacific Planation Surface: Geophysical Research Letters, v. 42, no. 20, p. 8448-8455.

Fallah, B., Cubasch, U., Prömmel, K., and Sodoudi, S., 2016, A numerical model study on the behaviour of Asian summer monsoon and AMOC due to orographic forcing of Tibetan Plateau: Climate Dynamics, v. 47, no. 5, p. 1485-1495.

Feng, R., and Poulsen, C. J., 2014, Andean elevation control on tropical Pacific climate and ENSO: Paleoceanography, v. 29, no. 8, p. 795-809.

Figueiredo, J., Hoorn, C., van der Ven, P., and Soares, E., 2009, Late Miocene onset of the Amazon River and the Amazon deep-sea fan: Evidence from the Foz do Amazonas Basin: Geology, v. 37, no. 7, p. 619-622.

Fiorella, R. P., Poulsen, C. J., Pillco Zolá, R. S., Jeffery, M. L., and Ehlers, T. A., 2015, Modern and long-term evaporation of central Andes surface waters suggests paleo archives underestimate Neogene elevations: Earth and Planetary Science Letters, v. 432, p. 59-72.

Garreaud, R. D., Molina, A., and Farias, M., 2010, Andean uplift, ocean cooling and Atacama hyperaridity: A climate modeling perspective: Earth and Planetary Science Letters, v. 292, no. 1, p. 39-50.

Garzione, C. N., Auerbach, D. J., Jin-Sook Smith, J., Rosario, J. J., Passey, B. H., Jordan, T. E., and Eiler, J. M., 2014, Clumped isotope evidence for diachronous surface cooling of the Altiplano and pulsed surface uplift of the Central Andes: Earth and Planetary Science Letters, v. 393, p. 173-181.

Garzione, C. N., Molnar, P., Libarkin, J. C., and MacFadden, B. J., 2006, Rapid late Miocene rise of the Bolivian Altiplano: Evidence for removal of mantle lithosphere: Earth and Planetary Science Letters, v. 241, no. 3, p. 543-556.

Ghosh, P., Garzione, C. N., and Eiler, J. M., 2006, Rapid Uplift of the Altiplano Revealed Through ¹³C-¹⁸O Bonds in Paleosol Carbonates: Science, v. 311, no. 5760, p. 511-515.

Gonfiantini, R., Roche, M.-A., Olivry, J.-C., Fontes, J.-C., and Zuppi, G. M., 2001, The altitude effect on the isotopic composition of tropical rains: Chemical Geology, v. 181, no. 1–4, p. 147-167.

Graham, A., Gregory-Wodzicki, K. M., and Wright, K. L., 2001, Studies in Neotropical Paleobotany. XV. A Mio-Pliocene palynoflora from the Eastern Cordillera, Bolivia: implications for the uplift history of the Central Andes: American Journal of Botany, v. 88, no. 9, p. 1545-1557.

Gregory-Wodzicki, K. M., 2000, Uplift history of the Central and Northern Andes: A review: GSA Bulletin, v. 112, no. 7, p. 1091-1105.

Herold, N., Seton, M., Müller, R. D., You, Y., and Huber, M., 2008, Middle Miocene tectonic boundary conditions for use in climate models: Geochemistry, Geophysics, Geosystems, v. 9, no. 10.

Hoorn, C., Wesselingh, F. P., ter Steege, H., Bermudez, M. A., Mora, A., Sevink, J., Sanmartín, I., Sanchez-Meseguer, A., Anderson, C. L., Figueiredo, J. P., Jaramillo, C., Riff, D., Negri, F. R., Hooghiemstra, H., Lundberg, J., Stadler, T., Särkinen, T., and Antonelli, A., 2010, Amazonia Through Time: Andean Uplift, Climate Change, Landscape Evolution, and Biodiversity: Science, v. 330, no. 6006, p. 927-931.

Insel, N., Poulsen, C. J., and Ehlers, T. A., 2009, Influence of the Andes Mountains on South American moisture transport, convection, and precipitation: Climate Dynamics, v. 35, no. 7-8, p. 1477-1492.

Jeffery, M. L., Poulsen, C. J., and Ehlers, T. A., 2012, Impacts of Cenozoic global cooling, surface uplift, and an inland seaway on South American paleoclimate and precipitation δ18O: GSA Bulletin, v. 124, no. 3-4, p. 335-351.

Jeffery, M. L., Yanites, B. J., Poulsen, C. J., and Ehlers, T. A., 2014, Vegetation-precipitation controls on Central Andean topography: Journal of Geophysical Research-Earth Surface, v. 119, no. 6, p. 1354-1375.

Jomelli, V., Favier, V., Vuille, M., Braucher, R., Martin, L., Blard, P. H., Colose, C., Brunstein, D., He, F., Khodri, M., Bourlès, D. L., Leanni, L., Rinterknecht, V., Grancher, D., Francou, B., Ceballos, J. L., Fonseca, H., Liu, Z., and Otto-Bliesner, B. L., 2014, A major advance of tropical Andean glaciers during the Antarctic cold reversal: Nature, v. 513, no. 7517, p. 224-228.

Lenters, J. D., and Cook, K. H., 1999, Summertime Precipitation Variability over South America: Role of the Large-Scale Circulation: Monthly Weather Review, v. 127, no. 3, p. 409-431.

Martins, J. P. A., Cardoso, R. M., Soares, P. M. M., Trigo, I. F., Belo-Pereira, M., Moreira, N., and Tomé, R., 2016, The summer diurnal cycle of coastal cloudiness over west Iberia using Meteosat/SEVIRI and a WRF regional climate model simulation: International Journal of Climatology, v. 36, no. 4, p. 1755-1772.

McClain, M. E., and Naiman, R. J., 2008, Andean Influences on the Biogeochemistry and Ecology of the Amazon River: BioScience, v. 58, no. 4, p. 325-338.

Moquet, J.-S., Crave, A., Viers, J., Seyler, P., Armijos, E., Bourrel, L., Chavarri, E., Lagane, C., Laraque, A., Casimiro, W. S. L., Pombosa, R., Noriega, L., Vera, A., and Guyot, J.-L., 2011, Chemical weathering and atmospheric/soil CO2 uptake in the Andean and Foreland Amazon basins: Chemical Geology, v. 287, no. 1, p. 1-26.

Müller, O. V., Lovino, M. A., and Berbery, E. H., 2016, Evaluation of WRF Model Forecasts and Their Use for Hydroclimate Monitoring over Southern South America: Weather and Forecasting, v. 31, no. 3, p. 1001-1017.

National Centers for Environmental Prediction, N. W. S. N. U. S. D. o. C., 2000, NCEP FNL Operational Model Global Tropospheric Analyses, continuing from July 1999: Boulder, CO, Research Data Archive at the National Center for Atmospheric Research, Computational and Information Systems Laboratory.

Pingel, H., Mulch, A., Alonso, R. N., Cottle, J., Hynek, S. A., Poletti, J., Rohrmann, A., Schmitt, A. K., Stockli, D. F., and Strecker, M. R., 2016, Surface uplift and convective rainfall along the southern Central Andes (Angastaco Basin, NW Argentina): Earth and Planetary Science Letters, v. 440, p. 33-42.

Poulsen, C. J., Ehlers, T. A., and Insel, N., 2010, Onset of convective rainfall during gradual late Miocene rise of the central Andes: Science, v. 328, no. 5977, p. 490-493.

Powers, G., Huang, X.-y., Klemp, B., Skamarock, C., Dudhia, J., Gill, O., Duda, G., Barker, D., and Wang, W., 2008, A description of the Advanced Research WRF version 3.

Quade, J., Dettinger, M. P., Carrapa, B., DeCelles, P., Murray, K. E., Huntington, K. W., Cartwright, A., Canavan, R. R., Gehrels, G., and Clementz, M., 2015, The growth of the central Andes, 22°S–26°S, *in* DeCelles, P. G., Ducea, M. N., Carrapa, B., and Kapp, P. A., eds., Geodynamics of a Cordilleran Orogenic System: The Central Andes of Argentina and Northern Chile, Geological Society of America.

Quade, J., Garzione, C., and Eiler, J., 2007, Paleoelevation reconstruction using pedogenic carbonates: Paleoaltimetry: Geochemical and Thermodynamic Approaches, v. 66, p. 53-87.

Rech, J. A., Currie, B. S., Jordan, T. E., Riquelme, R., Lehmann, S. B., Kirk-Lawlor, N. E., Li, S., and Gooley, J. T., 2019, Massive middle Miocene gypsic paleosols in the Atacama Desert and the formation of the Central Andean rain-shadow: Earth and Planetary Science Letters, v. 506, p. 184-194.

Rech, J. A., Currie, B. S., Michalski, G., and Cowan, A. M., 2006, Neogene climate change and uplift in the Atacama Desert, Chile: Geology, v. 34, no. 9, p. 761-764.

Rohrmann, A., Sachse, D., Mulch, A., Pingel, H., Tofelde, S., Alonso, R. N., and Strecker, M. R., 2016, Miocene orographic uplift forces rapid hydrological change in the southern central Andes: Scientific Reports, v. 6, p. 35678.

Saurral, R. I., Camilloni, I. A., and Ambrizzi, T., 2015, Links between topography, moisture fluxes pathways and precipitation over South America: Climate Dynamics, v. 45, no. 3, p. 777-789.

Saylor, J. E., and Horton, B. K., 2014, Nonuniform surface uplift of the Andean plateau revealed by deuterium isotopes in Miocene volcanic glass from southern Peru: Earth and Planetary Science Letters, v. 387, p. 120-131.

Schildgen, T. F., Hodges, K. V., Whipple, K. X., Pringle, M. S., van Soest, M., and Cornell, K., 2009, Late Cenozoic structural and tectonic development of the western margin of the central Andean Plateau in southwest Peru: Tectonics, v. 28, no. 4.

Seth, A., and Rojas, M., 2003, Simulation and Sensitivity in a Nested Modeling System for South America. Part I: Reanalyses Boundary Forcing: Journal of Climate, v. 16, no. 15, p. 2437-2453.

Tucker, G. E., and Bras, R. L., 2000, A stochastic approach to modeling the role of rainfall variability in drainage basin evolution: Water Resources Research, v. 36, no. 7, p. 1953-1964.

Urrutia, R., and Vuille, M., 2009, Climate change projections for the tropical Andes using a regional climate model: Temperature and precipitation simulations for the end of the 21st century: Journal of Geophysical Research: Atmospheres, v. 114, no. D2.

Vimeux, F., Gallaire, R., Bony, S., Hoffmann, G., and Chiang, J. C. H., 2005, What are the climate controls on δD in precipitation in the Zongo Valley (Bolivia)? Implications for the Illimani ice core interpretation: Earth and Planetary Science Letters, v. 240, no. 2, p. 205-220.

Wu, G., Liu, Y., He, B., Bao, Q., Duan, A., and Jin, F.-F., 2012, Thermal Controls on the Asian Summer Monsoon: Scientific Reports, v. 2, no. 1, p. 404.

Wu, G., Liu, Y., Zhang, Q., Duan, A., Wang, T., Wan, R., Liu, X., Li, W., Wang, Z., and Liang, X., 2007, The Influence of Mechanical and Thermal Forcing by the Tibetan Plateau on Asian Climate: Journal of Hydrometeorology, v. 8, no. 4, p. 770-789.

Chapter 4
A Modeling Framework (WRF-Landlab) for Simulating Orogen-scale Climate-erosion Coupling

Abstract

Precipitation-modulated erosion and orographic-forced precipitation are thought to be coupled during mountain building, potentially serving as a negative feedback on mountain uplift. However, the strength and spatial uniformity of this coupling are not well understood due to limitations in correlating past climate and orogenic events through proxy records as well as the substantial differences in temporal and spatial scales between climatic and erosional processes when using numerical models to describe these processes. Here, we present a novel numerical modeling framework that overcomes these order-of-magnitude differences in scale to study the co-evolution of climate, erosion, and mountain building. Our modeling framework uses asynchronous coupling and nested domains to link the National Center for Atmospheric Research Weather and Research Forecasting (WRF-ARW) through a hydrological model (WRF-Hydro) with Landlab, a landscape evolution model. We conduct numerical experiments that simulate coupled climate-erosion processes during uniform surface uplift from an initial flat landscape over 5 Myrs between the latitudes 0° and 40°S. Our results show that the precipitation-erosion coupling differs in strength as a function of both surface elevation and climate regime. With an increase in surface elevation and gradient, precipitation in the tropical and mid-latitude regions increases and a rain shadow forms on the leeward side of the mountain crest, while precipitation in sub-equatorial and subtropical regions exhibits little change. Erosion responds to these regional differences in precipitation and creates distinctive mean orographic elevation, slope, and hypsometry. Our study highlights that interactions between climate and erosion have a first-order impact on mountain-building over geological timescales, and that it is necessary to incorporate these interactions in modeling land surface evolution.

Keywords: climate-erosion-elevation coupling, WRF-hydro, Landlab, climate regime, precipitation-elevation relationship

4.1 Introduction

Tectonic and climatic processes are the driving forces in landscape evolution. Tectonic forces, mainly originating from interactions between tectonic plates at plate boundaries, act to uplift and deform rocks, while climate-driven processes erode and transport rock and soil materials throughout a landscape, potentially lowering mountain elevation (Anders et al., 2008; Stolar et al., 2007; Willett, 1999). It is thought that these two processes are coupled through a negative climate-erosion feedback. In this feedback, surface uplift and the creation of topography intensifies orographic precipitation leading to enhanced erosion that acts to denude the mountain (Anders et al., 2008; Insel et al., 2009; Molnar & England, 1990; Roe, 2003). Whether this climate-erosion feedback is sufficiently strong to compensate for tectonically induced surface uplift and stabilize mountain range elevations is a matter of debate (Insel et al., 2010; Montgomery and Brandon, 2002; Whipple, 2014).

The conclusions from empirical studies either have not identified clear links between precipitation and erosion rates (e.g. Blythe et al., 2007) or found inconsistent relationships at different study sites . For example, erosion rates were found to positively correlate with modern-day precipitation in the Himalayas (Grujic et al., 2006), while no such relationship was found in the central Andes (Insel et al., 2010). A shortcoming of these field studies is that they rely on mean annual precipitation rates to reach conclusions on the correlation between precipitation and erosion that may not be representative of the discrete, shorter-term events (i.e. storms) that induce erosion (Deal et al., 2018; DiBiase and Whipple, 2011; Lague et al., 2005; Tucker, 2004). Further complicating the issue, previous work often uses modern-era precipitation to make inferences about landscape evolution in the past. However, in active orogenic regions, past precipitation can differ significantly from modern due to both large-scale climate change (e.g. those due to past variations in CO_2 and orbital cycles) and as a result of surface uplift (Feng et al., 2013; Fiorella et al., 2015a; Insel et al., 2009).

In comparison to field studies that rely on modern precipitation records, numerical modeling studies are able to incorporate spatial and temporal variabilities of rainfall. Modeling studies

have shown that spatially variable orographic precipitation distribution can produce asymmetry in topography and exhumation patterns (Anders et al., 2008; Han et al., 2015; Stolar et al., 2007). Further, they have demonstrated that climate variability, which is represented as stochastic storms generated by probability functions, can lead to enhanced erosion (DiBiase and Whipple, 2011; Lague et al., 2005). Nonetheless, the representation of precipitation in past modeling studies has been greatly simplified using simple step changes in precipitation (e.g. Roe et al., 2003; Willett, 1999) or a simple linear orographic precipitation model (e.g. Anders et al., 2008; Han et al., 2015; Roe et al., 2003; Salles and Hardiman, 2016), and temporal variability has been expressed using statistical distributions with no seasonality (e.g. Tucker and Bras, 2000). These approaches have not allowed for complex responses of precipitation to elevation change, including the re-organization of large-scale precipitation due to heating or blocking of uplifted topography, the change in the relationship between orographic precipitation and topography with uplift, all of which may be important to accurately simulate the coupling between erosion and precipitation.

The challenge of incorporating these complex processes arises from differences, ranging several orders of magnitude, between the spatial and temporal scales of climatic processes and erosional processes. The response time of fluvial bedrock channels to climatic perturbations typically ranges from O(10^5 year) to O(10^6 year) (Roe, 2003). Because of this long response time, landscape models are usually integrated for millions of years with typical timesteps of hundreds or thousands of years. In order to resolve the evolution of fluvial channels, landscape models have spatial resolutions of O(10 m) to O(100 m). In contrast, atmospheric models must be run on large spatial scales of O(1km) to O(100 km) to ensure computational efficiency and over large domains of O(1000 km) to capture synoptic-scale weather systems. In addition to these large domains, atmospheric models must be run with small time steps ranging from several seconds to tens of minutes to capture medium-scale systems (e.g. gravity waves with period from minutes to hours) that are important for simulating precipitation, and also to maintain computational stability.

In this paper, we attempt to deal with these challenges by coupling NCAR's WRF-ARW, a limited-domain atmosphere-hydrology model, and WRF-Hydro, a hydrology model, with Landlab, a two-dimensional landscape evolution model. To reconcile the differences in spatial scales of climatic and erosional processes, we downscale the regional domain in WRF to a scale

that matches the resolution of Landlab. We further reconcile the difference in temporal scales by using an asynchronous coupling technique in which we run WRF-Hydro for 6 years and use the updated climate to run Landlab for millions of model years, before updating the new topography from Landlab to WRF for another run. Our coupling technique allows for feedbacks between topography and precipitation, and incorporates spatial and temporal variabilities of rainfall, which will help better understand the coevolution of topography, climate, and erosion.

4.2 WRF and Landlab description

4.2.1 Landlab

Landlab is a landscape evolution model that computes the flow of water and sediment across a gridded landscape. This python-based tool allows for a "plug-and-play" modeling environment, where users can couple a variety of process components to create a unique model. Here, we use two primary Landlab components to evolve the landscape: fluvial incision and hillslope diffusion.

The first component calculates fluvial incision using a form of the stream power law (Howard and Kerby, 1983; Whipple and Tucker, 1999). Detachment-limited local bedrock channel erosion, E [L T^{-1}], is proportional to the product of the discharge on a node per time step, Q [L^3 T^{-1}], and local channel slope, S:

$$E = KQ^m S^n, \quad (1)$$

where m and n are positive constants that are functions of incision process and channel geometry and K [$L^{-0.5}$ $T^{0.5}$] is a bedrock erodibility term (Howard, 1994; Lague, 2014; Whipple et al., 2000; Whipple & Tucker, 1999). The bedrock erodibility term encompasses variability in a wide range of parameters (lithology, climate, morphology, sediment) and determining values for K is an important area of study (Roberts & White, 2010; Stock & Montgomery, 1999; van der Beek & Bishop, 2003), but we do not explore this variability here. Instead, we choose to use a K of 5E-05 $m^{-1/2}$ $yr^{-1/2}$ to build an initial topography and a K of 0.01 $m^{-1/2}$ $yr^{-1/2}$ to run the Landlab experiments that use WRF-Hydro discharge to drive erosion (See sections 4.3.1 and 4.4 for further discussion of the Landlab model runs). As determining exact values for K is still widely

unknown, the values used here are primarily chosen to produce peaks at desired heights for the climate model simulations and fall within a reasonable range of predicted values (Stock & Montgomery, 1999). Values for *m* and *n* are held constant in all Landlab simulations (Table 4-1, C1), and are set to 0.5 and 1 respectively, following previous work (Whipple & Tucker, 1999). Discharge (Q) [L^3 $T^{-}1$] is supplied by WRF-Hydro and S represents slope.

The second Landlab component used in the model calculates hillslope diffusion, which describes the net effect of soil creep, bioturbation, and other gradual processes that modify the topography of soil-mantled hillslopes. The model follows a simple two-dimensional diffusion law such that

$$\frac{\partial z}{\partial t} = k\frac{\partial^2 z}{\partial x^2}, \quad (2)$$

where z [L] is elevation, t [T] is time, x [L] is space, and k [L^2 T^{-1}] is the diffusion coefficient. Similar to the bedrock erodibility term, values for k are difficult to measure, therefore values used in this study were chosen to produce peaks at desired heights for the climate simulations (Table 4-1).

The stream power erosion and hillslope diffusion components are implemented together to update final elevations at each node within the grid using

$$\frac{\delta z}{\delta t} = U - E + \frac{\delta z}{\delta t}, \quad (3)$$

where U [L T^{-1}] is a uniform uplift rate applied to the entire grid.

4.2.2 WRF-ARW

WRF-ARW (version 3.7.1) is a limited-domain state-of-art numerical weather prediction model (Powers et al., 2008) and has been widely used to simulate regional climate and weather conditions (e.g. Chen et al., 2014; Martins et al., 2016). WRF-ARW allows nesting of small finer-resolution domains within large lower-resolution domains.

Lower boundary conditions are obtained from various static geographical data, including satellite-based vegetation and albedo, United States Geological Survey (USGS) 24 category and satellite-based 20 category land use, and State Soil Geographic (STATSGO) soil category dataset. Initial conditions and lateral boundary conditions, including wind fields, temperature,

geopotential height, and moisture in the air, are derived from the NCAR Final (FNL) reanalysis datasets (National Centers for Environmental Prediction, 2000). The atmospheric variables are projected to the earth surface using Lambert conformal in our simulations (Miller, 1984).

The WRF-ARW physics package provides various options for parameterizing sub-grid scale processes. The combination of these options is critical in realistically simulating precipitation, heat and moisture fluxes. Land surface model (LSM) transfers these heat and moisture fluxes to the hydrological model WRF-Hydro.

4.2.3 WRF-Hydro

WRF-HYDRO (version 2.0) is a terrestrial hydrological model and is used to generate discharge maps that are input to Landlab (Gochis et al., 2013). WRF-Hydro inputs heat and moisture fluxes from WRF-ARW's LSM and downscale these fluxes by sub-grid disaggregation prior to subsurface and surface routing (including surface overland routing and channel routing). Afterwards, the hydrologic variables are upscaled by aggregating to the resolution of the LSM to be passed back to the LSM. It is recommended that the ratio of LSM and routing model grid areas do not exceed 15, in order to maintain the fidelity of the downscaled boundary conditions (Gochis et al., 2013).

Following sub-grid disaggregation, water is routed in a quasi-three-dimensional manner. This quasi-three-dimensional method first calculates hydraulic gradients based on the level of water table in each soil column. Subsurface water then flows along the direction of the steepest hydraulic gradient (i.e. the D8 method). If the soil column is supersaturated, exfiltration from the soil occurs and is the source for surface overland routing and channel routing. Surface overland routing is performed by the St. Venant equation and the continuity equation as in Julien et al. (1995), where unit discharges in Eq. (2) are given by the empirical Manning's equation. Roughness coefficients of the Manning's equation are obtained from Vieux (2001) and are mapped to modern land cover classifications. Because of the small length scale of the typical flood waves (usually less than 300 m), we use a resolution of 250 m as recommended by (Gochis et al., 2013). Channel routing is represented by a simple mass balance method and the St. Venant equation, assuming lateral inflow into channels from overland flow when surface water depth exceeds a given threshold.

4.3 Model coupling

4.3.1 Overview

Our approach to understanding the climate-topography interactions in a developing orogen is to couple the Landlab landscape evolution model with the WRF-ARW regional climate model and its hydrologic component, WRF-Hydro (Fig. 4-1), in order to simulate the idealized uplift of an incipient mountain range. To do so, an initial mountain range is created in Landlab

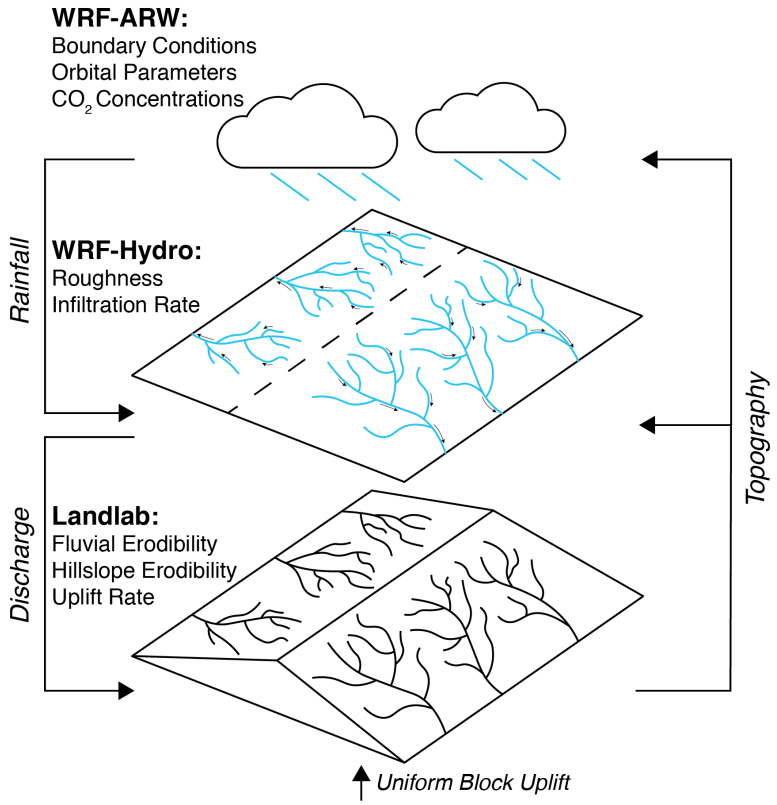

Figure 4-1 Illustration of the coupling process

Landlab topography is used as input for the climate model (WRF-ARW) and the hydrological model (WRF-Hydro). Rainfall generated in WRF-ARW is routed through the Landlab topography in WRF-Hydro to produce discharge. Discharge is input into Landlab to drive erosion. Updated topography is then sent back to WRF-ARW and WRF-Hydro for second coupling. Model names are in bold with input parameters listed below, data passed between models are in italics.

with a maximum elevation of l00 m and a channel network. This initial topography serves as the lower boundary condition for WRF-ARW and WRF-Hydro to generate high frequency (6-hourly) discharge data, which is then used by Landlab to drive erosion in the model. The

landscape in Landlab is modified through both erosion and uplift for 5 Myr, and the new topography is communicated back to WRF-ARW and WRF-Hydro for a second climate model simulation to complete the coupling.

The study domain is an idealized, north-south trending Andean mountain range along the western coast of South America spanning the tropics to mid-latitudes, allowing investigation of climate-topography coupling across different climate regimes. In sections 4.3.2-4.3.5, we describe our modeling techniques, including the domain setup, model component modifications, asynchronous coupling, and how discharge is varied temporally in Landlab and its justification.

4.3.2 Study domain setup

In choosing the model domain, the following decisions are made to balance scientific objectives against the computational cost. First, we selected the largest feasible domain in WRF-ARW. Previous work has shown that the influence of surface forcing on large-scale atmospheric circulation can be dampened in small domains (Seth and Rojas, 2003). Previous work has also shown that regional climate models (Insel et al., 2009) respond in a similar manner as global climate models (Poulsen et al., 2010) to changes in Andes elevation. To mitigate boundary effects, we use a large domain that extends from 20 °N – 60 °S and 140 °W – 0 °W. The horizontal resolution within the large domain is 93.75 km. To downscale precipitation from the large WRF-ARW domain to the fine-scale domains in WRF-Hydro and Landlab, two additional domains, with resolutions of 18.75 km and 3.75 km, are nested within the large domain in WRF-ARW (Fig. 4-2; Table 4-2). The innermost domain is of identical size and location to the domain in WRF-Hydro. Second, to smoothly transmit the outer boundary condition from WRF-Hydro domains to the fine-resolution domains in Landlab, the grid-cells in WRF-Hydro along its four boundaries are defined as a buffer zone surrounding the Landlab domain. As a result, the domain in WRF-Hydro is slightly larger (~350 x 350 km) than the domain in Landlab (~200 x 280 km) (Table 4-2). This smaller domain in Landlab is the only region where Landlab is coupled with WRF-ARW and WRF-Hydro. Third, the horizontal resolutions in both WRF-Hydro and Landlab are identically 250 m in order to resolve both the erosional processes in Landlab and the sub-surface flood waves in WRF-Hydro (Table 4-2). With such high resolution, the domain sizes in both WRF-Hydro and Landlab are limited to no more than 10^5 km^2 to keep computational costs feasible (Fig. 4-2; Table 4-2).

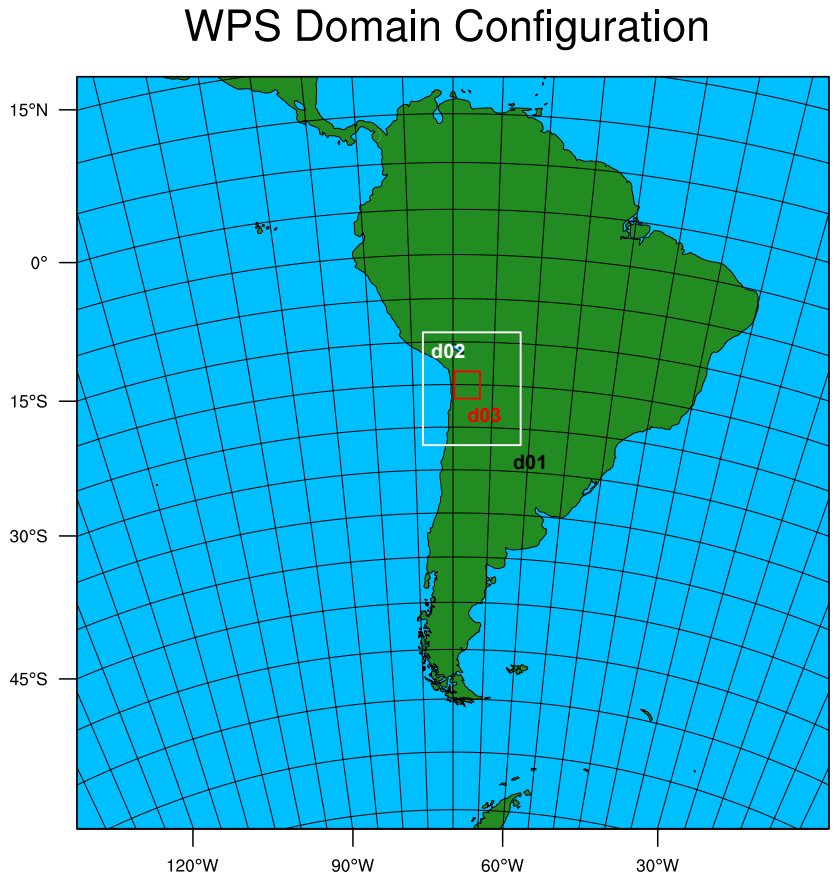

Figure 4-2 Demonstration of the three nested domains

Demonstration of the three nested domains using the third domain centered in 20°S. The three domains are shown as the three squares (black, white and red color corresponding to the outermost, intermediate and innermost domain) in this figure. d01, d02, and d03 denote the outermost, middle and innermost domain, respectively.

With these decisions in mind, we build an artificial mountain range in the present-day region of the South American Andes. Our intent is not to replicate the growth of the Andes, but to test the dynamic coupling between climate and topography. The region of the Andes is an especially useful choice because its long north-south extent makes it possible to examine the climate-erosion coupling across different climate zones. In order to build this domain, we first create five identical mountains placed between 0° and 40°S at an interval of 10° along the western coast of South America, and elevations are linearly interpolated between each domain to build a continuous mountain range (Fig. 4-3). Elevations other than this artificial mountain range are reduced to zero to avoid complicating factors of atmosphere-topography coupling that can occur when air flows around topographic obstructions (e.g. Galewsky, 2009). In creating each of the five coupled domains, we first set up a smaller domain that is 280 km long and 200 km wide

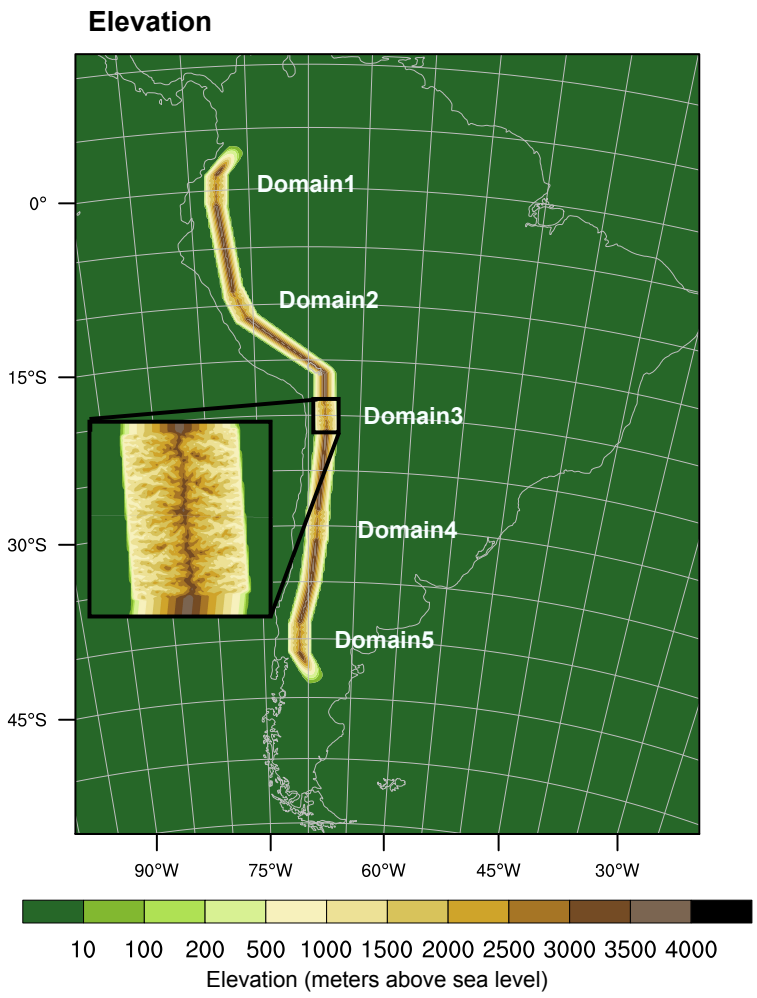

Figure 4-3 Example of initial topography

Example of initial topography input into WRF. (A) Five gridded topographies created in Landlab are placed at 10° intervals along the South American coast. (B) Elevation between each Landlab topography is interpolated to create a continuous mountain range and avoid atmospheric circulation around the base of each simulated mountain.

with a maximum elevation of 100 m (Fig. 4-3). We extend these topographies by 40-80 km (exact size depends on domains due to rotation) at each side to create a buffer zone that helps avoid instabilities that occur between the edges of the domains and the interpolated topography. The results presented in this work do not include data within this buffer zone. These gridded topographies are created using the stream power and hillslope components of Landlab with input parameters for uplift, erodibility, and diffusivity (Table 4-1) set to create steady-state mountains, defined by constant elevation at each point within the domain for over 400 kyr. The boundary conditions for these topographies include two closed boundaries and two open boundaries on opposite sides of the grid in order to create a mountain with two flanks (Fig. 4-3).

4.3.3 Model modifications

In coupling the atmosphere-hydrology model to the landscape model, the gridded discharge in WRF-Hydro must exactly align with the gridded topography in Landlab, ensuring that the discharge is correctly routed through the river networks. To make this alignment, two modifications are needed. Firstly, an ArcGIS toolbox, provided with the WRF-Hydro code, is used to interpolate the output topography from Landlab to the grids of WRF-Hydro. However, this interpolation changes the configuration of the topography, disturbing the location of the channel networks and impeding our ability to correctly align the discharge maps between WRF-Hydro and Landlab. We modify the ArcGIS toolbox code to remove the resampling process to exactly align the two models. Secondly, the projection methods are different between WRF-Hydro and Landlab. The projection of WRF-Hydro is set to be Lambert conformal with true latitudes at 5°S and 40°S for our simulations to minimize the distortions in the large area of South America; Landlab is projected on Cartesian coordinates. To make the projections consistent, we add an interface written in Matlab to perform the rotation from Lambert to Cartesian and Cartesian to Lambert.

To couple Landlab with WRF-ARW and WRF-Hydro, we make two adaptations to the Landlab code. First, the gridded elevation data from the five coupled domains used to build the initial mountain range is added to the topography in Landlab, providing an initial steady-state topography. WRF-Hydro output contains a gridded domain of discharge values and this grid is rotated and clipped using code written in Matlab, and then read into Landlab and stored at each node. Since the discharge in WRF-Hydro is routed through the topography created in Landlab, the gridded discharge data maps directly onto the gridded elevation data (Fig. 4-1).

4.3.4 Asynchronous Coupling

A difficulty that arises when coupling landscape processes with climate is the significant difference in their response time. The response time of fluvial bedrock channels to climatic perturbations typically ranges from $O(10^5$ year) to $O(10^6$ year) (Whipple, 2001). Because of this slow response, landscape models usually integrate over 100-1000 years in one time-step. In contrast, the atmosphere responds quickly to perturbations in the lower boundary condition, usually within the time range of hours to months. Because of this fast response, climate models usually integrate over short time steps of seconds to minutes, making climate models

computationally expensive to integrate over long time scales (i.e. more than a few years), and thus, impossible to integrate over the response time of landscape models.

To overcome this difficulty, we adopt an asynchronous coupling approach, in which boundary conditions are directly passed via data files between models. This approach provides reasonable climate forcing, ensures enough time for the landscape to respond, and runs in a computationally tractable manner. The workflow of this approach is shown in Fig. 4-1. The coupled model simulations iterate through the processes in Fig. 4-1 multiple times (twice in this study). Each iteration starts with passing topography produced by Landlab (with more details in 4.3.2) to the nested WRF-ARW and WRF-Hydro. Once the boundary file is read in, WRF-ARW and WRF-Hydro are run for 6 years, with the last 5 years of discharge output used as input to Landlab. The 5 years of discharge output is loaded into Landlab chronologically, with a single 6-hourly discharge dataset input at each time step in Landlab. A chronologic method was selected instead of randomly selecting discharge for each time step in order to model the effects of storm development and passage, with flood waves moving through the landscape. Once the end of the 5 years of discharge data is reached, the record is repeated as many times as necessary to complete the Landlab experiment. This single 6-hourly discharge dataset is multiplied by the time step and therefore represents the cumulative effects of many events of that size.

Forced by the discharge from WRF-Hydro, Landlab evolves over several million years. The frequency of coupling between fast (e.g. atmosphere) and slow (e.g. ocean, ice sheets, landscape) systems can affect the final coupled equilibrium state (e.g. Herrington and Poulsen, 2012), and, for this reason, the coupling frequency would ideally be as short as possible. However, the computational expense of each high-resolution WRF places practical limits on the coupling frequency. Each six-year simulation (for a single domain) costs ~80,000 core hours and takes 21 days of wall-clock time. Because of these prohibitive costs, we focus in this study on investigating the coupling behavior in domains with different climate regimes rather than attempting to simulate the long-term evolution of the Andes.

4.3.5 Validation of temporal variation of discharge in forcing Landlab

One issue that arises when forcing Landlab using the discharge from WRF-Hydro is that the discharge is output every 6 hours, much shorter than the time step of 10^2-10^3 yrs in typical Landlab runs. Ideally, Landlab would be run with the same 6-hourly time step as the WRF-

Hydro output; however, such time steps are computationally intractable since Landlab is not parallelized (Hobley et al., 2017) . Instead, 6 hourly discharge is applied to force Landlab for an entire time step of 100 yr. Tucker and Bras (2000) showed that this approach has minimal impact on resulting landscape for long-term basin evolution. To further confirm this, we conduct two experiments (Table C-1) in Landlab, varying the time step used in each experiment and analyzing the resultant topography. In the first experiment, we run five simulations in Landlab with for 50 model years and varied the time step from 0.001 (~8 hours) to 10 yrs, with the shortest time step representing the time step of the WRF-Hydro output. In the second experiment, we run four Landlab simulations for one-million model year and time steps varing from 10 to 10,000 yrs. To analyze the similarities between these simulations, we plot the change in topography during each simulation divided by the total uplift for each experiment. The results for the 50 yr and 1 Myr experiments show that despite the time step, the distribution of topography between simulations remains constant (Fig. C-1). These results show that the topography produced by Landlab is not affected by the difference in time step between WRF-Hydro and Landlab. This is because even in the experiments running for 1 Myr with a timestep of 100 yrs, each 6-hr discharge slice is selected 100 times, providing Landlab with a clear representation of the discharge distribution as it samples the full distribution many times over. Small differences arise in these final topographies due to the use of the hillslope diffusion component, which is run less often in the experiments with larger time steps. Therefore, exact elevations differ slightly between experiments, resulting in minor differences in the distribution of topography throughout the domain (Fig. C-1), but general trends in these distributions remain consistent.

4.4 Experimental Design

To show how the climate-topography co-evolution impacts atmospheric and mountain building processes, two simulations, T0 and T5, are conducted. T0 is initiated with a low, 100-meter high, artificial mountain range along the coast of South America (see Fig. 4-3 and 4.3.2). This initial topography is used as lower boundary condition in WRF-ARW and WRF-Hydro to produce the initial discharge maps. These discharge maps are then used to drive erosion in Landlab uplifting at 0.5 mm/yr for 5 Myr to produce maximum elevations of ~2.5 km. These discharge maps, precipitation produced from the initial 100 m elevation, and the resultant

topography are shown in results for T0. This ~2.5 km topography is passed to WRF-ARW and WRF-Hydro to provide precipitation and discharge maps to drive Landlab for another 5 Myrs to produce maximum elevations of ~5 km. These final discharge maps, precipitation produced from the ~2.5 km elevation and the resultant ~5 km topography are shown in results for T5.

The WRF-ARW physics parameters are shown in Table 4-3 and were demonstrated by Müller et al. (2016) to produce precipitation characteristics closely matching observations over South America. We also add in diffusive damping to reduce unrealistically heavy precipitation along steep eastern flank (5°S~15°S) (see Table 4-3 for coefficients). All WRF simulations are run for 6 years, with the last 5 years analyzed. We only show the results for domain 1, 2, 3 and 5, since the results of domain 4 are almost identical to domain 3.

4.5 Results

4.5.1 Climate response to elevation

Our simulations show that the uplift of the Andes impacts along-strike precipitation and large-scale atmospheric circulation (Fig. 4-4). Under the T0 scenario, the distribution of South American precipitation is controlled by the general circulation. The tropical region is characterized by easterly winds and high precipitation amounts to the north of 25°S; the subtropics (25°S–35°S) by large-scale subsidence and aridity; and the midlatitudes by westerly winds and moderate precipitation amounts to the south of 35°S (Fig. 4-4a, c). With the elevation increase from the T0 (100 m) to the T5 (2.5 km) scenario, there is an increase in tropical precipitation, an expansion of the subtropical high to 20°S–40°S, and a southward shift of the northern limit of the mid-latitude Westerlies to 40°S (Fig. 4-4a, b). Due to uplift, mean annual precipitation along the windward side of the mountain range (i.e. eastern slope in the tropics and subtropics, and western slope in mid-latitudes) increases by ~100% (Fig. 4-4c,d); most of this increase occurs during rainy seasons (austral winter for the midlatitudes, austral summer for the rest regions) (Fig. C-2). This increase in the magnitude of precipitation is similar to that in Insel et al. (2009) where the Andes were uplifted from 0% to 50% of modern height. Other key climate responses include an increase and northwestward shift in Amazon Basin precipitation and an increase in precipitation in the South Atlantic Convergence Zone (SACZ) (see differences

between Fig 4-5a and b), similar to previous climate modeling studies (e.g. Insel et al., 2009; Poulsen et al., 2010).

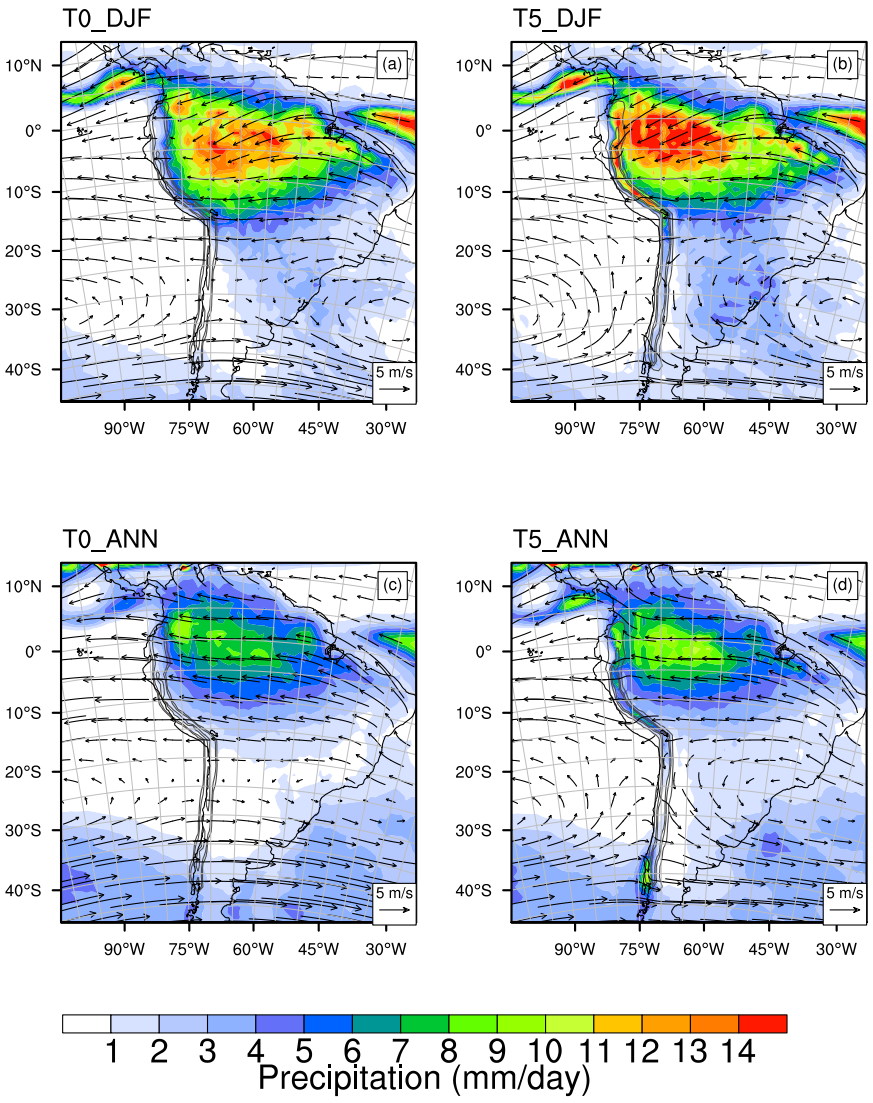

Figure 4-4 Large-scale precipitation and winds for T0 and T5

Large-scale precipitation (shaded) and 800 mb winds (arrows) (a) and (b) show austral mean summer conditions; (c) and (d) show mean annual conditions. (a) and (c) use a lower boundary condition of a mountain with maximum elevation of 100 m (T0); (b) and (d) with a mountain height from T5 simulations (~2.5 km maximum elevation). The light gray grids mark the latitudes and longitudes on a Lambert conformal projection. Black contour lines show topography gradient at 40m interval for the T0 scenario and 1000 m interval for the T5 scenario.

Insel et al. (2009) showed that the South America Low-Level Jet (LLJ) is an important moisture source in the subtropical Andes. In both the T0 and T5 scenario, the LLJ is absent (Fig. 4a-b), likely due to the narrowness of the Andes prescribed in our simulations, which induces weak surface heating in the absence of a high, broad plateau (Shen and Poulsen, in preparation).

Smaller spatial-scale precipitation features and responses are captured by the innermost high-resolution domains (Fig. 4-5 & 4-6). In the T0 scenario, mean annual precipitation varies substantially as a function of climate regime, in response to the large-scale circulation described above (Fig. 4-4). All domains exhibit relatively high precipitation amounts on the windward sides that decrease in the direction of prevailing winds, except for domain 3 which is arid and shows uniformly low precipitation (Fig. 4-5).

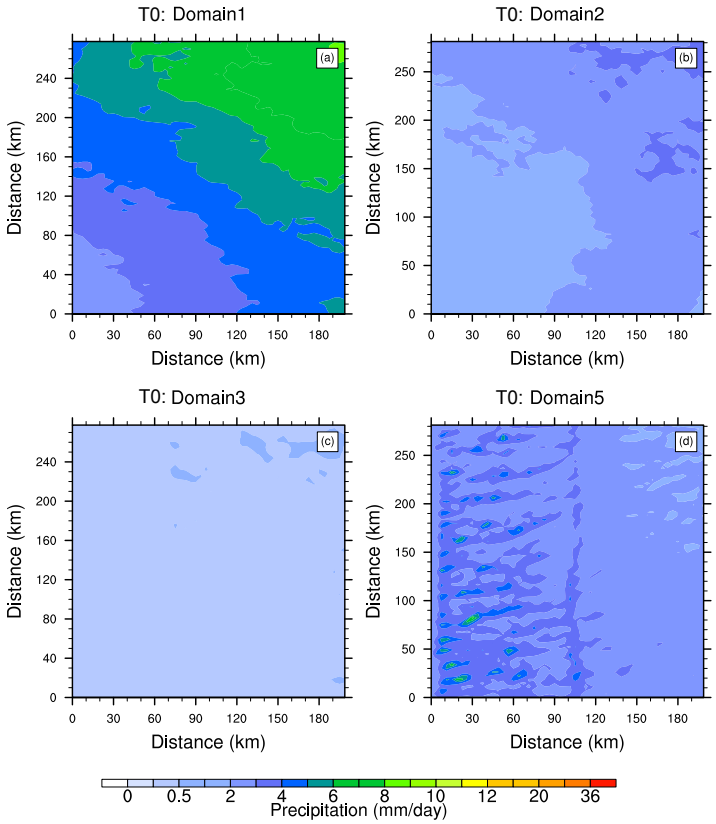

Figure 4-5 Precipitation for T0 in domain 3

Mean annual precipitation rates (shaded) from T0 initial elevation scenario as simulated by the innermost domain of WRF for (a) domain1 centered at 0° equator, (b) domain2 centered at 10° S, (c) domain3 centered at 20° S, and (d) domain5 centered at 40° S. Dashed lines denote the position for range crests.

The precipitation pattern within domains is strongly influenced by the emergent topography (Fig. 6). Both domains 1 and 5 exhibit strong orographic precipitation on the windward side of the mountain and a rain shadow on the leeward side (Fig. 4-6a, d). In domain 1, the highest precipitation rates occur on the leeward side, very close to the ridge crest in the middle of the domain (Fig. 4-6a). In contrast, in domain 5, maximum precipitation occurs at high elevations on the edge of the domain and upwind of the ridge crest (Fig. 4-6d). This difference

in the position of the maximum precipitation can be explained by more humid conditions in the tropics (relative humidity (RH) of ~90% versus 55% and mixing ratio of ~0.008 kg/kg versus ~0.002 kg/kg in domain 1 and 5, respectively, at 800 mb), which stabilizes the troposphere, resulting in less vertical motion and yielding less moisture condensation at lower elevations (Smith and Barstad, 2004). The strong rain shadow in domain 5 causes the leeward side of the mountain to be drier than in the T0 scenario (Fig. 4-5d, 4-6d). In domain 1, precipitation on the westward side of the mountain is due to moisture transport from the Pacific Ocean at low vertical levels (below 800 mb) by a land breeze that intensifies in the T5 scenario.

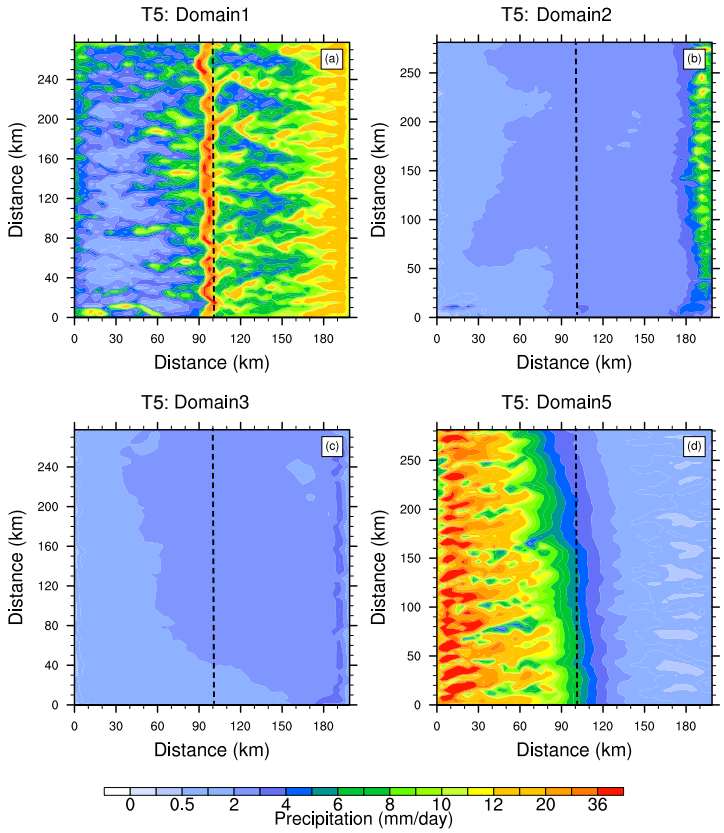

Figure 4-6 Precipitation for T5 in domain 3

Same as Fig. 6 but for T5 elevation scenario.

As in the T0 scenario, precipitation amounts in domains 2 (Fig. 4-6b) and 3 (Fig. 4-6a) remain low in the T5 scenario due to the lack of moisture transport from the LLJ in domain 2, and subtropical arid conditions in domain 3. With uplift, orographic precipitation increases on the windward side by ~8 mm/day in domain 2 and ~4 mm/day in domain 3. On the leeward side, there is only a slight increase in precipitation (< 0.5 mm/day) in domain 3, and little change in

precipitation in domain 2. This difference is related to upper level moisture transport (Roe and Baker, 2006), which is stronger in domain 2 with the uplift (Fig. C-3) due to the wetter condition to the east of domain 2 in the SACZ (Fig. 4-4a,b).

4.5.2 Erosion and discharge responses to precipitation changes

In our coupled system, climate modulates surface elevation and morphology through erosion via channel discharge. As shown in Fig. 4-7 & 4-8, discharge is controlled by the magnitude and distribution of precipitation, and the routing of excess precipitation through the drainage network. In domains 1 and 5, where precipitation penetrates to the center of the domain (Fig. 4-7b and 4-8b), discharge is large on both windward and leeward slopes (Fig. 4-7c, 4-8c), since discharge accumulates from excess precipitation flowing downhill. In domains 2 and 3 where precipitation within the domain is low, discharge is also low (Fig. 4-7b and 4-8b).

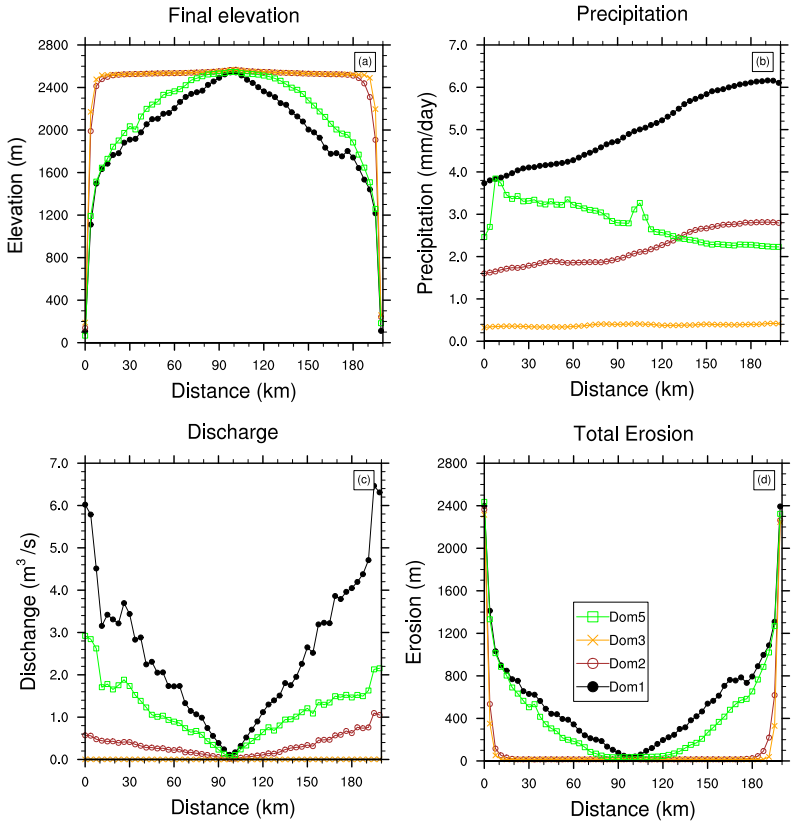

Figure 4-7 Meridional averages for final topography, precipitation, discharge and erosion for T0

Annual-mean meridional averages for (a) final topography at ~2.5 km driven by precipitation from the T0 scenario (b) T0 mean annual precipitation used to create (a), (c) discharge as generated by the precipitation in (b) under the T0 elevation scenario, and (d) total eroded elevation in T5 simulation. Only domains 1, 2, 3, 5 are shown here. Note that the scales of y-axis are different from those of Fig. 8.

In Landlab, erosion depends on discharge and slope (Eq. 1); as a result, erosion is greatest where discharge is large and slope is steep (Fig. 4-7 & 4-8, a, c, and d). Due to the erosion rule in Eq. 1, erosion is larger near the edges of the domain than near the ridges due to the establishment of a very steep topographic gradient due to the high uplift rate and overall low erosion rates, which will be further explained and discussed in 4.6.3. This high local erosion has very little impact on the mean elevation of the domain because it is constrained to a small area (~20 km in horizontal distance).

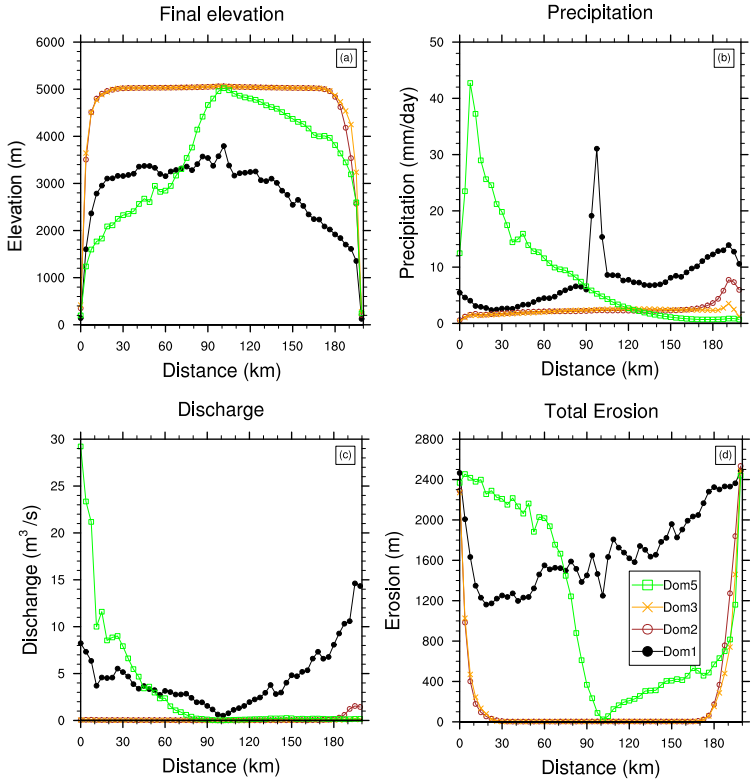

Figure 4-8 Meridional averages for final topography, precipitation, discharge and erosion for T5

Same as Fig. 8 but for T5 elevation scenario. Note that the scales of y-axis are different from those of Fig. 7.

Zonal topography, erosion, discharge and precipitation are shown as a function of latitude in Fig. 4-9 & 4-10. Generally, higher annual precipitation corresponds to higher erosion, higher discharge, smaller slopes and lower elevation, similar to the relationship shown by Montgomery et al. (2001). The exception is domain 5 where precipitation and discharge are the largest, but erosion is smaller than in domain 1 under the T5 scenario (Fig. 4-10). This exception is due to rainfall focusing at the edges of domain 5 (Fig. 4-8c), resulting in discharge trapped on the windward side and much less erosion on the leeward side.

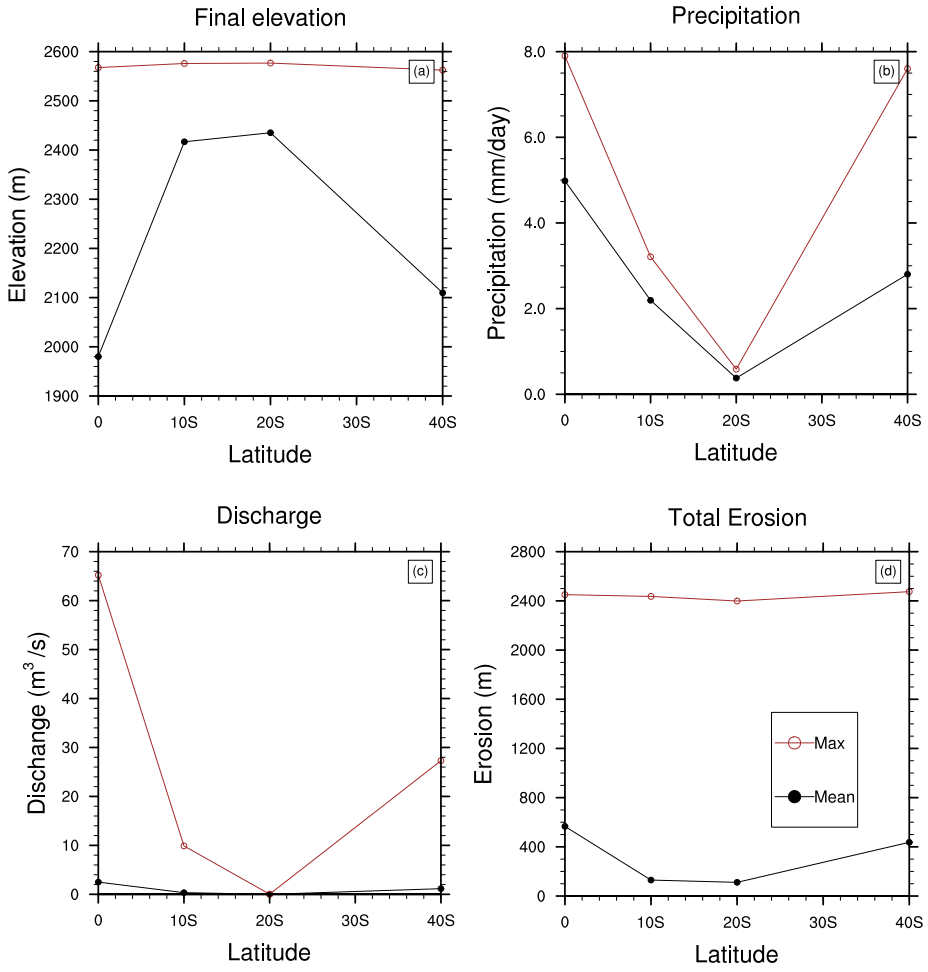

Figure 4-9 Zonal averaged max and mean for final topography, precipitation, discharge and erosion for T0

Zonal averaged max and mean for (a) final topography by T0 Landlab simulation (b) the precipitation used to create (a), generated by the T0 elevation scenario WRF simulation, (c) discharge as generated by the mean annual precipitation in (b) under the T0 elevation scenario, and (d) total eroded elevation in T5 simulation. Only domains 1, 2, 3, 5 are shown here. Note that the scales of y-axis are different from those of Fig. 10.

Precipitation and erosion also impact the variation of elevation among domains and the evolution of hypsometry. With the uplift from T0 to the T5 scenario, the final domain-averaged elevation range between domains increases from ~450 m (Fig. 4-9a) to ~2000 m (Fig. 4-10a). With this increase in the differences in mean elevation, domains 2 and 3 evolve into a more concave down, plateau-like shape than domain 1 and 5 (Fig. 4-11). This hypsometry feature in T5 is similar to that of modern Andes.

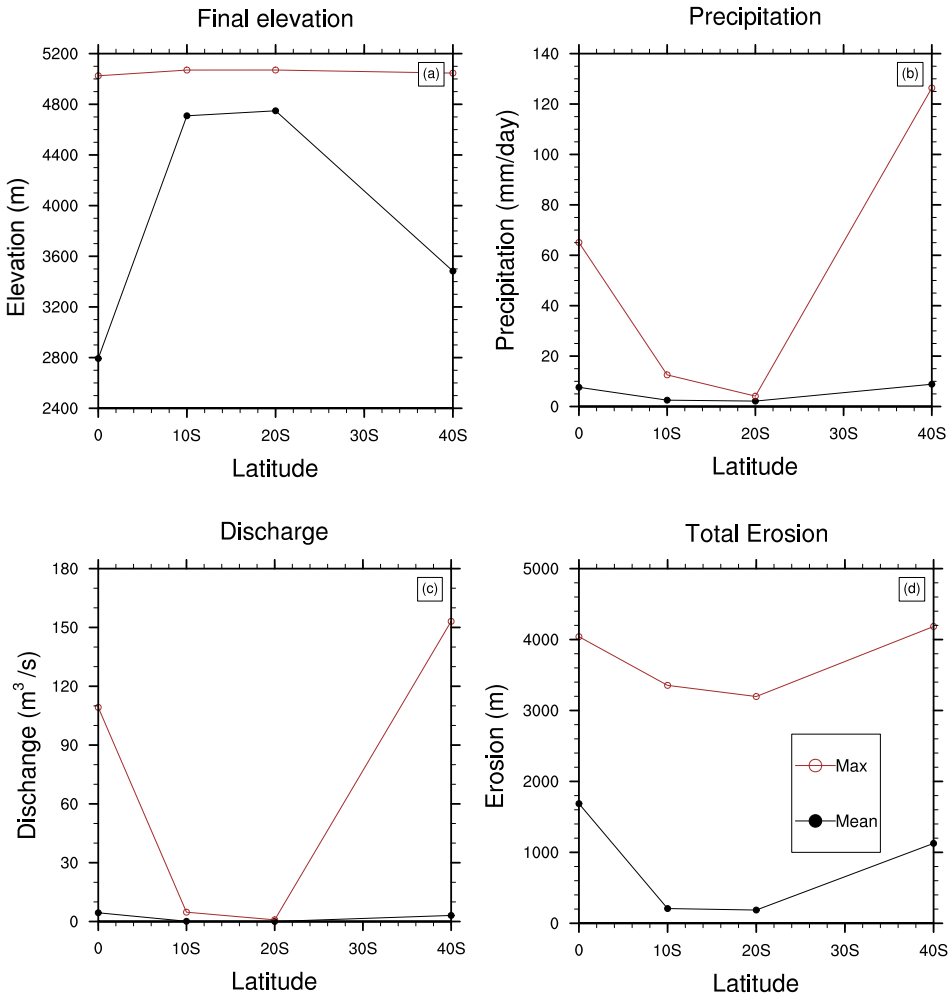

Figure 4-10 Zonal averaged max and mean for final topography, precipitation, discharge and erosion for T5

Same as Fig. 10 but for T5 elevation scenario. Note that the scales of y-axis are different from those of Fig. 9.

4.6 Discussion

4.6.1 Implications for coupling between climate, erosion, and elevation

Our simulations show a coupling between climate, erosion, and elevation; however, this coupling and its strength depends on many factors. The climate regime is a key factor impacting the distribution and strength of orographic precipitation primarily through moisture availability (e.g. domain 5 vs. domain 1) (Smith and Barstad, 2004). These impacts are passed via discharge to influence erosion and mountain elevation. Another important factor is the mountain elevation as it grows from low to high (e.g. T0 to T5). In general, this controls the strength of the climate-topography coupling. In the absence of orographic precipitation, erosion is low, and the range of

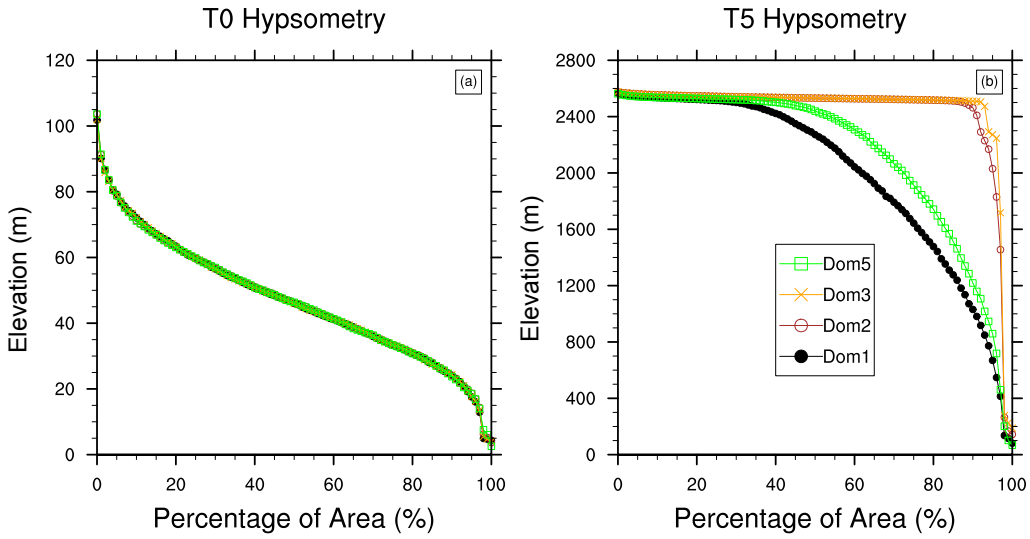

Figure 4-11 Hypsometry curves

Hypsometry curve for (a) initial topography and (b) final topography from T5 simulation. Only domains 1, 2, 3, 5 are shown here.

domain-averaged elevation between all domains is within 500 m (Fig. 4-9a). This range in domain-averaged mean elevation grows to 2000 m when topography rises (Fig. 4-10a), as orographic precipitation becomes stronger in domains 1 and 5 in the T5 elevation scenario.

Surface uplift does not cause precipitation to increase or decrease consistently across the range. On the windward side, precipitation increases with surface uplift, accompanied by increases in discharge and erosion, indicating a negative feedback of precipitation on elevation. However, with surface uplift on the leeward side, the precipitation can decrease (e.g. domain 5 due to enhanced rain shadow effects) or increase (e.g. domain 1 due to enhanced land breeze) or remain the same (e.g. domain 2).

In this study, we show how climate-driven erosion is capable of shaping topography. As shown by our simulations, when precipitation is high (e.g. domain 1 and 5), the concavity of the land surface evolves from negative to positive (Fig. 4-11). This impact of climate change on hypsometry is consistent with previous studies (e.g. Willett, 1999). In comparison, when precipitation is low (domain 2 and 3), the mountain evolves into a plateau shape with mostly high elevations due to insufficient erosion to keep pace with the high uplift rates under the fixed east-west boundary condition of the domains. In sum, we highlight the important feedbacks between climate and tectonics in highly erosive regions, and the integral role of spatially variable precipitation in shaping landscapes.

4.6.2 Application for future studies

Our study provides a modeling framework that could be applied elsewhere to understand regionally specific couplings between climate and topography, for instance, in the Himalayas where feedbacks between precipitation and erosion are highly debated (Burbank et al., 2003). Another application is to help investigate the strength of climate-erosion coupling on landscape evolution and how this strength evolves with time on geological time scale. A simulation with more frequent coupling between WRF-Hydro and Landlab would better show how the coupling changes progressively with mountain uplift and may provide more realistic output to compare to observed topography. Additionally, more simulations under different paleoclimate scenarios could help elucidate the impacts of glacial conditions, orbital parameters, and continental drift on topography-climate coupling. Lastly, the coupled model can also help better interpret the mountain-climate coevolution from reconstructed erosion rates (e.g. from paleo-surface or thermochronological records (Barke and Lamb, 2006; Starke et al., 2020)) and elevations (e.g. from stable oxygen isotopes (Fiorella et al., 2015b)).

4.6.3 Caveats

The goal of this study is to develop a framework for simulating coupled erosion-climate processes and is by its nature idealistic. There is no expectation that our modeling simulates conditions that resemble the past or modern Andes and yet they do in two important ways: the final domain-averaged topography (Fig. 4-10a) is similar to modern Andes elevations and hypsometric curves (Fig. 4-11b) show elevation distributions similar to that of the modern Andes with plateau formation at 20 °S and 30 °S. The fact that our simulations capture these features strongly suggests that erosion-climate feedbacks are primary controls on landscape evolution.

Nonetheless, our study has important limitations that stem from the models and the coupling techniques. Firstly, we use climate simulations of 5 years due to computational resources, not accounting for interannual, decadal and multi-decadal variabilities of precipitation, which may have impacts on rainstorm frequencies and erosion efficiency. Secondly, we simulate the response to time-variant rainstorms, but do not provide a simulation forced by time-invariant mean climate conditions for direct comparison. These simulations can be done in future work, and we are confident that our approach using time-variant rainstorms should have impacts on shaping landscape, since previous studies showed that erosion is sensitive to runoff variability

(Dibiase and Whipple, 2011). Thirdly, unrealistically steep slopes exist at the east-west boundaries in the T5 scenario because of the low precipitation in these domains in the low-elevation scenario and the constant uplift rates which may be too high for early-stage Andes uplift. As a result of slower erosion and faster uplift and that the topography outside of these domains is set to zero, the topography develops steep slopes at the edge of the domain. These steep boundaries create precipitation rates that are too high on the slope and hinder further penetration of moisture in dry regions and on the windward side of domain 5 (Fig. 4-7a and 4-8b). However, we do not think this shortcoming impacts the major conclusions of our study, since uplift in arid regions that lack sufficient precipitation, discharge, and fluvial erosion will produce high topography. In addition to the dry regions, in domain 5, the final elevation (Fig. 4-8a) on the windward side evolves to be much less steep in T5 comparing to T0 and will result in more realistic and lighter orographic precipitation in the next simulations. Fourthly, since there is no drainage reorganization component in the model, channels do not migrate laterally or towards divide with time, which results in no migration of the mountain ridge that would be expected with orographic precipitation. Another limitation is that, glacial erosion is not included in this study and would be an important future innovation. The omission of glacial erosion may be justifiable in the pre-Quaternary when global climate was warmer, during the early and mid-stages of uplift when the Andes were low, and at lower latitudes. Modern snowlines in the Andes are well above 4km north of 30°S (including domains 1-4), and glacial erosion is thought to be an important source for erosion only in the Southern Andes (Montgomery et al., 2001). Fourthly, erosion thresholds, which might be important for accurately modeling landscape response, are not included because we are focused on the broad relationships between mean climate and erosional of a landscape. The impact of erosion thresholds on erosion and landscape evolution, will be explored in a forthcoming paper (Lynch et al., In Preparation).

The potential impacts from human activity (Murray et al., 2013), isostasy (Simms, 2004), soil-landscape interaction (Temme and Vanwalleghem, 2016), and other boundary conditions, including global climate change (Yanites and Ehlers, 2012), global plate tectonic reorganization (Armijo et al., 2015), and vegetation (Jeffery et al., 2014), on the coupling between climate, erosion and elevation, are beyond the scope of our study but could be important to fully understanding erosion-climate coupling during orogenesis and ultimately to simulating the geological evolution of mountain ranges.

4.7 Conclusion

In this study, we present, for the first time, WRF-Landlab, a coupled climate-landscape evolution model, for investigating the interactions between climate, erosion and mountain elevation. In coupling WRF with Landlab, we reconcile the differences in spatial and temporal scale between climatic and erosional processes by using an asynchronous coupling technique and nested domains. We simulate an idealized mountain range spanning from the tropics to midlatitudes in South America, and find that strong interactions between climate, erosion and mountain elevation occur as the mountain is uplifted from 100 m to ~2.5 km:

- a shift of prevailing winds, with increased tropical precipitation, extended subtropical high, and southward shift of midlatitude Westerlies;
- an increase in precipitation by a large amount (~100%) on the windward flank;
- different patterns of precipitation at different latitudes due to the shift of general circulation, with strong rain-shadow effects in the tropics and midlatitudes, little change in sub-equatorial region and subtropics;
- a general relationship of higher annual precipitation corresponding to higher discharge, more erosion, smaller slopes and lower elevation, and exceptions on the leeward side due to erosion not keeping pace with high uplift rates;
- creation of hypsometry similar to that of modern topography, with a plateau topography in the sub-equatorial region and subtropics, and concave-up mountains in the tropics and midlatitudes.

Our results will help interpret erosion and exhumation related records, reconstruct and model past climate and mountain evolution, and inspire new studies on using coupled climate-landscape models.

4.8 Acknowledgement

This research was supported in part by Lilly Endowment, Inc., through its support for the Indiana University Pervasive Technology Institute and by NSF grant #1249788 to B. Yanites and C. Poulsen.

4.9 Computer code

We provide our modified version of this tool, the rotating scripts and a guideline for users together in GitHub with the link https://github.com/hdshen/WRF-LandLab. The source code for WRF and Landlab are available on their official websites.

4.10 References

Anders, A. M., Roe, G. H., Montgomery, D. R., and Hallet, B., 2008, Influence of precipitation phase on the form of mountain ranges: Geology, v. 36, no. 6, p. 479-482.

Armijo, R., Lacassin, R., Coudurier-Curveur, A., and Carrizo, D., 2015, Coupled tectonic evolution of Andean orogeny and global climate: Earth-Science Reviews, v. 143, p. 1-35.

Barke, R., and Lamb, S., 2006, Late Cenozoic uplift of the Eastern Cordillera, Bolivian Andes: Earth and Planetary Science Letters, v. 249, no. 3, p. 350-367.

Blythe, A. E., Burbank, D. W., Carter, A., Schmidt, K., and Putkonen, J., 2007, Plio-Quaternary exhumation history of the central Nepalese Himalaya: 1. Apatite and zircon fission track and apatite [U-Th]/He analyses: Tectonics, v. 26, no. 3, p. TC3002.

Burbank, D. W., Blythe, A. E., Putkonen, J., Pratt-Sitaula, B., Gabet, E., Oskin, M., Barros, A., and Ojha, T. P., 2003, Decoupling of erosion and precipitation in the Himalayas: Nature, v. 426, no. 6967, p. 652-655.

Chen, F., Yang, X., and Zhu, W., 2014, WRF simulations of urban heat island under hot-weather synoptic conditions: The case study of Hangzhou City, China: Atmospheric Research, v. 138, p. 364-377.

Davies, H. C., 1976, A laterul boundary formulation for multi-level prediction models: Quarterly Journal of the Royal Meteorological Society, v. 102, no. 432, p. 405-418.

Deal, E., Braun, J., and Botter, G., 2018, Understanding the Role of Rainfall and Hydrology in Determining Fluvial Erosion Efficiency: Journal of Geophysical Research: Earth Surface, v. 123, no. 4, p. 744-778.

DiBiase, R. A., and Whipple, K. X., 2011, The influence of erosion thresholds and runoff variability on the relationships among topography, climate, and erosion rate: Journal of Geophysical Research-Earth Surface, v. 116, p. F04036.

Feng, R., Poulsen, C. J., Werner, M., Chamberlain, C. P., Mix, H. T., and Mulch, A., 2013, Early Cenozoic evolution of topography, climate, and stable isotopes in precipitation in the North American Cordillera: American Journal of Science, v. 313, no. 7, p. 613-648.

Fiorella, R. P., Poulsen, C. J., Pillco Zolá, R. S., Barnes, J. B., Tabor, C. R., and Ehlers, T. A., 2015a, Spatiotemporal variability of modern precipitation δ18O in the central Andes and implications for paleoclimate and paleoaltimetry estimates: Journal of Geophysical Research: Atmospheres, v. 120, no. 10, p. 4630-4656.

Fiorella, R. P., Poulsen, C. J., Pillco Zolá, R. S., Jeffery, M. L., and Ehlers, T. A., 2015b, Modern and long-term evaporation of central Andes surface waters suggests paleo archives underestimate Neogene elevations: Earth and Planetary Science Letters, v. 432, p. 59-72.

Galewsky, J., 2009, Rain shadow development during the growth of mountain ranges: An atmospheric dynamics perspective: Journal of Geophysical Research: Earth Surface, v. 114, no. F1.

Gochis, D., Yu, W., and Yates, D., 2013, The WRF-Hydro Model Technical Description and User's Guide, Version 1.0, NCAR Technical Document: Boulder, Colo, NCAR, p. 120.

Grujic, D., Coutand, I., Bookhagen, B., Bonnet, S., Blythe, A., and Duncan, C., 2006, Climatic forcing of erosion, landscape, and tectonics in the Bhutan Himalayas: Geology, v. 34, no. 10, p. 801-804.

Han, Z., Chen, G., Li, Y., and He, Y., 2015, Assessing entrainment of bed material in a debris-flow event: a theoretical approach incorporating Monte Carlo method: Earth Surface Processes and Landforms, v. 40, no. 14, p. 1877-1890.

Herrington, A. R., Poulsen, C. J., 2012, Terminating the Last Interglacial: The Role of Ice Sheet–Climate Feedbacks in a GCM Asynchronously Coupled to an Ice Sheet Model: Journal of Climate, v. 25, no. 6, p. 1871-1882.

Hobley, D. E. J., Adams, J. M., Nudurupati, S. S., Hutton, E. W. H., Gasparini, N. M., Istanbulluoglu, E., and Tucker, G. E., 2017, Creative computing with Landlab: an open-source toolkit for building, coupling, and exploring two-dimensional numerical models of Earth-surface dynamics: Earth Surf. Dynam., v. 5, no. 1, p. 21-46.

Howard, A. D., and Kerby, G., 1983, Channel changes in badlands: Geological Society of America Bulletin, v. 94, no. 6, p. 739-752.

Insel, N., Ehlers, T. A., Schaller, M., Barnes, J. B., Tawackoli, S., and Poulsen, C. J., 2010, Spatial and temporal variability in denudation across the Bolivian Andes from multiple geochronometers: Geomorphology, v. 122, no. 1-2, p. 65-77.

Insel, N., Poulsen, C. J., and Ehlers, T. A., 2009, Influence of the Andes Mountains on South American moisture transport, convection, and precipitation: Climate Dynamics, v. 35, no. 7-8, p. 1477-1492.

Jeffery, M. L., Yanites, B. J., Poulsen, C. J., and Ehlers, T. A., 2014, Vegetation-precipitation controls on Central Andean topography: Journal of Geophysical Research-Earth Surface, v. 119, no. 6, p. 1354-1375.

Julien, P. Y., Saghafian, B., and Ogden, F. L., 1995, RASTER-BASED HYDROLOGIC MODELING OF SPATIALLY-VARIED SURFACE RUNOFF1: JAWRA Journal of the American Water Resources Association, v. 31, no. 3, p. 523-536.

Lague, D., Hovius, N., and Davy, P., 2005, Discharge, discharge variability, and the bedrock channel profile: Journal of Geophysical Research: Earth Surface, v. 110, no. F4, p. F04006.

Martins, J. P. A., Cardoso, R. M., Soares, P. M. M., Trigo, I. F., Belo-Pereira, M., Moreira, N., and Tomé, R., 2016, The summer diurnal cycle of coastal cloudiness over west Iberia using Meteosat/SEVIRI and a WRF regional climate model simulation: International Journal of Climatology, v. 36, no. 4, p. 1755-1772.

Miller, M. J., 1984, Numerical prediction and dynamic meteorology (2nd Edition). G. J. Haltiner and R. T. Williams. J. Wiley & Sons Ltd. 1983. i–xiii & pp. 477, $26.90: Quarterly Journal of the Royal Meteorological Society, v. 110, no. 463, p. 280-280.

Montgomery, D. R., Balco, G., and Willett, S. D., 2001, Climate, tectonics, and the morphology of the Andes: Geology, v. 29, no. 7, p. 579-582.

Montgomery, D. R., and Brandon, M. T., 2002, Topographic controls on erosion rates in tectonically active mountain ranges: Earth and Planetary Science Letters, v. 201, no. 3-4, p. 481-489.

Müller, O. V., Lovino, M. A., and Berbery, E. H., 2016, Evaluation of WRF Model Forecasts and Their Use for Hydroclimate Monitoring over Southern South America: Weather and Forecasting, v. 31, no. 3, p. 1001-1017.

Murray, A., Gopalakrishnan, S., McNamara, D. E., and Smith, M. D., 2013, Progress in coupling models of human and coastal landscape change: Computers & Geosciences, v. 53, p. 30-38.

National Centers for Environmental Prediction, N. W. S. N. U. S. D. o. C., 2000, NCEP FNL Operational Model Global Tropospheric Analyses, continuing from July 1999: Boulder, CO, Research Data Archive at the National Center for Atmospheric Research, Computational and Information Systems Laboratory.

Poulsen, C. J., Ehlers, T. A., and Insel, N., 2010, Onset of convective rainfall during gradual late Miocene rise of the central Andes: Science, v. 328, no. 5977, p. 490-493.

Powers, G., Huang, X.-y., Klemp, B., Skamarock, C., Dudhia, J., Gill, O., Duda, G., Barker, D., and Wang, W., 2008, A description of the Advanced Research WRF version 3.

Roberts, G.G., White, N., 2010, Estimating uplift rate histories from river profiles using African examples:Journal of Geophysical Research, v. 115, p. B02406.

Roe, G. H., and Baker, M. B., 2006, Microphysical and Geometrical Controls on the Pattern of Orographic Precipitation: Journal of the Atmospheric Sciences, v. 63, no. 3, p. 861-880.

Roe, G. H., Montgomery, D. R., and Hallet, B., 2003, Orographic precipitation and the relief of mountain ranges: Journal of Geophysical Research-Solid Earth, v. 108, no. B6, p. 2315.

Salles, T., and Hardiman, L., 2016, Badlands: An open-source, flexible and parallel framework to study landscape dynamics: Computers & Geosciences, v. 91, p. 77-89.

Seth, A., and Rojas, M., 2003, Simulation and Sensitivity in a Nested Modeling System for South America. Part I: Reanalyses Boundary Forcing: Journal of Climate, v. 16, no. 15, p. 2437-2453.

Simms, M. J., 2004, Tortoises and hares: Dissolution, erosion and isostasy in landscape evolution: Earth Surface Processes and Landforms, v. 29, no. 4, p. 477-494.

Smith, R. B., and Barstad, I., 2004, A Linear Theory of Orographic Precipitation: Journal of the Atmospheric Sciences, v. 61, no. 12, p. 1377-1391.

Starke, J., Ehlers, T. A., and Schaller, M., 2020, Latitudinal effect of vegetation on erosion rates identified along western South America: Science, v. 367, no. 6484, p. 1358-1361.

Stock, J. D., and Montgomery, D. R., 1999, Geologic constraints on bedrock river incision using the stream power law: J. Geophys. Res., v. 104, no. B3, p. 4983– 4993.

Stolar, D., Roe, G., and Willett, S., 2007, Controls on the patterns of topography and erosion rate in a critical orogen: Journal of Geophysical Research-Earth Surface, v. 112, no. F4, p. F04002.

Temme, A. J. A. M., and Vanwalleghem, T., 2016, LORICA – A new model for linking landscape and soil profile evolution: Development and sensitivity analysis: Computers & Geosciences, v. 90, p. 131-143.

Tucker, G. E., 2004, Drainage basin sensitivity to tectonic and climatic forcing: implications of a stochastic model for the role of entrainment and erosion thresholds: Earth Surface Processes and Landforms, v. 29, no. 2, p. 185-205.

Tucker, G. E., and Bras, R. L., 2000, A stochastic approach to modeling the role of rainfall variability in drainage basin evolution: Water Resources Research, v. 36, no. 7, p. 1953-1964.

van der Beek, P., and Bishop, P., 2003, Cenozoic river profile development in the Upper Lachlan catchment (SE Australia) as a test of quantitative fluvial incision models: J. Geophys. Res., v. 108, no. B6, p. 2309.

Vieux, B. E., 2001, Hydraulic Roughness, Distributed Hydrologic Modeling Using GIS: Dordrecht, Springer Netherlands, p. 121-134.

Whipple, K. X., 2001, Fluvial Landscape Response Time: How Plausible Is Steady-State Denudation?: American Journal of Science, v. 301, no. 4-5, p. 313-325.

Whipple, K. X., 2014, Can erosion drive tectonics?: Science, v. 346, no. 6212, p. 918-919.

Whipple, K. X., and Tucker, G. E., 1999, Dynamics of the stream-power river incision model: Implications for height limits of mountain ranges, landscape response timescales, and research needs: Journal of Geophysical Research: Solid Earth, v. 104, no. B8, p. 17661-17674.

Willett, S. D., 1999, Orogeny and orography: The effects of erosion on the structure of mountain belts: Journal of Geophysical Research: Solid Earth, v. 104, no. B12, p. 28957-28981.

Yanites, B. J., and Ehlers, T. A., 2012, Global climate and tectonic controls on the denudation of glaciated mountains: Earth and Planetary Science Letters, v. 325, p. 63-75.

Chapter 5 Conclusion and Summary

This chapter summarizes the key results of the research chapters, provides responses to motivative questions highlighted in the dissertation introduction, and discusses future research questions and directions.

5.1 Summary of results

Chapter 2: This chapter identifies climate response to topography, quantifies the processes that control the stable water isotope compositions in precipitation ($\delta^{18}O_p$), and examines the $\delta^{18}O_p$-elevation relationship and its application in paleoaltimetry as a response to topography in the Himalayan-Tibet orogen. Our results show that: (1) when topography is lowered, the Indian summer monsoon weakens featured by reduced orographic precipitation and weaker southerly winds; the East Asian summer monsoon shifts southward with local uplift of the eastern Andes as a first-order control; the Tibetan Plateau is featured by drier conditions; (2) in the Himalayas, the Rayleigh distillation is the dominant process for $\delta^{18}O_p$ only in monsoonal regions and only when topography is above 50% of modern height, in which case $\delta^{18}O_p$ based paleoaltimetry is appropriate; (3) on the Tibetan Plateau, $\delta^{18}O_p$ linearly increases with latitude and this gradient decreases when topography is lowered, primarily due to stronger sub-cloud evaporation under dry conditions. Further, we find that only 7 out of 50 sites are appropriate for using $\delta^{18}O_p$ as paleoaltimeter due to these elevation-independent processes. This study emphasizes that climatic responses to topography vary by regions, and the primary controls of isotope compositions can be different from modern due to the climate responses, making $\delta^{18}O_p$ to be inappropriate, or at least a blunt indicator for paleoaltimetry.

Chapter 3: This chapter presents results from a regional climate model exploring the climate response the widening of the central Andes, its impact on hydrology and proxy records, and the comparison with uniform uplift. Our simulations show that: (1) on the eastern flank, orographic precipitation increases by similar amount in the south as a response to uniform uplift and widening of the central Andes; and precipitation increases by 2–7 mm/day more due to the

widening than due to the uniform uplift in the north; (2) this similar increase is triggered by an enhancement in the South American Low-level jet in both the uniform uplift and the widening scenarios, which transports moisture from sub-equatorial regions to subtropics; (3) on the western flank, precipitation changes little as a response to uniform uplift, but decrease substantially as a response to the widening due to the a shift of precipitation as the plateau widens. These climate responses can have profound impacts on hydrology. We estimated that the increase in precipitation on the eastern flank can account for up to 10 ‰ of decrease in $\delta^{18}O_p$ due to the amount effect and an overestimation of surface uplift. On the western flank, the widening of the central Andes shows a similar aridity to hyperaridity transition as in proxy records. This study highlights the impact the west-east expansion of the Andes on local hydrology and the interpretation of proxy records.

Chapter 4: This chapter presents a coupling framework, WRF-Landlab, for simulating the interactions between climate, erosion and mountain elevation. The primary coupling techniques (nested domain and asynchronous coupling), domain setting, coupling steps and procedures are introduced in detail. Then we show the results from building a narrow mountain on the western coast of the South America, at the location of today's Andes. The simulations show that with the uplift of the mountain range: (1) there is a shift of prevailing winds, with increased tropical precipitation, extended subtropical high, and southward shift of midlatitude Westerlies, and an increase in orographic precipitation by a large amount (~100%) on the windward flanks; (2) due to the shift of general circulation, precipitation responds varies by climate regimes at this latitudes, with strong rain-shadow effects formed in the tropics and midlatitudes, little change and continuing dryness in sub-equatorial region and subtropics; (3) higher annual precipitation rates generally corresponds to higher discharge, more erosion, smaller slopes and lower elevation, with exceptions on the leeward side due to erosion not keeping pace with high uplift rates. Further, the final topography created has similar hypsometry to that of modern topography, featured by a plateau in the sub-equatorial region and subtropics, and concave-up mountains with steep slopes in the tropics and midlatitudes, indicating a first-order control of mountain-climate interactions on mountain building process. This study emphasizes the necessity to incorporate mountain-climate interactions in modeling landscape evolution and inspires future research on using this coupled framework.

5.2 Responses to key questions

The goal of this dissertation is to investigate climate and isotopic response to mountain growth and coupling behaviors among climate, erosion and topography using climate and landscape evolution models. Below are brief answers to some key questions related to these responses and coupling behaviors.

(1) How does climate respond to topography in the Himalayan-Tibet and Andean orogen?

In the simulations where the Himalayan-Tibet orogen is lowered uniformly, near-surface temperature increases at the lapse rate close to modern moist adiabatic lapse (5 K/km). The response of winds, orographic precipitation and relative humidity to a reduction in surface elevation varies by regions: on the western flank of the Himalayas, wind directions switches from southerly to northwesterly, resulting in moisture transport of dry air from the north and a reduction in relative humidity by ~40% and precipitation by ~3 mm/day from modern elevation to 20% of modern elevation; in the central Himalayas, the Indian summer monsoon weakens with reduced southerly winds and an decrease in precipitation, and there is a threshold abrupt weakening at 40% to 60% of modern height; in the eastern Himalayas, there is a similar weakening in the East Asian summer monsoon, characterized by a southward retreat of the southerly winds and rain belt in east Asia at the threshold height of 40% of modern elevation; on the Tibetan Plateau, relative humidity decreases by ~20% and precipitation decreases by ~3 mm/day to only ~1 mm/day from modern elevation to 20% of modern elevation.

In the central Andes, the climate responses to a uniform uplift have been investigated in previous modeling studies (Ehlers and Poulsen, 2009; Poulsen et al., 2010). Here we show that with the widening of the central Andes: on the northeastern flank, summer precipitation increases by 7–13 mm/day due to the widening, more than the 1–4 mm/day due to a uniform uplift from 50% to 100% of modern elevation; on the southeastern flank, precipitation increases by up to 4 mm/day due to the widening, almost the same as the amount due to the uniform uplift; on the western flank, summer precipitation decreases substantially by 1–5 mm/day due to the widening, in contrast to the little change due to the uniform uplift.

(2) How does isotopic-elevation relationship respond to topography in the Himalayan-Tibet orogen? What are the controlling mechanisms? When and where does the Rayleigh distillation process perform well in explaining isotopic compositions?

We compare the $\delta^{18}O_p$ simulated by the isotope-enabled general circulation model, ECHAM, with that calculated by the Rayleigh distillation model (RDM). With the lowering of the Himalayan-Tibet orogen, our results show that the match between ECHAM $\delta^{18}O_p$ and RDM $\delta^{18}O_p$ varies by regions and surface height in the Himalayas: in monsoonal regions, ECHAM $\delta^{18}O_p$ generally agrees well with RDM $\delta^{18}O_p$ under high elevation scenarios above 60% of modern elevation, and below this height, the relationship between ECHAM $\delta^{18}O_p$ becomes poor with much smaller lapse rate; in the western Himalayas, the lapse rate of ECHAM $\delta^{18}O_p$ is much smaller than the lapse rate predicted by the RDM at 80% of modern elevation, and below this elevation, orographic precipitation is not triggered and $\delta^{18}O_p$ is unsuitable to represent precipitation-related processes. On the Tibetan Plateau, $\delta^{18}O_p$ increases linearly and this gradient decreases when the plateau is lowered.

The dominant processes vary by regions and elevation scenarios: in the western Himalayas, local surface recycling and convective processes account for the $\delta^{18}O_p$ variations with elevation under all elevation scenarios; in the monsoonal regions, vapor mixing dominants and reflects moisture transported from the south when elevations are high, but with the weakening of the monsoon and southerly winds when topography is lowered, surface recycling becomes the primary process; on the Tibetan Plateau, our results show that surface recycling is the primary process under all elevation scenarios, but is not the cause for the decrease in latitudinal $\delta^{18}O_p$ gradient; rather, the gradient is reduced due to weaker amount effect and a reduction in depleted moisture source from the south.

(3) Are the mountain-climate interactions strong enough to shape landscape on the timescale of mountain building process?

Our results show that the strength of mountain-climate interactions varies by region (climate regime or latitude) and elevation. In the subequatorial regions and subtropics where orographic precipitation is low, climate change exhibits little impact on landscape evolution through erosion, and thus it forms a plateau-like topography in our simulations. In the tropics and midlatitudes, mountain-climate interactions are weak when elevations are low due to the weak orographic precipitation and low rates of erosion, but when mountains are elevated, there is a substantial increase in orographic precipitation and erosion rates, removing materials and reducing local elevations. Over the entire mountain range, the coupled framework is able to

create similar hypsometry to that of modern topography, and we suggest a first-order control of mountain-climate interactions on mountain building processes.

5.3 Future work

This dissertation provides insights into the above questions regarding mountain-climate interactions. However, these responses can be further improved by future research, and there are many remaining questions to be answered. These future research directions are described below.

(1) Mountain-erosion-climate interactions in the Himalayan-Tibet orogen and the North American Cordillera

Our dissertation presents a modeling framework for investigating mountain-erosion-climate interactions, and this framework has been used to build a mountain in South America as its first initial experiment to study the coupled behavior in various climate regimes. The southern hemisphere is occupied mostly by ocean and the climate is controlled mostly by the global-scale general circulation, with much less disturbance by lands than in the northern hemisphere. Because of the reason, the southern hemisphere generally serves an initial testing ground for atmospheric dynamics, and this is why we conducted our very first experiment in this region. However, the climate conditions can be more complex in other mountainous regions. For example, in the Himalayan-Tibet orogen, it is divided into several climate regimes in the west-east direction and the Asian monsoons are further divided into summer and winter monsoons. Within this orogen, there have been debates on linking precipitation to erosion rates in the Himalayas (Burbank et al., 2003). Our modelling framework provides an opportunity to study this coupling across the west-east intersect.

The North America Cordillera, as part of the circum-Pacific orogenic system, is the only large-scale orogen with transform tectonism after mid-Cenozoic (Dickinson, 2004). Feng et al. (2013) studied the evolutions of climate and the key processes controlling the isotope compositions when the cordillera is lowered. It would be interesting to investigate the co-evolution of climate and topography during extension and collapse of this orogen using our framework.

(2) Effects of tectonics and lower boundary conditions on mountain-erosion-climate interactions

Now that we have investigated the climate regimes and mountain elevation as two factors impacting mountain-erosion-climate interactions, there are other important factors influencing this interaction. Tectonics is also one of the most important factors and has first-order impact, since mountain elevation is a result of the competition between tectonic uplift and climate driven erosion. This process, however, is simplified in Chapter 4 as a constant at all latitudes and under all climate regimes since it is beyond the scope of the study. Adding a spatial-variant and potentially time-variant tectonic uplift can help better understand the evolution of the mountain range.

Further, other lower boundary conditions may also have important impacts on the mountain-erosion-climate interactions. Jeffery et al. (2014) showed that precipitation is largely mediated by vegetation in central Andes. During the growth of the mountain range from almost flat to an average height 4 km, we would expect the vegetation to evolve and this evolution may have an impact on the mountain-erosion-climate interactions. It would be interesting to quantify the contribution of this factor using our modeling framework in comparison to the climate regimes & tectonics, and how this comparison evolves with the evolving mountain elevation.

(3) Interpretation on proxy records based on erosion rates

The modelling framework also provides us with potential better interpretation of paleo-surface slopes that cannot be directly simulated by previous models. In Chapter 4, the framework simulates hypsometry that is similar to modern conditions. Although the mountain slopes are overly steep because of the fixed boundary and small domain, it sheds light on future study with a wider and larger region, which may simulate mountain slopes that is similar to modern surface or paleo-surface slopes. The sensitivity of the simulated slopes to topography and climate provide a bridge in linking paleo-surface slope to the mountain elevation rather than relying on modern relationship. Further, the simulated erosion rates by the framework can serve as a more direct source than precipitation in understanding low-temperature thermochronogical records.

5.4 References

Barke, R., and Lamb, S., 2006, Late Cenozoic uplift of the Eastern Cordillera, Bolivian Andes: Earth and Planetary Science Letters, v. 249, no. 3, p. 350-367.

Battisti, D. S., Ding, Q., and Roe, G. H., 2014, Coherent pan-Asian climatic and isotopic response to orbital forcing of tropical insolation: Journal of Geophysical Research: Atmospheres, v. 119, no. 21, p. 11997-12020.

Burbank, D. W., Blythe, A. E., Putkonen, J., Pratt-Sitaula, B., Gabet, E., Oskin, M., Barros, A., and Ojha, T. P., 2003, Decoupling of erosion and precipitation in the Himalayas: Nature, v. 426, no. 6967, p. 652-655.

Dickinson, W. R., 2004, EVOLUTION OF THE NORTH AMERICAN CORDILLERA: Annual Review of Earth and Planetary Sciences, v. 32, no. 1, p. 13-45.

Deutz, P., Montañez, I. P., and Monger, H. C., 2002, Morphology and Stable and Radiogenic Isotope Composition of Pedogenic Carbonates in Late Quaternary Relict Soils, New Mexico, U.S.A.: An Integrated Record of Pedogenic Overprinting: Journal of Sedimentary Research, v. 72, no. 6, p. 809-822.

Ehlers, T. A., and Poulsen, C. J., 2009, Influence of Andean uplift on climate and paleoaltimetry estimates: Earth and Planetary Science Letters, v. 281, no. 3-4, p. 238-248.

Feng, R., Poulsen, C. J., Werner, M., Chamberlain, C. P., Mix, H. T., and Mulch, A., 2013, Early Cenozoic evolution of topography, climate, and stable isotopes in precipitation in the North American Cordillera: American Journal of Science, v. 313, no. 7, p. 613-648.

Gallagher, T. M., and Sheldon, N. D., 2016, Combining soil water balance and clumped isotopes to understand the nature and timing of pedogenic carbonate formation: Chemical Geology, v. 435, p. 79-91.

Luciene Dias de Melo, M., and Marengo, J. A., 2008, The influence of changes in orbital parameters over South American climate using the CPTEC AGCM: simulation of climate during the mid Holocene: The Holocene, v. 18, no. 4, p. 501-516.

Poulsen, C. J., Ehlers, T. A., and Insel, N., 2010, Onset of convective rainfall during gradual late Miocene rise of the central Andes: Science, v. 328, no. 5977, p. 490-493.

Schildgen, T. F., Hodges, K. V., Whipple, K. X., Pringle, M. S., van Soest, M., and Cornell, K., 2009, Late Cenozoic structural and tectonic development of the western margin of the central Andean Plateau in southwest Peru: Tectonics, v. 28, no. 4.

Simms, M. J., 2004, Tortoises and hares: dissolution, erosion and isostasy in landscape evolution: Earth Surface Processes and Landforms, v. 29, no. 4, p. 477-494.

Vimeux, F., Gallaire, R., Bony, S., Hoffmann, G., and Chiang, J. C. H., 2005, What are the climate controls on δD in precipitation in the Zongo Valley (Bolivia)? Implications for the Illimani ice core interpretation: Earth and Planetary Science Letters, v. 240, no. 2, p. 205-220.

Yanites, B. J., and Ehlers, T. A., 2012, Global climate and tectonic controls on the denudation of glaciated mountains: Earth and Planetary Science Letters, v. 325, p. 63-75.

Appendices

Appendice A Supplementary tables and figures for chapter 2

Table A-1 Classification of sites.

Classification of sites from which $\delta^{18}O$ records have been used to infer paleoaltimetry (see Section 2.4.2 and Figure 2-15 for more explanation).

Site	Latitude (° N)	Longitude (° E)	Paleoaltimetry Studies
Sites that are judged appropriate for $\delta^{18}O$-paleoaltimetry under high-elevation scenarios (black dots in Fig. 15)			
Gyirong	28.7	85.3	Wang et al. 1996
Hongtupo	31.4	103.5	Xu et al. 2016
Linzhou Basin	30.0	91.2	Ding et al. 2014
Markam Basin	29.7	98.5	Li et al. 2015
Mount Everest	28.3	87.6	Rowley et al. 2001
Namling-Oiyug Basin	29.7	89.5	Currie et al. 2005
Penbo Basin	29.8	91.2	Ingalls et al. 2017
Sites in the southernmost Himalayas where elevations are too low (red dots in Fig. 2-15)			
Chake Basin	23.8	103.1	Hoke et al. 2014
Eryuan	26.2	99.8	Hoke et al. 2014
Jianchuan Basin	26.6	99.8	Hoke et al. 2014
Lanping	26.5	99.4	Hoke et al. 2014
Luhe	25.2	101.3	Hoke et al. 2014
Nepal Siwaliks	27.4	82.8	Quade et al. 1995
Xiaolongtan Basin	23.6	103.2	Li et al. 2015
Yanyuan	27.5	101.5	Hoke et al. 2014
Sites in northern Tibet (orange dots in Fig. 2-15)			
Aertashi	38.0	75.6	Kent-Corson et al. 2009

Ganchaigou	37.7	91.0	Kent-Corson et al. 2009
Hexi Corridor	39.5	97.5	Kent-Corson et al. 2009
Huaitoutala	37.3	96.7	Zhuang et al. 2011
Huatugou	38.3	91.8	Li et al. 2016
Janggalsay	38.2	86.6	Kent-Corson et al. 2009
Lake Mahai	37.7	94.2	Kent-Corson et al. 2009
Lao Mangnai	36.9	92.0	Kent-Corson et al. 2009
Lenghu	37.8	93.4	Kent-Corson et al. 2009
Lulehe	37.5	95.1	Kent-Corson et al. 2009
Miran River	39.0	88.9	Kent-Corson et al. 2009
Oytag	39.0	75.5	Bershaw et al. 2011
Puska	37.1	78.6	Kent-Corson et al. 2009
Xiao Qaidam	37.0	94.9	Kent-Corson et al. 2009
Xorkol	39.0	91.9	Kent-Corson et al. 2009

Sites in the western or transitional regions (blue dots in Fig. 2-15)

India Siwaliks	30.4	77.6	Ghosh et al. 2004
India Siwaliks	30.3	77.6	Sanyal et al. 2005
Kailas Basin	31.2	81.0	DeCelles et al. 2011
Pakistan Siwaliks	33.4	73.1	Quade et al. 1995
Thakkhola	28.7	83.5	Garzione et al. 2000
Thakkhola-Tetang	28.7	83.5	Garzione et al. 2000
Zhada Basin	31.5	79.8	Saylor et al. 2009

Sites in central Tibet (green dots in Fig. 2-15)

Chaoyang-Hoh Xil Basin	35.5	87.4	Li et al. 2018
Deyu-Hoh Xil Basin	35.7	87.4	Li et al. 2018
Erdagou-Hoh Xil Basin	34.5	92.7	Li et al. 2018
Erdaogou-Hoh Xil Basin	35.0	92.3	Li et al. 2018
Gerze Basin	31.9	85.1	Wei et al. 2016
Hoh Xil Basin	34.6	93.0	Cyr et al. 2005
Kunlun Pass Basin	35.6	94.1	Wang et al. 2008
Linxia Basin	35.7	103.1	Dettman et al. 2003
Lunpola Basin	32.1	89.8	Rowley and Currie 2006
Nima Basin	31.8	87.5	DeCelles et al. 2011
Xuehuan-Hoh Xil Basin	35.1	88.1	Li et al. 2018
Xunhua Basin	35.9	102.5	Hough et al. 2010
Zhuonai-Hoh Xil Basin	35.4	91.8	Li et al. 2018

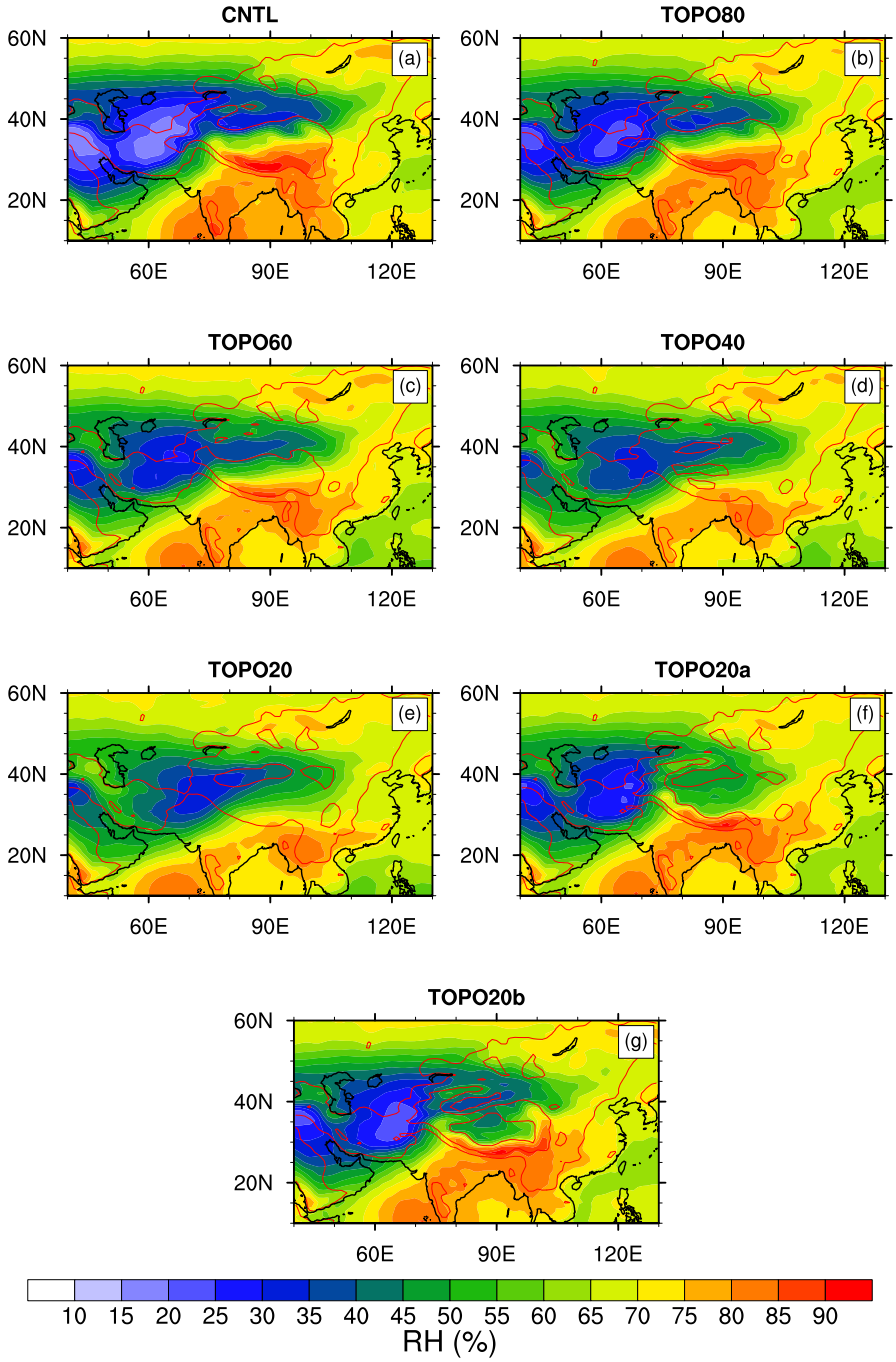

Figure A-1 Summer total-column-averaged relative humidity

Summer (June-July-August) total-column-averaged relative humidity (shaded) for (a) CNTL (b) TOPO80, (c) TOPO60, (d) TOPO40, (e) TOPO20, (f) TOPO20a, and (g) TOPO20b cases. The red lines mark 500 m and 2000 m surface elevation contours in the Tibetan region.

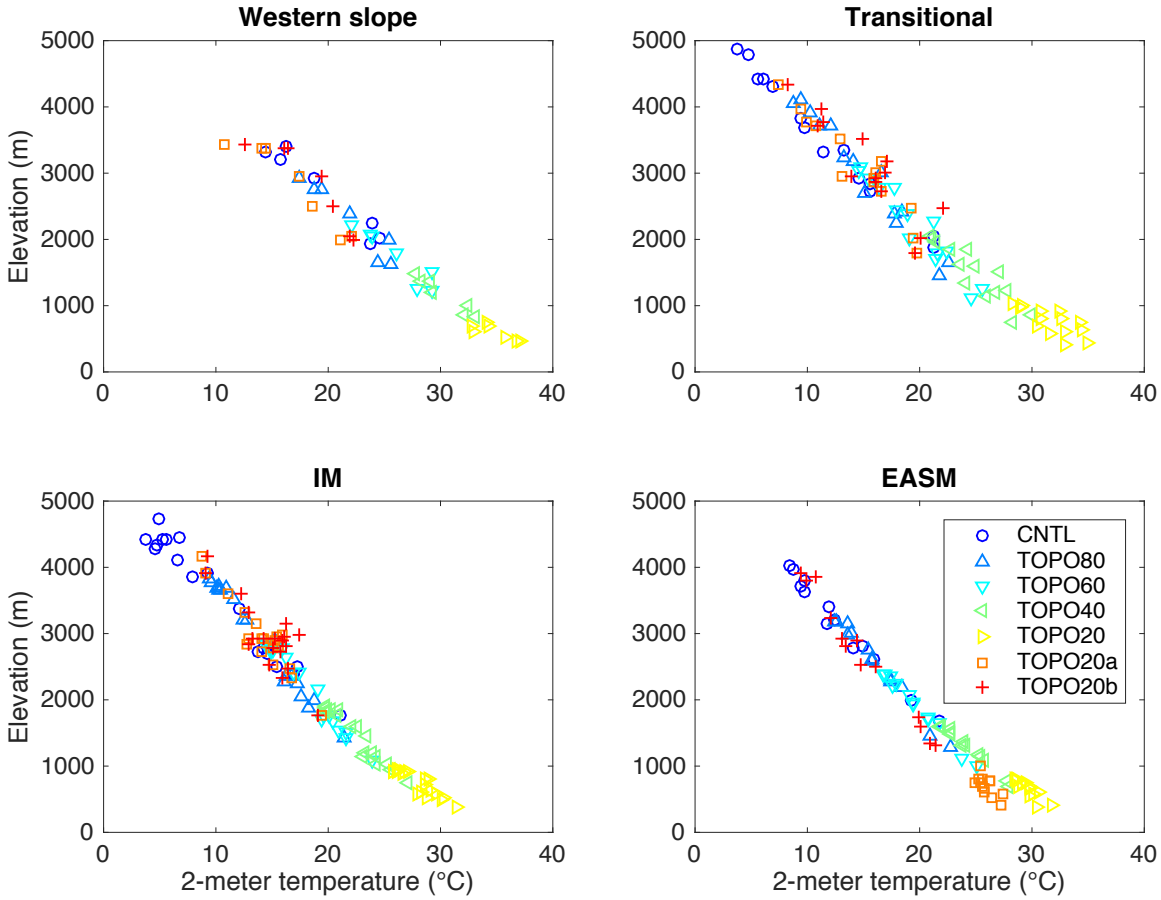

Figure A-2 ECHAM5 simulated 2-meter air temperature versus elevation

ECHAM5 simulated 2-meter air temperature (°C) versus elevation (m) for (a) western; (b) transitional; (c) IM region; and (c) EASM regions. The symbols indicate the elevation scenarios. Note that when calculating lapse rates using the data in these figures as described in section 3.1, we excluded TOPO40 and TOPO20 in the EASM region, and TOPO20 for the Himalayan and IM domains, since temperature exhibits little relationship with elevation in these low-relief cases.

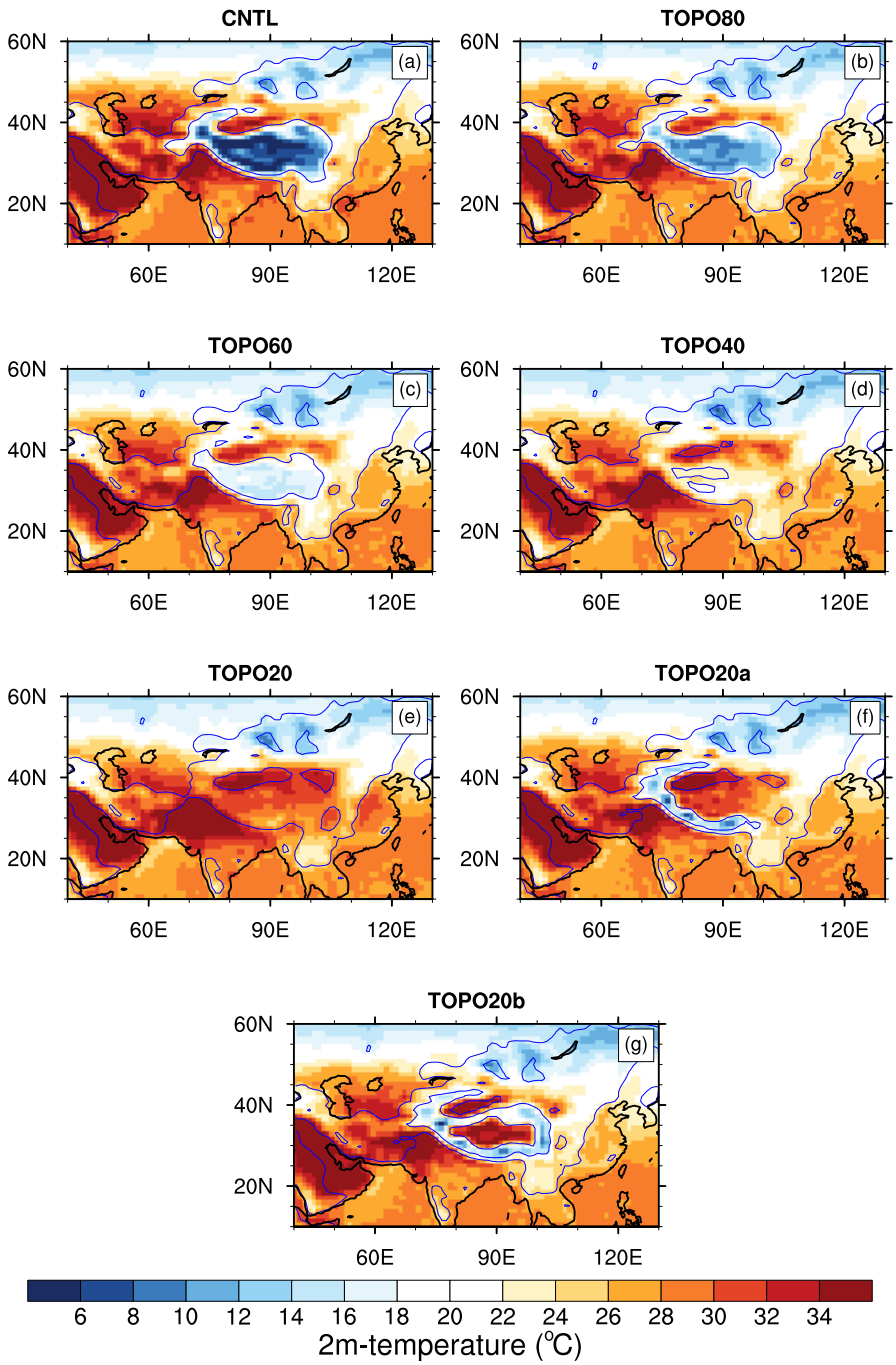

Figure A-3 ECHAM5 2-meter near surface temperature

ECHAM5 June-July-August 2-meter near surface temperature (°C) for (a) CNTL, (b) TOPO80, (c) TOPO60, (d) TOPO40, (e) TOPO20, (f) TOPO20a, and (g) TOPO20b cases. Blue contour lines mark the 500 and 2000 m Tibetan surface elevations. Temperature decreases on the slope of the Himalayas but remains largely unchanged on the Tibetan Plateau.

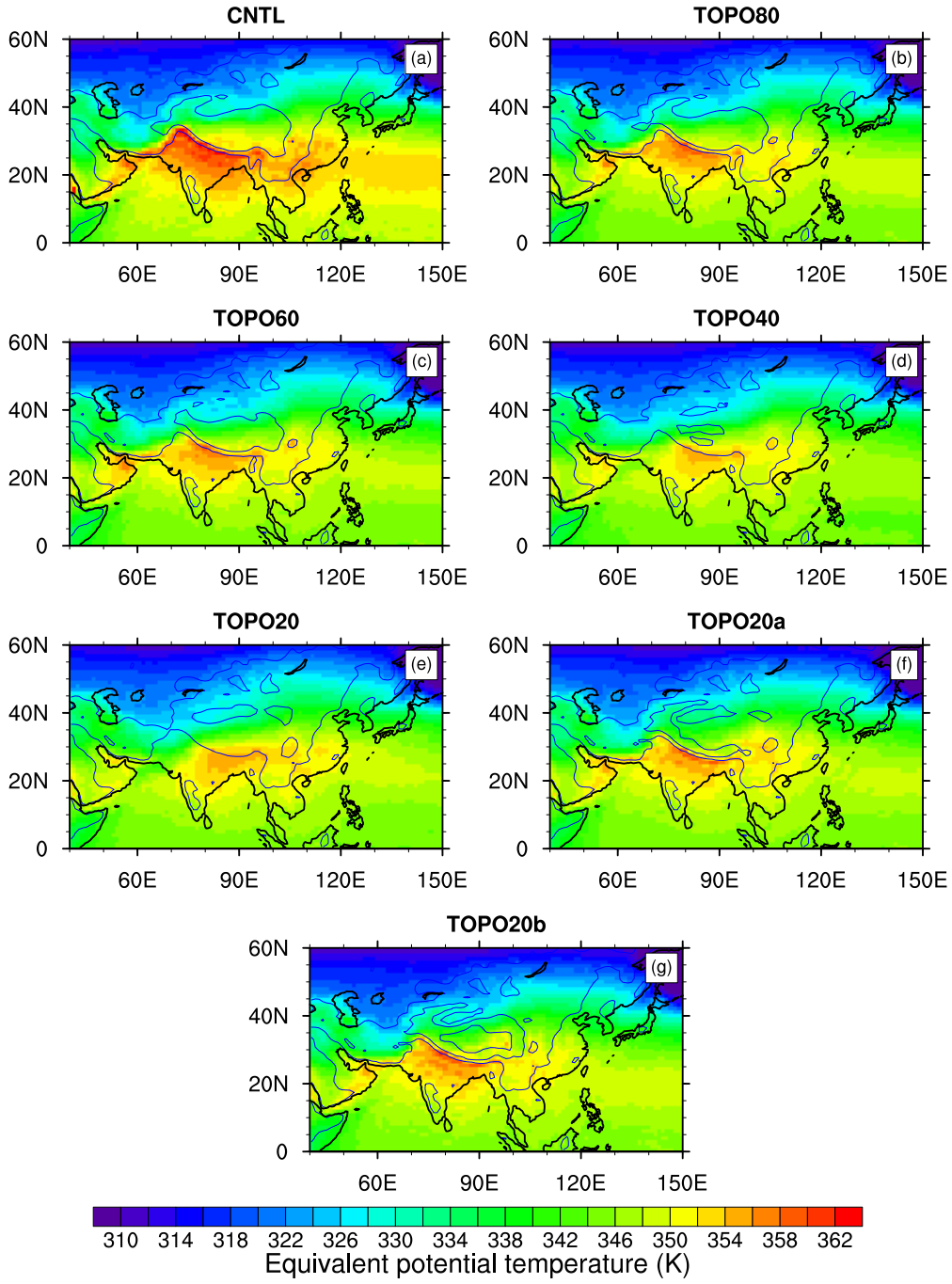

Figure A-4 Equivalent potential temperature

Equivalent potential temperature (K) at the 40 hPa sigma level for (a) CNTL, (b) TOPO80, (c) TOPO60, (d) TOPO40, (e) TOPO20, (f) TOPO20a, and (g) TOPO20b cases. Light blue contours mark 500 m and 2000 m surface elevation contours in the Tibetan reach for each case.

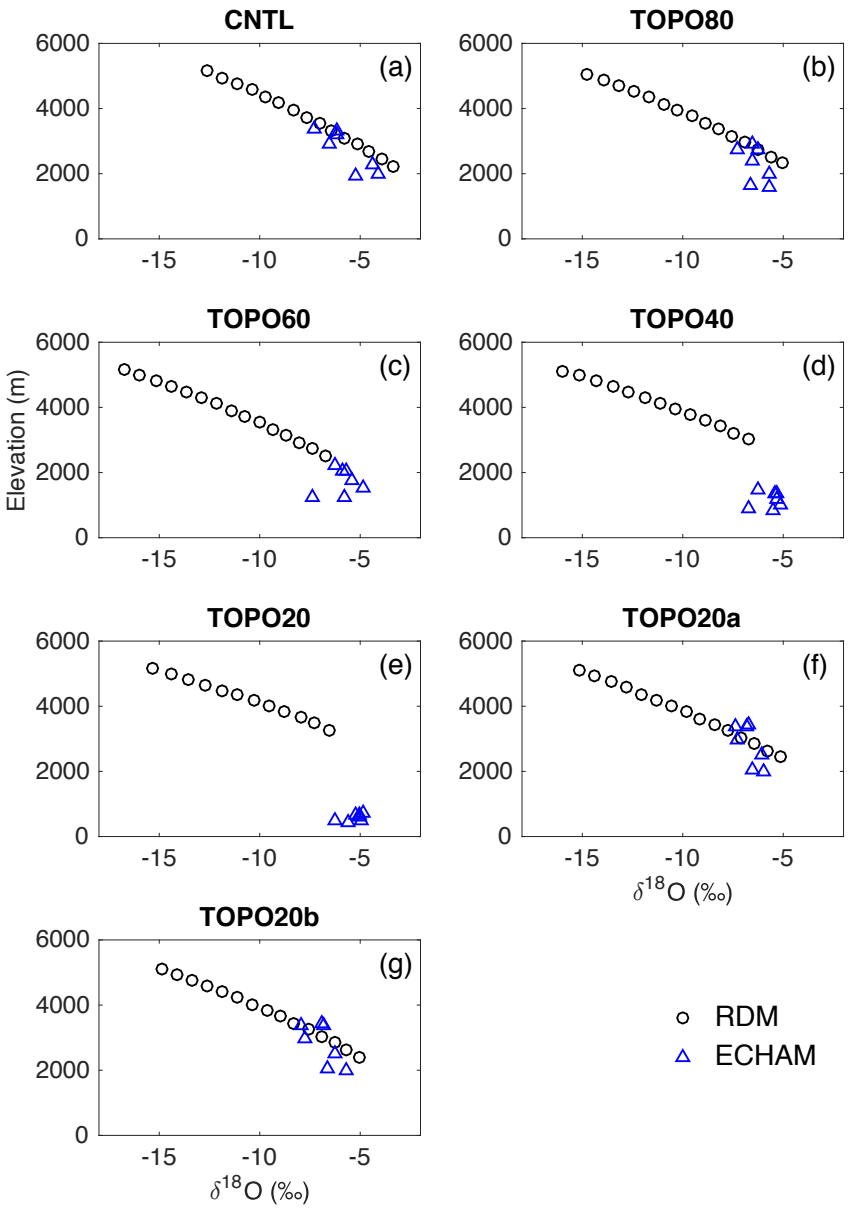

Figure A-5 ECHAM (blue triangle) and RDM (black circle) $\delta^{18}O_p$ in the western Himalayas

Monthly-precipitation-weighted ECHAM (blue triangle) and RDM (black circle) $\delta^{18}O_p$ (‰) versus elevation (m) plot for the western part of the southern Himalayan flank for the cases (a) CNTL, (b) TOPO80, (c) TOPO60, (d) TOPO40, (e) TOPO20, (f) TOPO20a, and (g) TOPO20b.

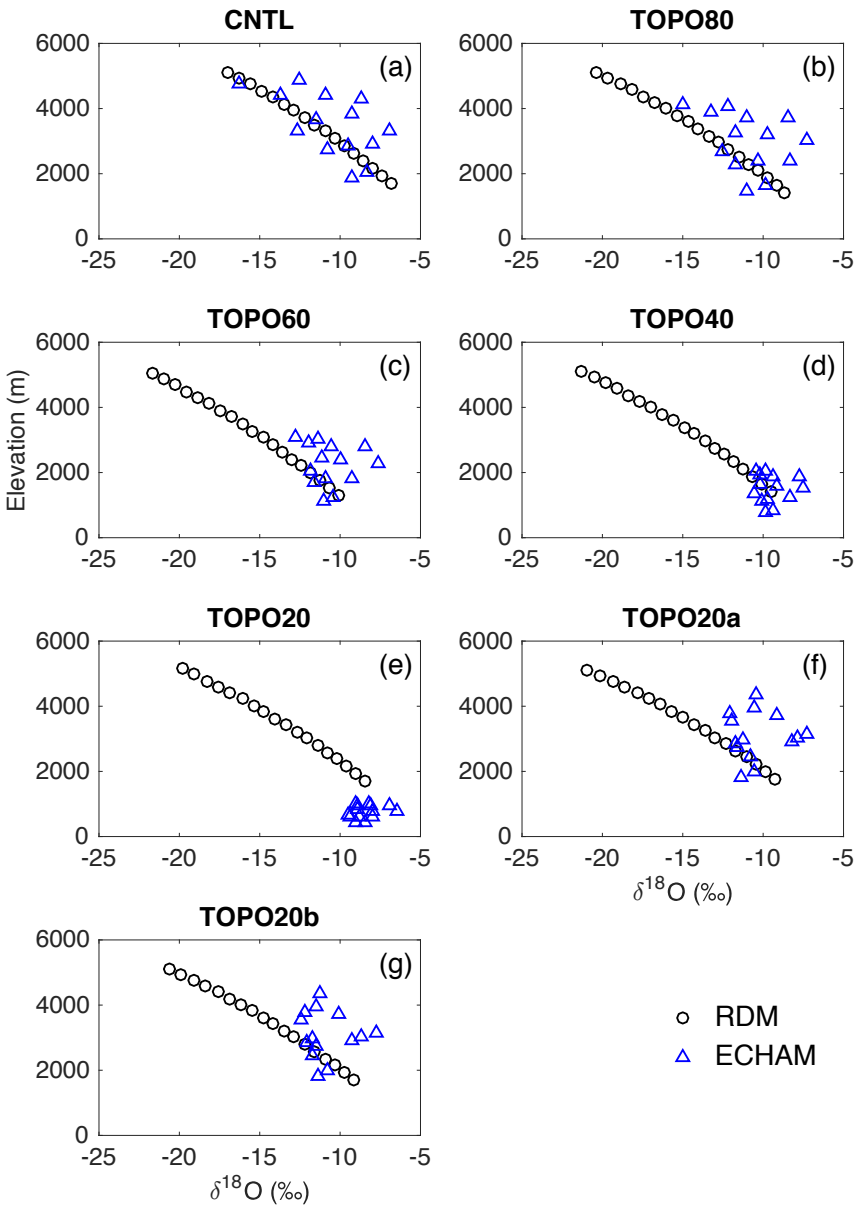

Figure A-6 ECHAM (blue triangle) and RDM (black circle) $\delta^{18}O_p$ for the transitional area

Same as figure S6 but for the transitional area between the western and the central part of the southern Himalayan flank.

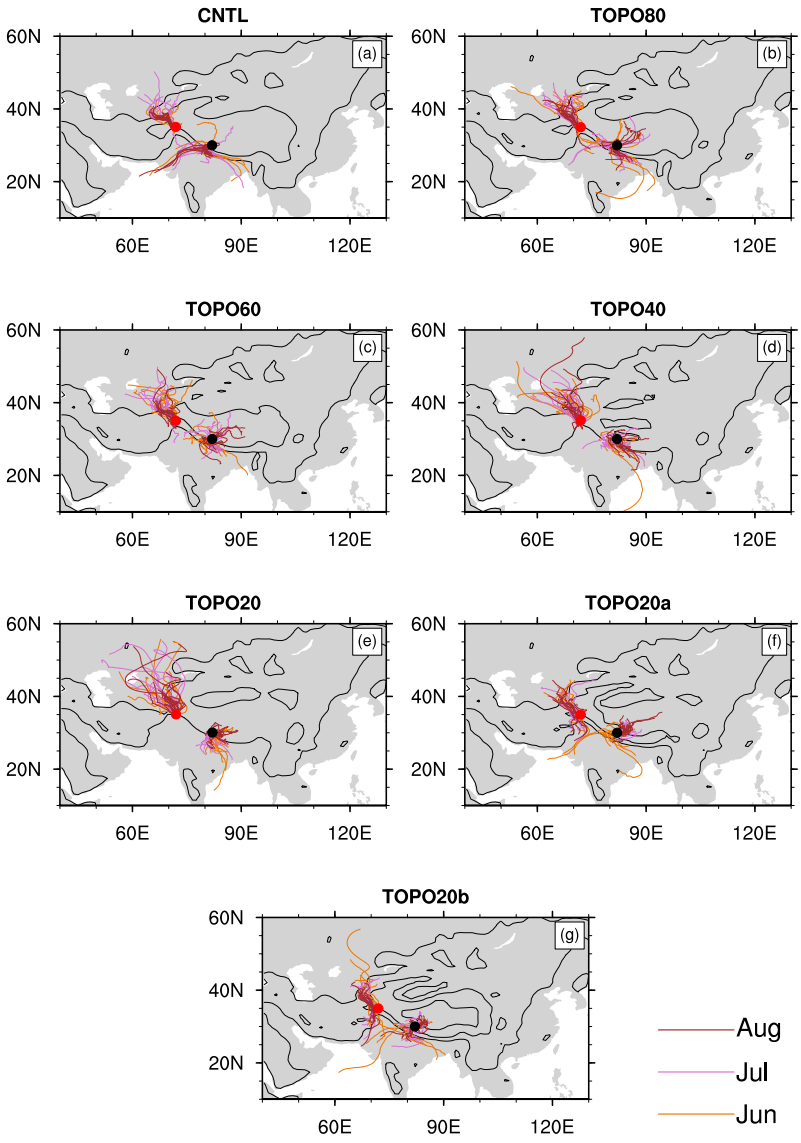

Figure A-7 Back trajectory calculations

Back trajectory calculations for air parcels originating from the western (35° N, 72° E, red filled circle) and transitional (30° N, 82° E, black filled circle) regions for (a) CNTL, (b) TOPO80, (c) TOPO60, (d) TOPO40, (e) TOPO20, (f) TOPO20a, and (g) TOPO20b cases. Black contour lines show 500 and 2000 m Tibetan surface elevations. In each case, 42 trajectories were estimated, one each for June, July, and August for 14 years. Line colors represent the month. As seen from this figure, moisture sources for the transitional region in high-elevation scenarios come from both the Bay of Bengal and the Arabian Sea. In comparison, the sources of the monsoonal regions come primary from the Bay of Bengal and northwest India (not shown).

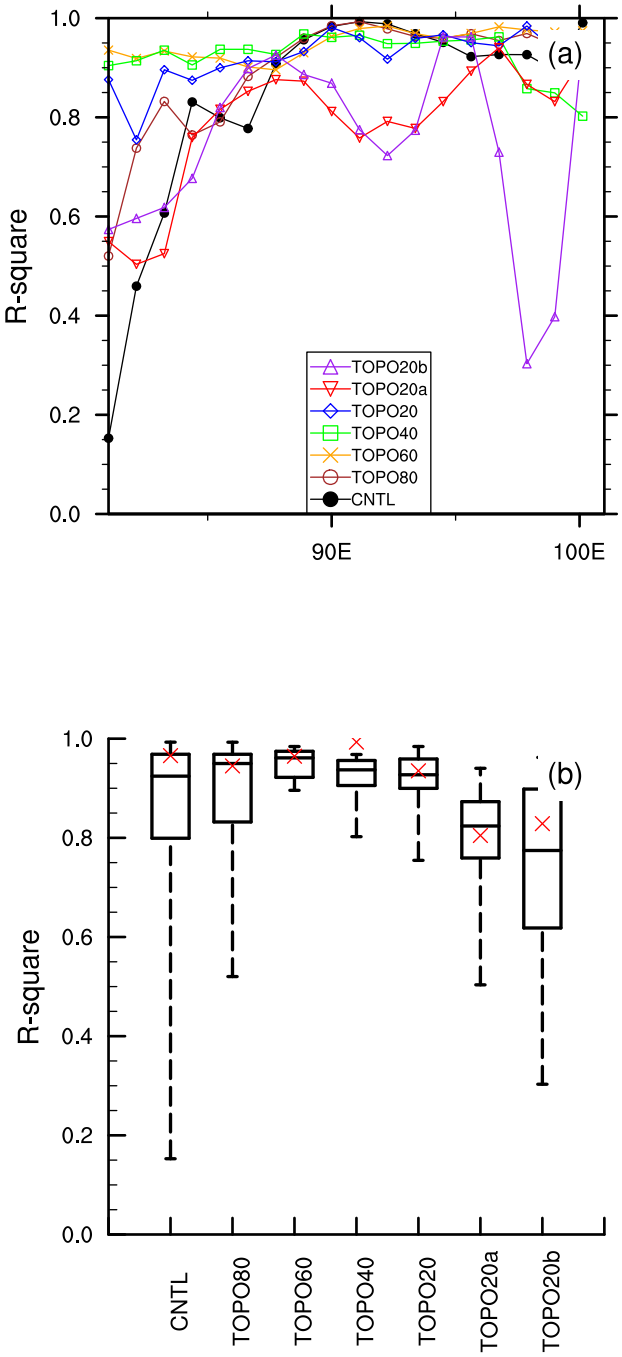

Figure A-8 Goodness of fit of the regression in Fig. 2-11

(a) The r-squared indicating goodness of fit of the regression in Fig 2-11. (b) Box plots showing minimum, maximum, median, and quartile values for (a). Red "x" represents the mean values for each scenario, calculated by regressing longitudinally averaged $\delta^{18}O_p$ across the Tibetan Plateau to latitude.

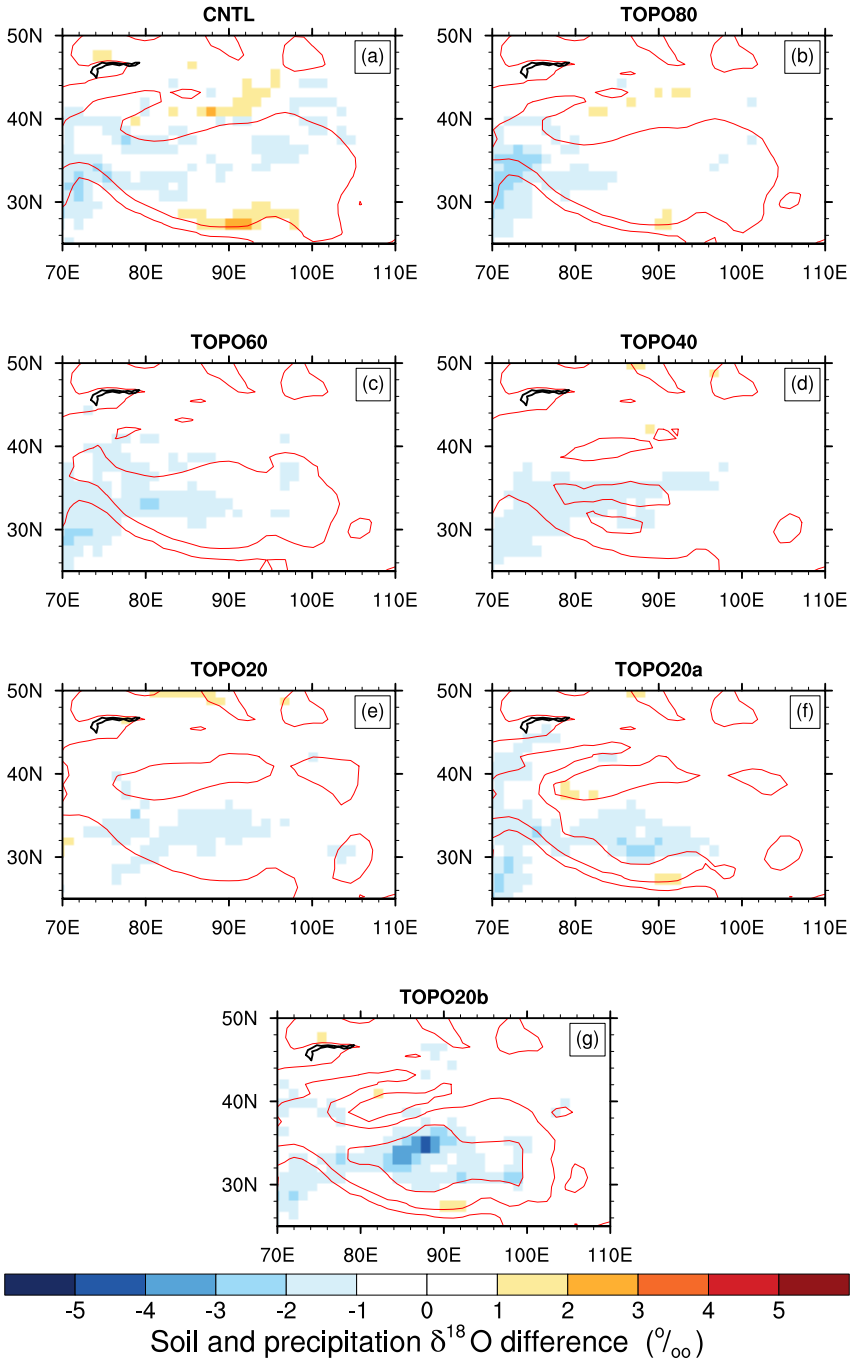

Figure A-9 Isotopic difference between soil and precipitation

Simulated summer soil $\delta^{18}O$ minus precipitation $\delta^{18}O$ for each case (a) CNTL, (b) TOPO80, (c) TOPO60, (d) TOPO40, (e) TOPO20, (f) TOPO20a, and (g) TOPO20b. The soil and precipitation $\delta^{18}O$ values are quite similar on the plateau, with soil $\delta^{18}O$ slightly lower than that in precipitation.

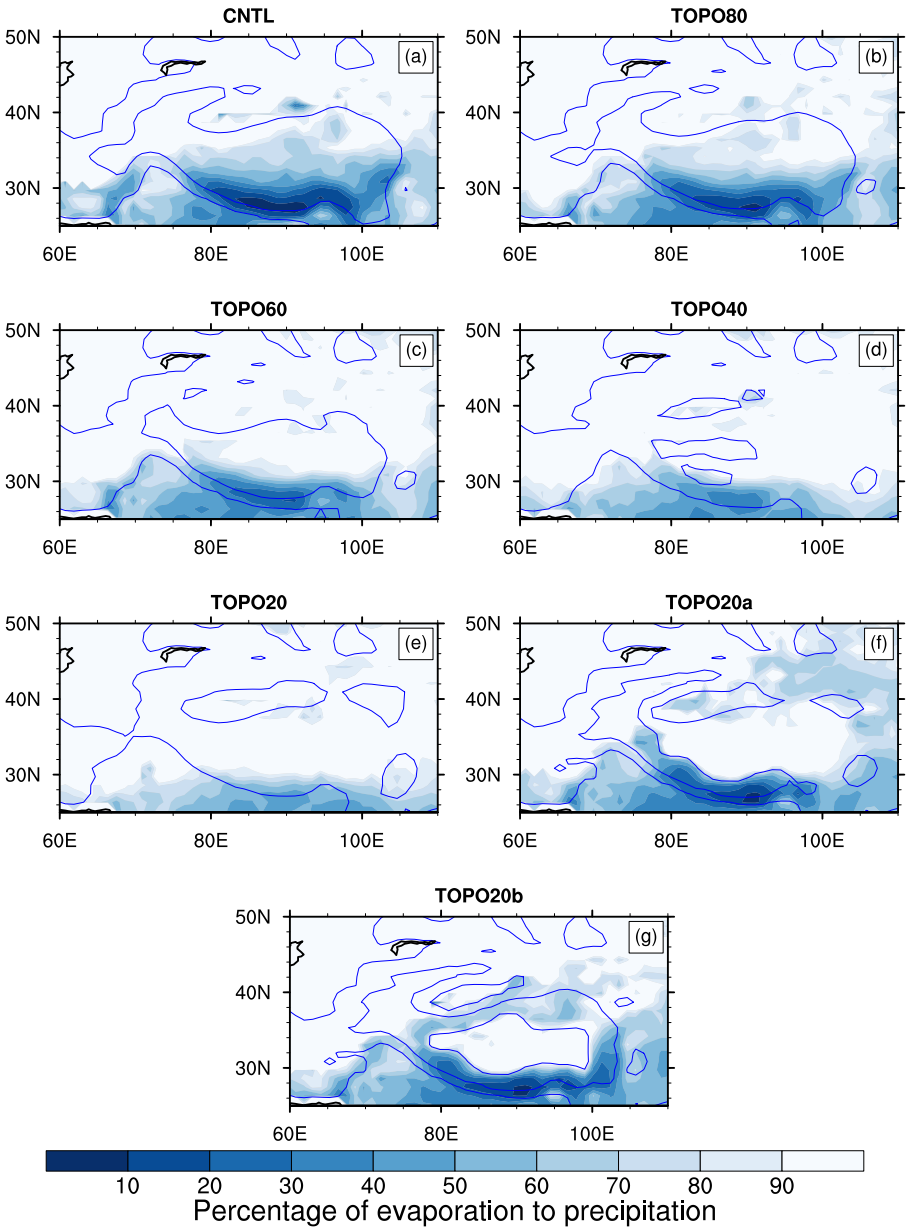

Figure A-10 Fraction of summer land surface evaporation to total summer precipitation

Fraction of summer land surface evaporation to total summer precipitation (shaded) for the (a) CNTL, (b) TOPO80, (c) TOPO60, (d) TOPO40, (e) TOPO20, (f) TOPO20a, and (g) TOPO20b cases. Blue contour lines mark the 500 and 2000 m Tibetan surface elevations. Larger portion of total precipitation is evaporated as the elevations are reduced.

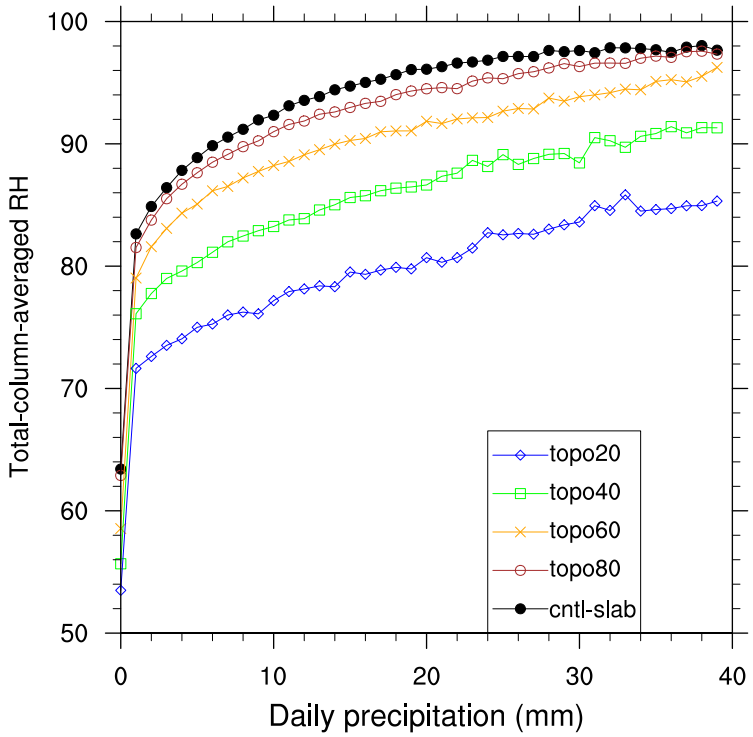

Figure A-11 ECHAM5 total-column-averaged relative humidity versus daily precipitation

ECHAM5 total-column-averaged relative humidity (%) versus daily precipitation rate (mm day^{-1}) for the Tibetan plateau. RH is higher in high-elevation scenarios than that in low-elevation scenarios at any given precipitation rate.

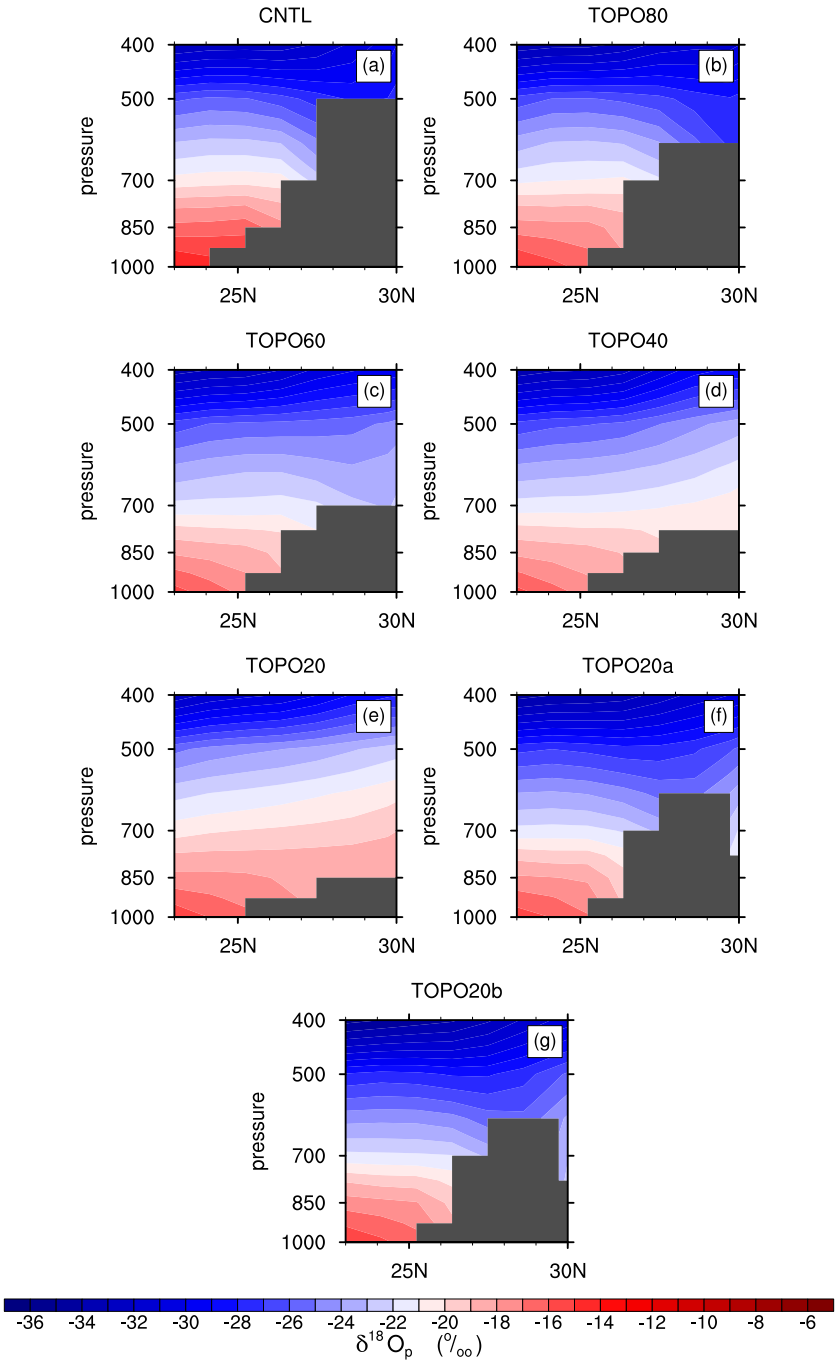

Figure A-12 Vertical profile of air $\delta^{18}O$ along the longitudinal section of 90°E

Vertical profile of air $\delta^{18}O$ along the longitudinal section of 90°E for the (a) CNTL, (b) TOPO80, (c) TOPO60, (d) TOPO40, (e) TOPO20, (f) TOPO20a, and (g) TOPO20b cases. Gray shading denotes raised topography (i.e., mountains). The low-level (~26° N) $\delta^{18}O_v$ is more depleted in lower-elevation scenarios than in CNTL. Abe, M., Kitoh, A., and Yasunari, T.: An Evolution of the Asian Summer Monsoon Associated with Mountain Uplift—Simulation with the MRI Atmosphere-Ocean Coupled GCM—, Journal of the Meteorological Society of Japan. Ser. II, 81, 909-933, doi:10.2151/jmsj.81.909, 2003.

Appendice B Supplementary figures for Chapter 3

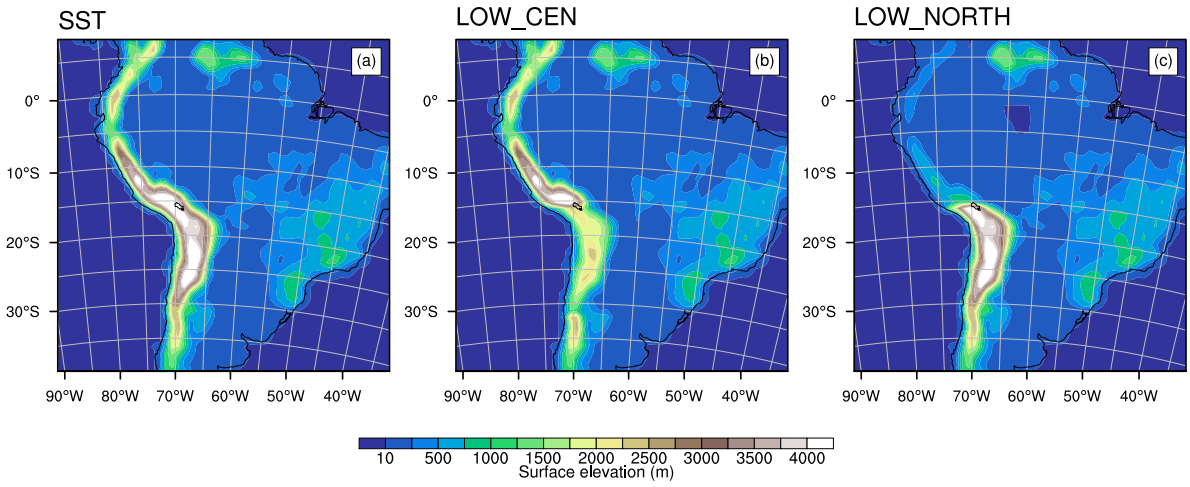

Figure B-1 Elevation scenarios

Elevation scenarios for (a) SST, (b) LOW_CEN and (c) LOW_NOR

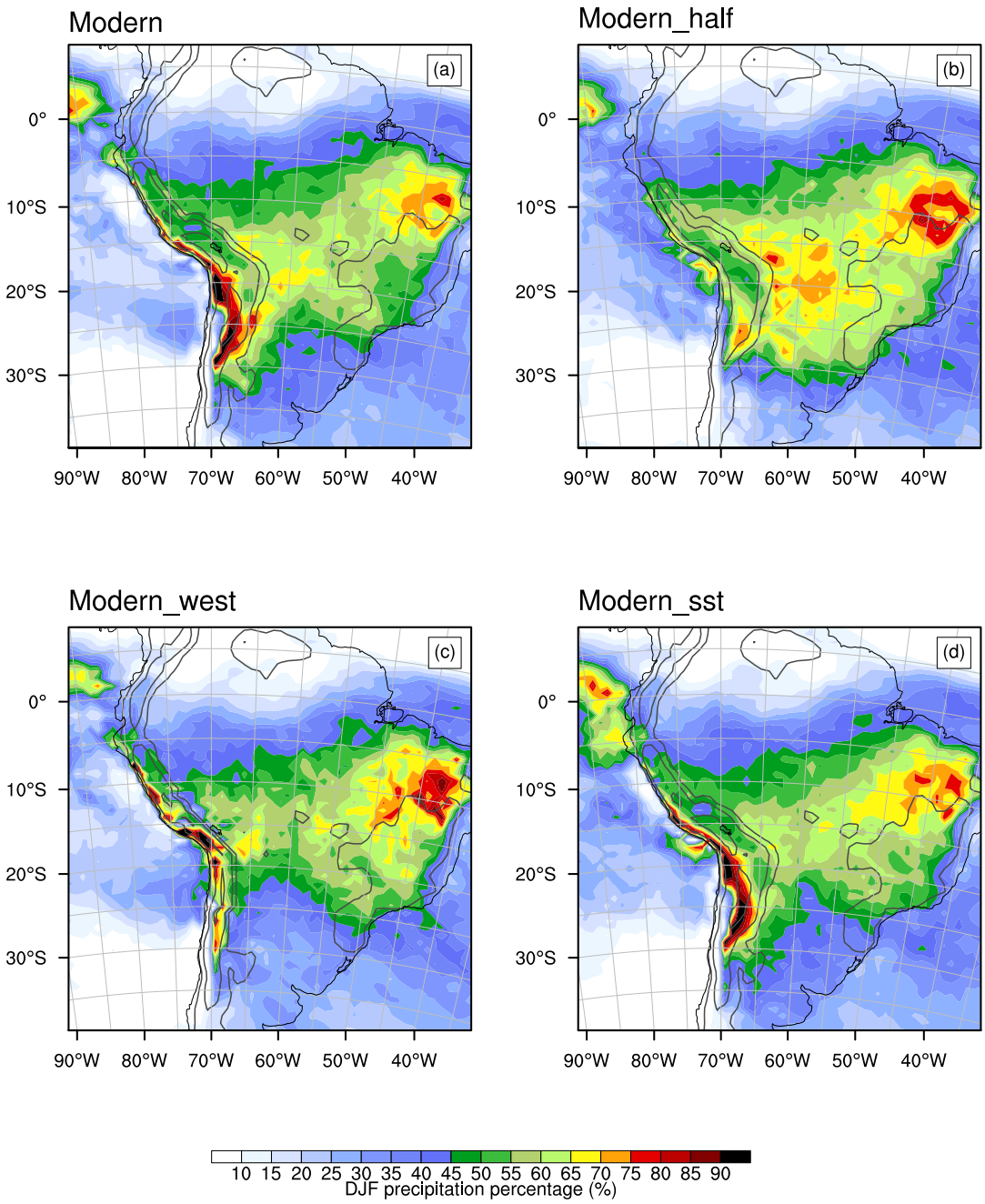

Figure B-2 DJF percentage of precipitation to mean-annual precipitation

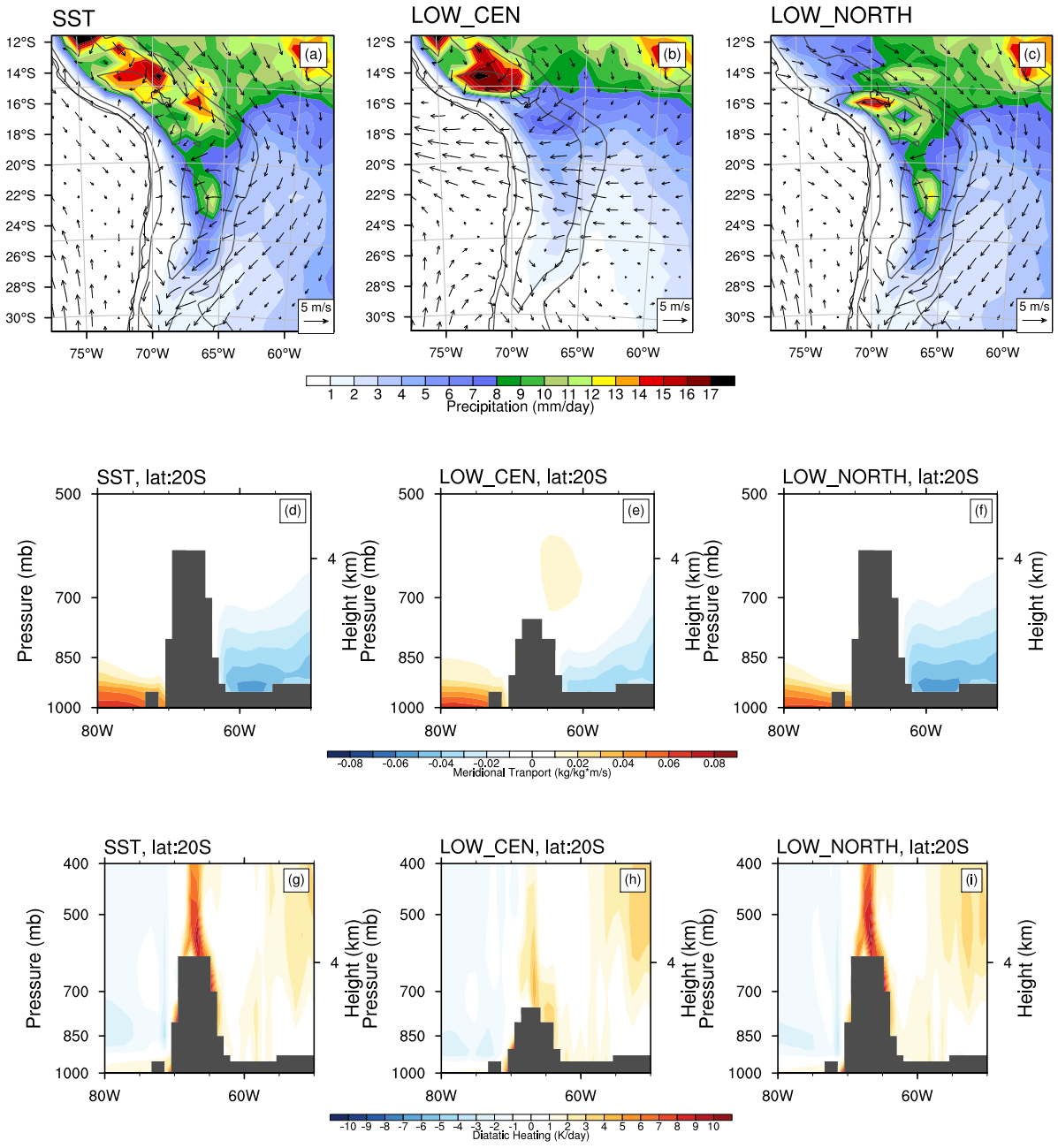

Figure B-3 DJF winds and precipitation for additional experiments

Figure B-3. (a)-(c): DJF winds (arrows) and precipitation (shaded) for scenario (a) SST, (b) LOW_CEN and (c) LOW_NORTH; (d)-(f): DJF diabatic heating (shaded) for scenario (d) SST, (e) LOW_CEN and (f) LOW_NORTH; (g)-(i): 800mb geopotential height (shaded) for scenario (g) SST, (h) LOW_CEN and (i) LOW_NORTH.

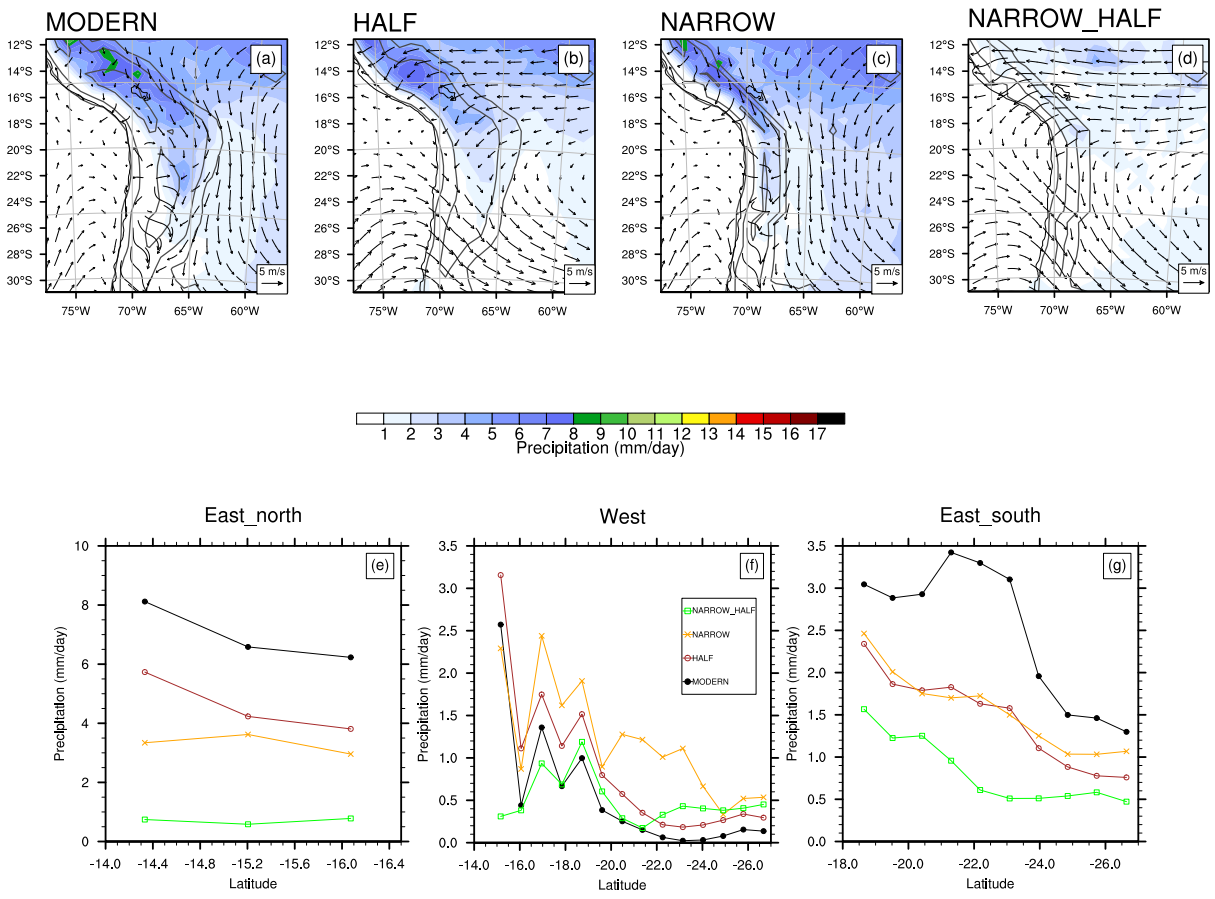

Figure B-4 Mean annual precipitation and winds

Mean annual precipitation (shaded) and winds (vectors) (a) MODERN, (b) HALF, (c) NARROW, and (d) NARROW_HALF, and mean annual precipitation averaged by regions with reference to the regions in Fig. 3.

Appendice C Supplementary figures for Chapter 4

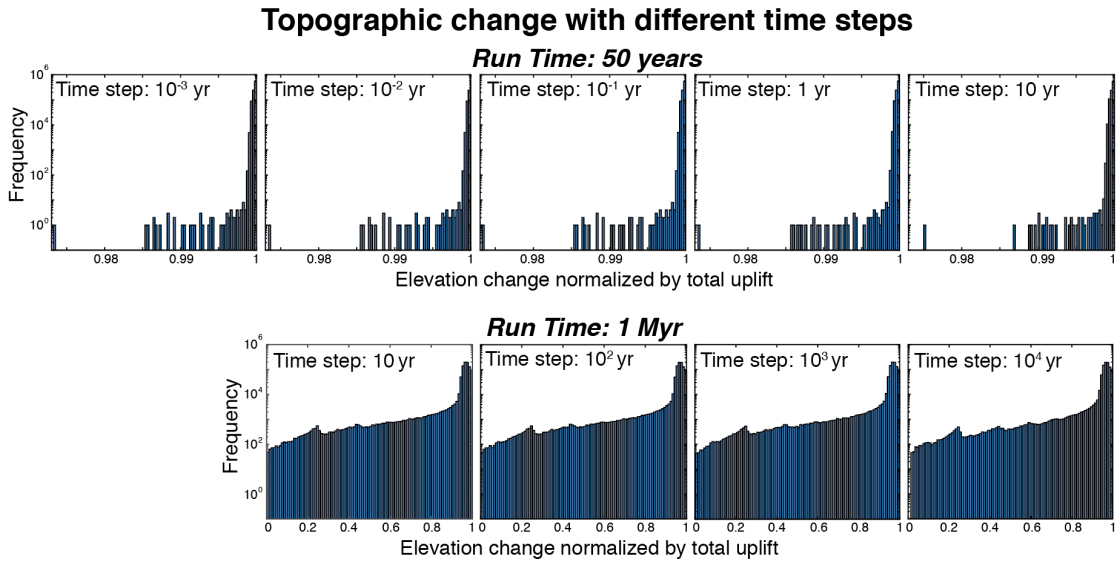

Figure C-1 Results from Landlab experiments to test the effect of the time step size

Results from Landlab experiments to test the effect of the time step size used, plotted as a frequency distribution of elevation change in each grid cell throughout the Landlab domain, normalized by total uplift (i.e. a value of 1 means the grid cell only experienced uplift, no erosion). The top plots were run for 50 years with time steps of 0.001yr (~8hrs), 0.01 yr, 0.1yr, 1 yr and 10 yr. The bottom plots were run for 1 Myr with time steps of 10 yr, 100 yr, 1000 yr, and 10,000 yr. The bottom set of experiments form plateau-like topography and therefore the peaks at ~0.2, ~0.4, and ~0.6 represent a concentration of similar values for the normalized change in elevation [(final topography – initial topography)/uplift] at the edges of the plateau. Note: a run time of 1 Myr and a time step of 1 year is too computationally expensive to complete.

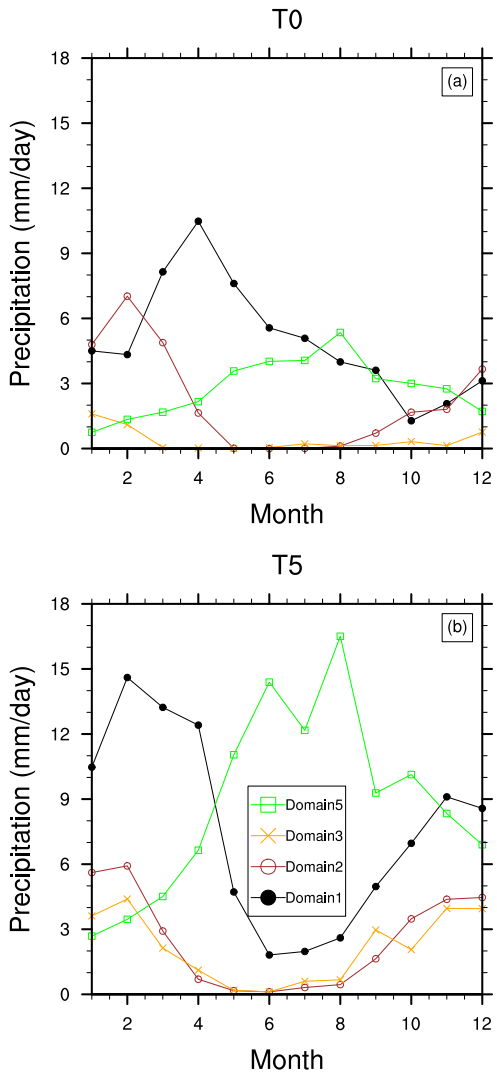

Figure C-2 Monthly domain-averaged precipitation

Monthly domain-averaged precipitation of the five domains under the elevation scenario of (a) T0, and (b) T5.